University of Alberta

Elemental impurities, defects and carbon isotopes in mantle diamond

by

Greg Lee Melton

A thesis submitted to the Faculty of Graduate Studies and Research
in partial fulfillment of the requirements for the degree of

Doctor of Philosophy

Earth and Atmospheric Sciences

Fall 2013
Edmonton, Alberta

Dedication

This is dedicated to Julie, Chloe, Tatiana, Gavin and Oliver:
my favorite collaborators.

Abstract

Monocrystalline gem-quality diamonds from Akwatia, Ghana and De Beers Pool, South Africa have trace-element concentrations ranging from ppt to ppm levels, but mostly are below the limit of quantification. Ce_N/Eu_N (1–6; N = chondrite normalized) and Ce_N/Ti_N (0.6 to 12) indicate mildly elevated LREE/MREE and variable LREE/Ti. Syngenetic garnet inclusions indicate that the diamond growth medium must have been highly enriched in LREE, with Ce_N/Eu_N and Ce_N/Ti_N from 9 to 370 and 10 to 3400, respectively. One sample, G103, has trace-element characteristics that closely resemble a carbonatitic fluid. The remaining samples show discrepancies in trace-element ratios between these diamond and inclusion-based fluid/melt compositions is inconsistent with the generalized interpretation that trace impurities in gem diamond represent trapped inclusions of the diamond-forming fluid/melt.

Model mixtures of submicroscopic inclusions of common peridotitic and metasomatic phases fail to mimic expected modal relationships for peridotitic sources. Additionally, the calculated inclusion abundances in these models would affect sample transparency, which is not observed. Trace-element patterns for most of the studied gem diamonds are not a direct representation of the diamond growth medium.

Gem-quality micro-diamonds from the Panda kimberlite (Ekati, Canada) have $\delta^{13}C$ values that are on average 1.3‰ higher than macro-diamonds from the same pipe. This documents either distinct diamond-forming fluids, fractionation process, or growth histories for these two populations. A broad trend to more 13C enriched compositions with decreasing mantle residence temperature (proxy for decreasing depth) is interpreted to reflect diamond formation from a carbonate-bearing metasomatic fluid/melt that isotopically evolves as it percolates upward through the compositionally layered Central Slave cratonic lithosphere.

The linear relationship between platelet peak area and N_B concentration that defines “regular”, non-cuboid diamonds is evaluated with a world-wide database of FTIR diamond data. This relationship is expressed as I(B’) = $0.61N_B$ and can be projected with confidence to at least ~550 at. ppm N_B. This database also shows that maximum hydrogen-related IR absorbance (3107 cm^{-1} center) correlates with increasing N_B concentrations, implying a relationship between IR-active hydrogen at 3107 cm^{-1} and the aggregation process that forms B-centers in diamond.

Acknowledgements

Thomas Stachel has been an exceptional mentor, teacher, leader and friend over the years that I have worked through the ups and downs of this PhD. I will always be grateful for his patience, generosity and wisdom. At the beginning of my time at the U of A Steven Creighton and Lucy Hunt-Ramsden showed me the ropes and welcomed me into the family. The hours of discussion spent with them and other colleagues in the Diamond Research Group at U of A taught me much and entertained me even more.

Technical aspects of some of this work could not have been possible without the help of John McNeill (CRU International, UK), Chris Ottley (Durham University, UK), D. Graham Pearson (U of A) and Richard Stern (Canadian Centre for Isotopic Microanalysis). Richard was especially instructive and encouraging while I worked through the particulars of analyzing the micro-diamonds from Panda. I am also grateful for the knowledge (scientific and otherwise) gleaned from many others at the U of A, including Bob Luth, Tom Chacko, Karlis Muehlenbachs, Sergei Matveev and Andrew Locock.

Funding for these projects was furnished to Thomas Stachel through NSERC Discovery and CRD grants as well as GSC/NRCAN GEM funding. I am also very grateful for being selected to receive the Myer Horowitz Graduate Student Association Scholarship. Samples from De Beers Pool and Akwatia were supplied by Jeff Harris (University of Glasgow) and Jon Carlson kindly gave me access to the Panda micro-diamonds.

The person that deserves the most heart-felt thanks is my wife, Julie. Thank you for having faith in me and believing me when I kept saying all of this would eventually come to an end and hopefully be worth it.

Table of Contents

List of Tables

List of Figures

List of symbols and abbreviations

at. ppm	Concentration as atomic parts per million
%B	Percent of nitrogen in the aggregated B center in diamond ($\%B = 100*N_B/(N_A+N_B)$)
^oC	Degrees Celsius
C1	Composition of a specific type of stoney carbonaceous chondrite
CCIM	Canadian Centre for Isotopic Microanalysis
CL	Cathodoluminescence
cm	Centimeter
$\delta^{13}C$	Carbon isotope ratios expressed relative to a standard (VPDB)
$\Delta \log fO_2$	Oxygen fugacity relative to a specific reaction buffer
$\Delta m/m$	Mass resolution
$D^{dia/l}$	Partition coefficient between diamond and a liquid
DTC	Diamond Trading Company
FMQ	Fayalite-magnetite-quartz oxygen buffer reaction
FTIR	Fourier transform infrared spectroscopy
Ga	Billions of years
GPa	Giga Pascal
h	Hour
HEPA	High-efficiency particulate air
HFSE	High field strength element
HPHT	High pressure high temperature
HREE	Heavy rare earth elements (subscript N = normalized)
Hz	Hertz
I(B')	Integrated absorption strength of platelet peak
IR	Infrared
J	Joule
kbar	Kilobar
keV	Kiloelectron volts

km	Kilometer
kV	Kilovolts
LA-ICP-MS	Laser ablation inductively coupled plasma mass spectrometer
LILE	Large ion lithophile element
LOD	Limit of detection
LOQ	Limit of quantification
LREE	Light rare earth elements (subscript N = normalized)
μm	Micrometer
Ma	Millions of years
min	Minute
MC-SIMS	Multicollector secondary ion mass spectrometer
mm	Millimeter
MREE	Middle rare earth elements (subscript N = normalized)
mW/m^2	Heat flow units in milliwats per meter squared
nA	Nanoampere
Nd:YAG	Neodymium doped yttrium aluminum garnet
nm	Nanometer
ppb	Concentration in parts per billion
ppm	Concentration in parts per million
ppt	Concentration in parts per trillion
REE	Rare earth element
σ	Standard deviation
Type IaA	Diamond with > 90% of nitrogen in the A center
Type IaAB	Diamond with < 90% of nitrogen in either the A or B center
Type IaB	Diamond with > 90% of nitrogen in the B center
Type Ib	Diamond with only singly substituted nitrogen
Type II	Nitrogen free diamond
USGS	United States Geological Survey
VPDB	Vienna Pee-Dee Belemnite carbon isotope standard
wt%	Concentration in weight percent

Chapter 1 – Introduction

This thesis is aimed at expanding previous research into diamond genesis by focusing on elemental impurities and carbon isotopic compositions. The samples utilized in these studies are derived from De Beers Pool (South Africa), Akwatia (Ghana) and the Ekati mine (Canada). The thesis will explore topics in diamond genesis by investigating the following: I) trace-elements in gem diamond from De Beers Pool and Akwatia; 2) nitrogen and carbon isotope data for micro- and macro-diamonds from the Panda kimberlite (Ekati); 3) a detailed analysis of a world-wide database of FTIR spectral characteristics in an effort to understand the behavior of various defects.

Before considering these works, it is necessary to first discuss the general provenance of natural diamond in the deep Earth and the geologic settings of the sample sources.

1.1. Background

Below the crust is the part of the Earth's interior called the mantle. The major distinguishing property between these two layers is their composition. While the crust is enriched in fusible major elements (e.g. Ca, Na, Al), the mantle is relatively enriched in elements like Mg, Ni and Cr (McDonough and Sun, 1995; Palme and O'Neill, 2007). As a consequence of their divergent geochemical makeup and ambient temperatures and pressures, these two layers naturally possess contrasting mineralogies. Despite being extremely heterogeneous, the continental crust has an average composition of andesite. That is to say, it is dominated by quartzofeldspathic minerals. However, the vast majority of the mantle is ultra mafic with varying proportions of olivine, orthopyroxene,

clinopyroxene and garnet (peridotite). Eclogite (garnet and pyroxene-rich rock) and pyroxenite (pyroxene-rich rock) are the only other rock types in the lithospheric mantle of significant abundance. The upper mantle behaves in a brittle fashion and, together with the crust, comprises the lithosphere. Just below the lithosphere is the asthenospheric mantle which is broadly similar in its chemical composition to the lithsopheric mantle, but behaves in a more ductile manner.

One element that is significantly enriched in the crust versus the mantle is carbon. Despite its partitioning into the crust, carbon naturally occurs in the upper mantle with an expected concentration of 400 ppm (Javoy 1997). Because of its incompatible and volatile nature it can be efficiently concentrated in very low degrees of partial melt. If it is not a dissolved component of a melt/fluid, then it can be stored in the mantle in solid phases like carbonates or elemental carbon (graphite or diamond). At low oxygen fugacity, in a metal saturated mantle, carbon may also be stored as a dissolved component in Ni-Fe alloys. At even lower oxygen fugacity, carbides may represent an important carbon reservoir.

With the appropriate temperature, pressure and oxygen fugacity, diamond will be a stable solid carbon phase. A “cool” geotherm is generally needed for diamond to be stable in the lithosphere. Otherwise the temperatures required for diamond formation will correspond to greater depths (i.e. higher pressure) exceeding the thickness of the lithosphere, where diamond formation is less feasible. Specifically, in a peridotite host rock, diamond is stable at temperatures above ~900ºC (4.25 GPa) and at an oxidation state of $\Delta \log fO_2 \leq -1.8$, relative to FMQ (Luth, 1999). In eclogitic host rocks, diamond is stabile at more oxidizing environments.

The Archean shield (cratonic) geotherm, which is “cooler” than a typical continental geotherm (Hasterok and Chapman, 2011), is an ideal environment for diamond. Cratons are remnants of old crustal domains that have survived destructive tectonic processes for billions of years and retained deep reaching lithospheric mantle roots. In addition to old age, cratonic lithosphere is different from younger continental lithosphere in that it is thicker and colder. Typical continental lithosphere extends to depths of ~100 km, whereas cratonic “keels” can be as deep as 250 km (Boyd and Gurney, 1986). The lithospheric mantle below cratons was created during the Archean during high degrees of partial melt extraction in the mantle. This left the lithospheric mantle depleted relative to the ductile, more fertile asthenospheric mantle. This compositional contrast causes the lithospheric mantle to be colder and less dense than asthenospheric mantle, contributing to its preservation from convective forces of the asthenosphere.

Despite our understanding of the mantle environment required for diamond precipitation, many questions regarding diamond-forming processes still exist. Some of the questions I hope to address are: 1) what is the diamond-precipitating medium? Is it a fluid or melt and how do the high density fluids identified by Klein-BenDavid et al. (2009) in fibrous diamonds relate to gem-diamond growth? And 2) what are the diamond-forming redox reactions: carbonate reduction (EMOD) or CH_4 oxidation (Taylor and Green, 1989)?

Elemental impurities in diamond are one source for answers to these questions. But due to the strong covalent carbon-carbon bonds which give diamond its superior hardness, few elemental impurities can be accommodated in the diamond structure. Nevertheless, nitrogen substitutes into the diamond lattice in concentrations reaching thousands

of ppm and can be used to investigate formation and residence conditions of diamond in the upper mantle. In addition to nitrogen, other trace-elements have been measured in natural diamond that can contribute to our understanding of their formation.

1.2. Geologic settings

1.2.1. De Beers Pool, South Africa

The De Beers Pool mines consist of four kimberlites that have been in production since the late 1800's: De Beers, Dutoitspan, Bultfontein and Wesselton. These kimberlites are located near Kimberley, South Africa and intruded the Kaapvaal Craton between 83 and 90 Ma (Figure 1.1; Allsop and Barrett, 1975). Data from detrital zircons in sedimentary sequences in the craton indicate that craton formation began at about 3.7 Ga (de Wit et al., 1992). Crustal generation continued with accretion of

Figure 1.1. Map of southern Africa showing the location of Kimberley, South Africa. Shaded region indicates extent of the Kaapvaal craton (simplified from de Wit et al., 1992).

oceanic crust, granite generation and chemical differentiation of the upper lithosphere. Accretion, magmatism and tectonic processes continued to expand and modify the craton until a final collisional event with the Zimbabwean Craton to the north created the Kalahari Craton around 2.6 Ga (de Wit et al., 1992).

The lithospheric mantle below the De Beers Pool kimberlites, based on garnet xenocryst data, is dominated by “fertile peridotite” in the upper portion of the lithospheric mantle (Griffin et al., 2003). In this context, “fertile peridotite” is used to represent the composition of mantle garnets (major and trace-elements) that show little to no evidence of a depletion event. At depths > 100 km, however, the mantle section becomes increasingly depleted, with signs of subsequent refertilization by metasomatism. Finally, at depths > ~160 km the lithosphere below De Beers Pools is melt metasomatized, indicated by the enrichment of melt-mobile elements like Zr, Ti and Y. Enrichment by melt metasomatism at the base of the cratonic lithosphere is observed, in varying degrees, for almost all of the sample locations throughout the Kaapvaal Craton (Griffin et al., 2003).

Diamonds recovered from De Beers Pool with a peridotitic paragenesis have been dated at 3.3 Ga to 3.2 Ga (Richardson et al., 1984) but those of the eclogitic paragenesis are younger (2.9 Ga, Richardson et al., 2001). Studies on inclusions in diamonds indicate that most of the peridotitic diamonds trapped inclusions that were in equilibrium with the highly depleted section of the lithosphere (< 160 km) and only a few showed signs of interaction with melt metasomatism similar to the deeper (>160 km) garnet xenocrysts (Griffin et al., 2003; Phillips et al., 2004; Banas et al., 2009).

1.2.2. Akwatia, Ghana

Diamonds from Akwatia are hosted in alluvial stream sediments of the Birim and Bonsa rivers (Figure 1.2; Mílesi et al., 1992). These sediments are sourced from the Paleoproterozoic Birimian Supergroup, situated on the southern edge of the West African Craton. The Birimian Supergroup includes volcanic belts with intermittent sedimentary basins and ubiquitous outcroppings of granitoids (Taylor et al., 1992). Crustal generation in this part of the craton initiated at ~2.2 Ga with large degrees of magmatism and its volcanic counterparts (Hirdes and Davis, 1998). There is no indication that an Archean crustal component exists; however, Sm-Nd isotope data suggests much of the basaltic magmatism was derived from a previously depleted mantle source. The diamonds themselves were likely derived from weathering of metakimberlites within the Birimian Supergroup (Appiah et al., 1996).

Geothermobarometry from diamond inclusions indicates the host diamonds grew in deeper conditions than typically observed for other peridotitic locations (Stachel and Harris, 1997). These inclusions also record a history of metasomatic re-enrichment of a depleted lithospheric mantle. A deep lithospheric source is confirmed by a slight increase of Si

Figure 1.2. Location map of the Birim diamond field near Akwatia, Ghana (from Stachel et al., 1997).

in garnet, i.e. the presence of the majorite component ($Mg_4Si_4O_{12}$) in some garnet inclusions.

1.2.3. Panda (Ekati), Canada

The Ekati mine of the Northwest Territories began operations in 1998 and was Canada's first diamond mine. The Ekati property includes 150 kimberlite pipes, six of which have been, or are currently, under production: Panda, Koala, Koala North, Fox, Misery and Beartooth. These kimberlites are hosted by 2.6 Ga Archean granitoids (Davis et al., 2003). The Slave Craton is bound on the east and west by the Paleoproterozoic Thelon-Taltson and Wopmay orogens, respectively (Figure 1.3).

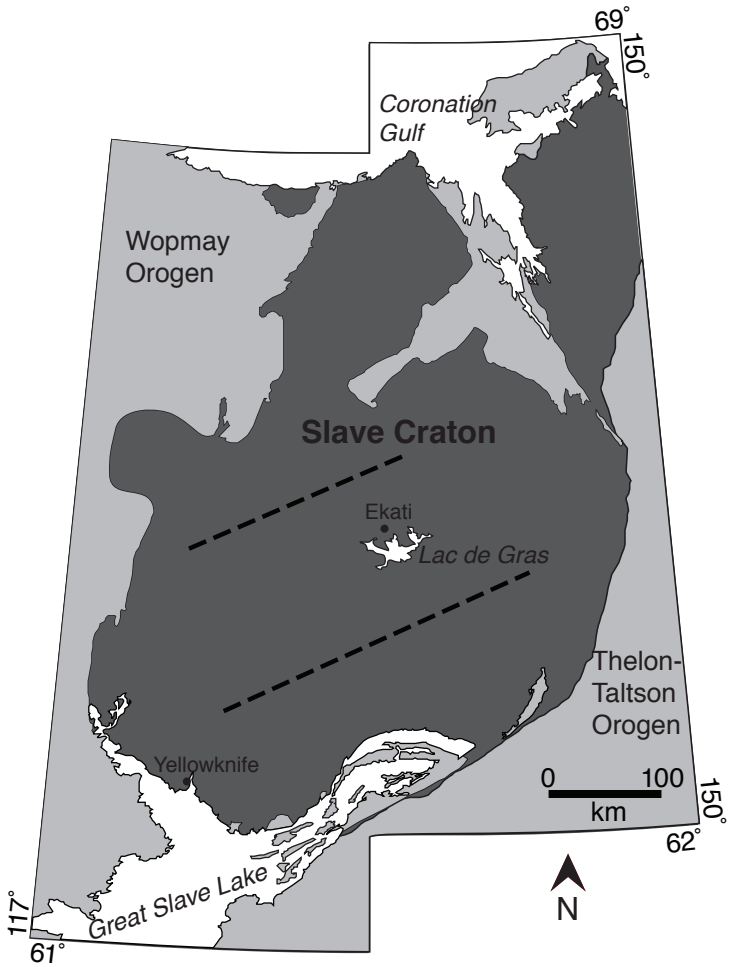

Figure 1.3. Map showing the extent of the Slave Craton and the location of the Ekati mine (simplified from Bleeker and Davis, 1999). The Central Slave Craton is that part between the dashed lines (Grütter et al., 1999).

The “Central Slave Basement Complex” is overlain by thick mafic (and lesser intermediate) volcanic rocks and turbidititic graywackes. These sequences are intruded by voluminous 2.62 - 2.58 Ga granitic plutons (Bleeker et al., 1999).

The Central Slave domain is defined, geochemically, by differences in degrees of depletion in the lithospheric mantle as recorded by garnet xenocrysts from kimberlites. The northern domain of the Slave has a high proportion of lherzolitic and eclogitic garnets with moderately subcalcic garnets (i.e. G10 garnets, Grütter et al., 2004) being less common. The central Slave has a distinctive subpopulation of ultra depleted (possibly dunitic) garnets with CaO < 1.8 wt% but in general, garnets are moderately subcalcic. The southern most domain consists of lherzolitic and eclogitic garnets, similar to the northern domain, but some subcalcic garnets have high Cr_2O_3. These data indicate that the lithospheric mantle below the Slave Craton has experienced significantly variable degrees of melt depletion, or has been unequally modified by metasomatic process.

Within the Central Slave lithospheric mantle, garnet xenocrysts also display strong vertical heterogeneity that indicates a highly depleted “harzburgitic” upper lithosphere overlies a less-depleted “lherzolitic” layer at the bottom of the lithosphere (Griffin et al., 1999). This chemical layering is further explored in Chapter 4 of this thesis.

References

Allsopp, H.L., Barrett, D.R., 1975. Rb-Sr age determinations on South African kimberlite pipes. Physics and Chemistry of the Earth 9, 605–617.

Appiah, H., Norman, D.I., Kuma, J.S., 1996. The diamond deposits of Ghana. Africa Geoscience Review 3, 261–272.

Banas, A., Stachel, T., Phillips, D., Shimizu, N., Viljoen, K.S., Harris, J.W., 2009. Ancient metasomatism recorded by ultra-depleted garnet inclusions in diamonds from DeBeers Pool, South Africa. Lithos 112, 736–746.

Bleeker, W., Davis, W.J., 1999. The 1991-1996 NATMAP Slave Province Project: Introduction. Canadian Journal of Earth Sciences 36, 1033–1042.

Bleeker, W., Ketchum, J.W., Jackson, V.A., Villeneuve, M.E., 1999. The Central Slave Basement Complex, Part I: its structural topology and autochthonous cover. Canadian Journal of Earth Sciences 36, 1083–1109.

Boyd, F.R., Gurney, J.J., 1986. Diamonds and the African Lithosphere. Science 232, 472–477.

Davis, W.J., Jones, A.G., Bleeker, W., Grütter, H., 2003. Lithosphere development in the Slave craton: a linked crustal and mantle perspective. Lithos 71, 575–589.

de Wit, M.J., de Ronde, C.E.J., Tredoux, M., Roering, C., Hart, R.J., Armstrong, R.A., Green, R.W.E., Peberdy, E., Hart, R.A., 1992. Formation of an Archaean continent. Nature 357, 553–562.

Griffin, W.L., Doyle, B.J., Ryan, C.G., Pearson, N.J., Suzanne, Y.O., Davies, R., Kivi, K., Van Achterbergh, E., Natapov, L.M., 1999. Layered mantle lithosphere in the Lac de Gras area, slave craton: composition, structure and origin. Journal of Petrology 40, 705–727.

Griffin, W.L., O'Reilly, S.Y., Natapov, L.M., Ryan, C.G., 2003. The evolution of lithospheric mantle beneath the Kalahari Craton and its margins. Lithos 71, 215–241.

Grütter, H.S., Apter, D.B., Kong, J., 1999. Crust-mantle coupling: evidence from mantle-derived xenocrystic garnets, in: Gurney, J.J., Gurney, J.L., Pascoe, M.D., Richardson, S.H. (Eds.), Proceedings of the 7th

International Kimberlite Conference. Red Roof Design, Cape Town, pp. 307–313.

Grütter, H.S., Gurney, J.J., Menzies, A.H., Winter, F., 2004. An updated classification scheme for mantle-derived garnet, for use by diamond explorers. Lithos 77, 841–857.

Hasterok, D., Chapman, D.S., 2011. Heat production and geotherms for the continental lithosphere. Earth and Planetary Science Letters 307, 59–70.

Hirdes, W., Davis, D.W., 1998. First U/Pb zircon age of extrusive volcanism in the Birimian Supergroup of Ghana/West Africa. Journal of African Earth Sciences 27, 291–294.

Javoy, M., 1997. The major volatile elements of the Earth: Their origin, behavior, and fate. Geophysical Research Letters 24, 177–180.

Klein-BenDavid, O., Logvinova, A.M., Schrauder, M., Spetius, Z.V., Weiss, Y., Hauri, E.H., Kaminsky, F.V., Sobolev, N.V., Navon, O., 2009. High-Mg carbonatitic microinclusions in some Yakutian diamonds—a new type of diamond-forming fluid. Lithos 112, Supplement 2, 648–659.

Luth, R.W., 1999. Carbon and carbonates in the mantle, in: Fei, Y., Bertka, C.M., Mysen, B.O. (Eds.), Mantle Petrology: Field Observations and High-pressure Experimentation: a Tribute to Francis R (Joe) Boyd. pp. 297–316.

McDonough, W.F., Sun, S. -s., 1995. The composition of the Earth. Chemical Geology 120, 223–253.

Milési, J.-P., Ledru, P., Feybesse, J.-L., Dommanget, A., Marcoux, E., 1992. Early proterozoic ore deposits and tectonics of the Birimian orogenic belt, West Africa. Precambrian Research 58, 305–344.

Palme, H., O'Neill, H.S.C., 2007. Cosmochemical Estimates of Mantle Composition, in: Holland, H.D., Turekian, K.K. (Eds.), The Mantle and Core, Treatise on Geochemistry. Pergamon, Oxford, pp. 1–38.

Phillips, D., Harris, J.W., Viljoen, K.S., 2004. Mineral chemistry and thermobarometry of inclusions from De Beers Pool diamonds, Kimberley, South Africa. Lithos 77, 155–179.

Richardson, S.H., Gurney, J.J., Erlank, A.J., Harris, J.W., 1984. Origin of diamonds in old enriched mantle. Nature 310, 198–202.

Richardson, S.H., Shirey, S.B., Harris, J.W., Carlson, R.W., 2001. Archean subduction recorded by Re–Os isotopes in eclogitic sulfide inclusions in Kimberley diamonds. Earth and Planetary Science Letters 191, 257–266.

Stachel, T., Harris, J.W., 1997. Syngenetic inclusions in diamond from the Birim field (Ghana) - a deep peridotitic profile with a history of depletion and re-enrichment. Contributions to Mineralogy and Petrology 127, 336–352.

Taylor, P.N., Moorbath, S., Leube, A., Hirdes, W., 1992. Early Proterozoic crustal evolution in the birimian of Ghana: constraints from geochronology and isotope geochemistry. Precambrian Research 56, 97–111.

Taylor, W.R., Green, D.H., 1989. The role of reduced COH fluids in mantle partial melting, in: Kimberlites and Related Rocks, Special Publication. Geological Society of America, Boulder, pp. 592–602.

Chapter 2 – Trace-elements in gem diamond from Akwatia, Ghana and De Beers Pool, South Africa

The content of this chapter, in part, has been published as: Melton, G.L., McNeill, J., Stachel, T., Pearson, D.G. and Harris, J.W., 2012, Trace-elements in gem diamond from Akwatia, Ghana and De Beers Pool, South Africa. Chemical Geology, v 314-317, p. 1-8.

2.1. Introduction

Investigations into the provenance of mantle-derived diamonds through direct analysis of their trace-element contents have historically been obstructed by analytical limitations relating mainly to exceedingly low concentrations of these elements in diamond. The first quantitative measurements of trace-elements in diamond were obtained by Raal (1957), who determined impurity abundances at low ppm levels using optical emission spectroscopy. These results may, however, have been influenced by the presence of minute mineral inclusions. Fesq et al. (1973; 1975) quantitatively determined 40 elemental impurities in diamonds from South Africa using instrumental neutron activation analysis (INAA) and observed a correlation between color and diamond chemistry, affecting elements commonly associated with mafic and ultramafic magmas. Fesq et al. (1975) concluded that these elemental impurities, therefore, reside in trapped melt inclusions that apparently also may influence diamond coloration.

The advent of laser ablation inductively coupled mass spectrometry (LA-ICPMS) opened up the possibility to quantify trace-element concentrations

in diamond in situ and with high spatial resolution (Rege et al., 2005) with application initially to trace-element rich fibrous and cloudy diamonds (Tomlinson et al. 2005) and recently to gem diamonds (Araújo et al., 2009; McNeill et al., 2009). Using an on-line LA-ICPMS method, Rege et al. (2010) measured 36 elements in 538 samples from 27 locations worldwide and presented a new model for the origin of gem diamonds. Rege et al. (2010) suggested that gem diamonds precipitate from hydro-silicic high-density fluids that acquired a unique trace-element signature (e.g. low light rare earth elements over heavy rare earth elements (LREE/HREE) and negative Sr and Y anomalies) through immiscible separation from a parental carbonatite-silicate fluid/melt. They propose that subcalcic garnets, which have been shown to be closely associated with diamond (e.g., Gurney 1984), equilibrated with the highly LREE enriched residual carbonatitic melt fraction. An integral part of this new model is the assumption that, similar to fibrous and cloudy diamonds, elemental impurities in gem diamond are hosted by trapped fluid/melt inclusions, and therefore, the trace-element ratios in diamond and its growth medium are the same.

For gem diamonds from Akwatia (Ghana) and De Beers Pool (South Africa), I will explore the establishment of equilibrium between these diamonds and their garnet inclusions based on their trace-element contents and then investigate the potential for elemental impurities in diamond residing (1) in melt inclusions, (2) in the diamond lattice and (3) in dispersed sub-microscopic mineral inclusions.

2.2. Methods

Trace-element concentrations in monocrystalline gem-quality diamonds were determined using an ‘off-line’ LA-ICP-MS method developed at Durham University (McNeill et al., 2009). Samples were ablated off-line

with a 213 nm New Wave Nd:YAG laser in an enclosed PTFE cell. The laser operated at 20 Hz and produced an energy density of 5 J/cm^2 to 6 J/cm^2 with a 160 μm spot size.

Diamond samples were prepared by being washed in an ultrasonic bath with an ultra-pure 16N HNO_3 - 29N HF solution, rinsed in Milli-Q water, then washed in 6N HCl and allowed to dry at 100^{o}C. The custom-made PTFE ablation cell was prepared by leaching in HCl at 120^{o}C for 48 h then 16N HNO_3 for 24 h followed by a Milli-Q water bath. Finally it was put in ultra-pure 6N HCl for 48 h before being loaded with the diamond sample.

A 500 μm x 500 μm area was rastered for 180 min with ablation depths varying between 200 μm and 400 μm. Ablation pits were sharp sided, with minimal graphitization. After ablation, the cell was opened in a Class 10 HEPA-filtered environment and leached with 6N HCl. Details of the post-ablation extraction process are given by McNeill et al. (2009). Leaching products were collected, dried down, and then digested with 3% ultra-pure HNO_3 for introduction into the ICP-MS. All samples were weighed to a precision of 0.1 μg before and after the ablation process and the weight difference was used to quantify trace-element concentrations (McNeill et al., 2009).

Twenty seven isotopes (24 elements) were measured using a Thermo Scientific ELEMENT 2 double focusing magnetic sector-field ICP-MS: ^{47}Ti, ^{48}Ti, ^{49}Ti, ^{85}Rb, ^{88}Sr, ^{89}Y, ^{90}Zr, ^{93}Nb, ^{133}Cs, ^{137}Ba, ^{139}La, ^{140}Ce, ^{141}Pr, ^{143}Nd, ^{147}Sm, ^{149}Sm, ^{151}Eu, ^{157}Gd, ^{159}Tb, ^{161}Dy, ^{166}Er, ^{172}Yb, ^{175}Lu, ^{179}Hf, ^{208}Pb, ^{232}Th, ^{238}U. Operating conditions of the ICP-MS were the same as described in McNeill et al. (2009). A calibration line was established by at least six points from 1000x and 5000x diluted solutions of USGS standards AGV-1, BHVO-1 and W2. The dilution resulted in standard concentrations

close to those expected for gem-quality diamonds. Multiple blanks were analyzed to establish an a priori limit of quantification (LOQ = $10\sigma_{blank}$) that is constant for all samples (McNeill et al., 2009). Table 2.1 shows count rate ranges, medians and standard deviation for samples and a 3% wash blank solution for Ti, Ce and Eu.

	cps (samples)			cps (blank)	
	Min	Max	Median	Median	s.d
Ti	6922	30959	13870	1847	318
Ce	328	178540	2404	39	94
Eu	144	505	193	164	20

Table 2.1. Sample count rate ranges, medians and 3% wash blank medians and standard deviations for Ti, Ce and Eu.

2.3. Samples

The diamonds from this work originate from two distinct cratons in the African continent. Ghanaian diamonds studied herein come from the alluvial deposits of the Birim Diamond Field, near Akwatia, on the West African Craton. The diamonds are weathered from metakimberlites of the Birimian Supergroup (~2 Ga) (McKitrick et al., 1993; Appiah et al, 1996). De Beers Pool samples come from the cumulative production of four kimberlites on the De Beers property in Kimberly, South Africa. These kimberlites intruded into the Kaapvaal craton at ~84 Ma (Allsopp et al., 1989).

All samples are fragments of diamonds that were previously studied for their mineral inclusion content (Stachel and Harris 1997a and b; Phillips et al. 2004; Banas et al. 2009). The fragments are from gem-quality (i.e. fully transparent) monocrystalline diamonds with octahedral primary morphologies and are either colorless or have a very faint brownish

coloration. In preparation for ICP-MS analysis, sample fragments were screened based on size and shape and only large and flat (cleavage) fragments were chosen. A large (≥ 1.7 mm) fragment size is necessary to maximize the amount of potential ablation product and to avoid sample movement ("jumping" of grains) during laser beam impact. Because of the extremely low trace-element contents in our samples, a previous analytical attempt via direct (on-line) laser ablation ICPMS in a different laboratory resulted in signals below or near the limit of detection and invariably distinctly below the limit of quantification.

A major-element study on garnet inclusions in diamonds from Akwatia, Ghana (Stachel and Harris, 1997a) revealed that they are principally of harzburgitic paragenesis (~80% of all garnets and 84% of peridotitic garnets). Olivine and orthopyroxene Mg number modes are 93.0 and 93.5, respectively, and average Cr_2O_3 in chromite inclusions is high compared to a worldwide database. Garnet-opx geothermobarometry results in a range from 1100ºC to 1370ºC at 5.0 GPa to 6.7 GPa (Stachel and Harris, 1997a). The combined results of all geothermobarometric data indicate a slightly deeper and hotter origin than typically observed for peridotitic diamonds worldwide (Stachel and Harris, 2008). Of particular interest, Stachel and Harris (1997a) observed a high knorringite ($Mg_3Cr_2Si_3O_{12}$) component and a slight excess of Si per formula unit in garnet sample G303-305, supporting the interpretation of an unusually deep lithospheric origin for some of the samples from Akwatia.

Trace-element partitioning between garnet and clinopyroxene inclusions occurring together in two Akwatia diamonds is consistent with experimentally determined partition coefficients, establishing that the inclusions are in equilibrium (Stachel and Harris, 1997b). Harzburgitic garnet inclusions show systematically lower concentrations of Ti, Y, Zr,

HREE, and higher LREE than those from lherzolitic samples (Stachel and Harris, 1997b). These differences imply that the source of lherzolitic garnets was affected by a metasomatic agent comparatively rich in high field strength (HFSE) such as Ti, Zr, Hf and Y and with moderate LREE/HREE, characteristics typically associated with melt metasomatism (Stosch and Lugmair, 1986; Menzies et al., 1987, Stachel et al. 2004). Harzburgitic inclusions, however, bear the characteristics of a source that was overprinted by a highly fractionated C-H-O fluid with very high $LREE_N$/$HREE_N$ (Stachel and Harris, 1997b) and low other HFSE (Ti, Zr, Hf and Y) (Eggler, 1987).

The De Beers Pool samples come from a population of 425 inclusion-bearing diamonds (Phillips et al., 2004). Garnet inclusion compositions reflect strongly depleted sources with 94% of peridotitic garnets being harzburgitic, 78% of which have CaO < 2 wt % (Phillips et al., 2004). High Cr_2O_3 in chromites (up to 68 wt%), high Mg-numbers for olivines and orthopyroxenes (93 to 97) and low Ca concentrations in garnets provide further evidence for highly depleted, Cr-rich sources (Phillips et al., 2004). Temperature and pressure estimates range from 1080ºC to 1320ºC at 4.6 GPa to 7.7 GPa (Phillips et al., 2004). A trace-element study (Banas et al., 2009), based on a subset of the garnet inclusions suite of Phillips et al. (2004), showed that despite their highly-depleted, major-element signature, inclusions in De Beers Pool diamonds invariably reflect metasomatic re-enrichment of incompatible trace-elements. Garnets from the diamonds selected for our study fall into the low TiO_2 (<0.02 wt%) group of Banas et al. (2009) and have sinusoidal or “humped” chondrite normalized REE patterns, with the exception of DBP457, containing a high-Ti garnet (TiO_2 = 0.06 wt%) with weakly sinusoidal REE_N.

2.4. Results

Concentrations of trace-elements in diamonds from Akwatia and De Beers Pool are generally very low and fall in the ppm to ppt range, with most analyzed elements being < 100 ppb (Table 2.2). Ti, Ba and Sr are the only elements to exceed 1 ppm in at least one sample, although Sr is very variable (0.05 to 9.3 ppm) and Ba is detected for sample DBP457 only. A variation of one to two orders of magnitude over the whole sample suite is observed for Eu, Pr, Gd, Tb, Ce, La, Dy, Y, Sr and U (in order of increasing variability), whilst Ti, Zr, Nb, Sm, Hf and Th vary by less than an order of magnitude. DBP457 is the only sample with quantifiable amounts of Ba, Rb, Cs, Yb, Lu and Pb. Conversely, sample DBP406 has no elemental data above the limit of quantification with the exception of Ti. Nd, a REE with relatively high natural abundance, is below the limit of quantification in all samples. This is likely a consequence of a comparatively high LOQ for Nd resulting from an instrumental problem during analyses.

Chondrite-normalized trace-element patterns are incomplete for most samples but an overall trend of only modest enrichment of LREE over MREE is present: Ce_N/Eu_N ranges from 1.2 to 5.7 (average 2.7). Of the three samples with fairly complete REE_N patterns, G103 and G201 have smooth REE_N with negative $LREE_N$-$HREE_N$ slopes (Figure 2.1); DBP457 shows an irregular pattern from Sm_N to Y_N and overall flat $MREE_N$ to $HREE_N$. Large ion lithophile elements (LILE) and non-REE HFSE analyses above the limit of quantification are also sparse; the present data show minor inter-elemental variations with the one exception of DBP457, which has Ba_N and Sr_N two orders of magnitude higher than Ti_N, Zr_N and Hf_N. DBP457 is overall unique and does not even remotely match the trace-element patterns observed for the other nine samples in this study.

	G50	2σ	G103	2σ	G113	2σ	G201	2σ	G303	2σ	DBP 014	2σ	DBP 032	2σ	DBP 398	2σ	DBP 406	2σ	DBP 457	2σ	Aver. lherz.	1σ	Aver. harz.	1σ
Para.	l		h		l		l		h		h		h		h		h		h					
Ti (ppm)	6.61	1.83	1.68	0.52	1.68	0.23	5.64	0.52	6.48	1.23	6.04	1.85	1.17	0.06	5.4	0.29	7.2	0.42	6.0	2.66	4.64	2.61	5.26	2.38
Rb																			216	16.1				
Sr							108	7.95					46	2.47					9315	405				
Y			3.16	0.52			3.01	0.88											307	9.24				
Zr											85.1	15.4							150	22.6				
Nb			2.18	0.09															4.4	1.12				
Cs																			25.5	0.99				
Ba																			5998	166				
La			42.3	3.0			3.07	0.25			4.67	1.08	81.5	6.26					85.4	1.95			43.1	54.3
Ce	5.39	0.63	60.6	2.17			10.1	0.72			34.5	2.66			14.9	0.3			102	3.45	7.74	3.33	24.7	13.9
Pr			4.88	0.32			1.38	0.24											17.1	0.62				
Nd																								
Sm			2.32	1.2			2.58	1.01											17.6	1.33				
Eu	0.24	0.18	0.98	0.35	0.36	0.41	0.8	0.4	0.84	0.45			0.33	0.4	1.01	0.69			2.9	0.72	0.46	0.29	0.73	0.35
Gd			1.41	1.04			1.57	0.69											22.5	2.21				
Dy			0.91	0.47			0.61	0.13											19.3	3.76				
Er			0.4	0.05															12.4	2.07				
Yb																			10.4	2.64				
Lu																			1.5	0.3				
Hf											1.92	0.75							3.0	0.6				
Pb																			762	41.7				
Th			5.91	0.36															12.4	0.61				
U			9.01	0.12	0.14	0.04													29.0	1.42				
Tb			0.22	0.05			0.23	0.05											3.6	0.15				
Mass loss (mg)	0.28		0.31		0.31		0.33		0.13		0.12		0.28		0.12		0.12		0.26					

Table 2.2. Trace-element concentrations in gem quality diamond from De Beers Pools (DBP), South Africa and Akwatia, Ghana (G). All concentrations, including 2σ uncertainty, are reported in ppb unless otherwise noted. LOQ for Ce, Eu,and Ti (the elements with the most analyses above LOQ) are 1.6, 0.2 and 49 ppt, respectively (McNeill et al., 2009; unpublished data). Parageneses are lherzolitic (l) and harzburgitic (h) as reported by Stachel and Harris (1997a,b), Phillips et al. (2004) and Banas et al. (2009). Averages for the harzburgitic samples exclude DBP457 and G103 (see text).

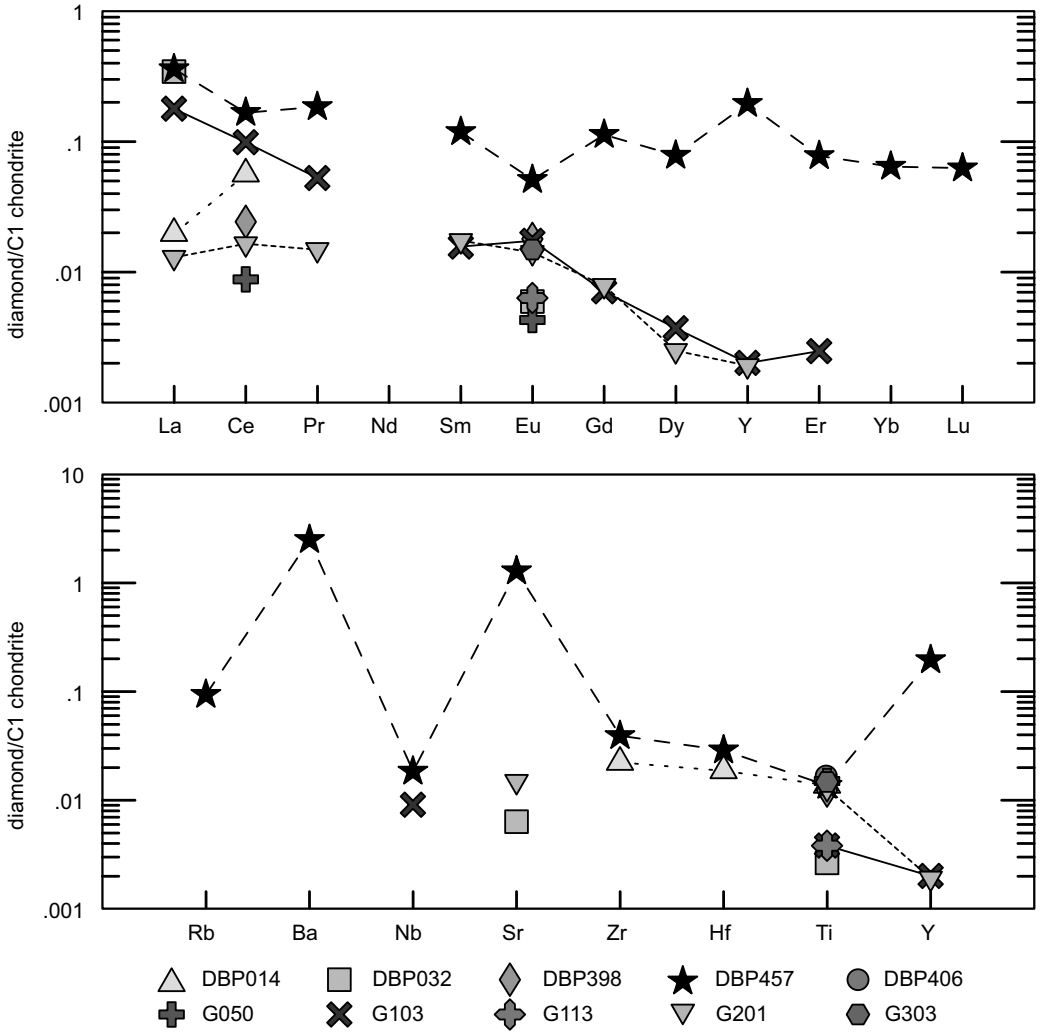

Figure 2.1. C1 chondrite (composition of McDonough and Sun, 1995) normalized REE and HFSE patterns for gem diamond samples from De Beers Pool (Kimberley area, South Africa) and Akwatia (Birim diamond fields, Ghana).

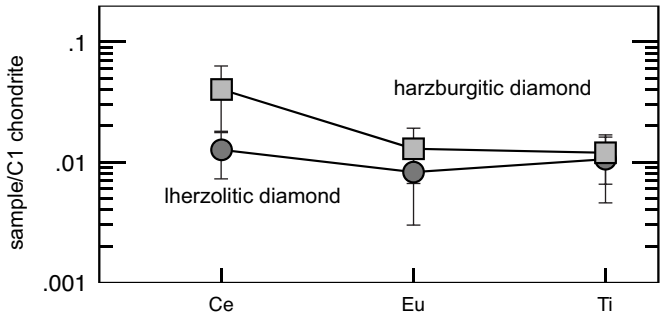

Figure 2.2. Average lherzolitic and harzburgitic diamond compositions normalized to C1 chondrite with 1σ bars.

Averages based on paragenesis established from garnet inclusion analyses (Stachel and Harris 1997b; Banas et al., 2009), excluding G103 and DBP457, were calculated for the three elements that were found to be above the limit of quantification for at least four of the 10 analyzed diamonds (Ti: n=8; Ce: n=4; Eu: n=6) (Figure 2.2). Samples G103 (see section 5.1) and sample DBP457 were excluded from these averages because of their unusual composition, high trace-element concentrations and unique inter-elemental relationships. The average harzburgitic diamond has higher Ce_N (by a factor of 3.2) than the average lherzolitic diamond whereas Eu_N and Ti_N overlap considerably when accounting for standard deviation (Table 2.2).

2.5. Discussion

2.5.1. Melt inclusions in G103

The REE_N pattern for G103 is fairly complete and shows the highest $LREE_N/HREE_N$ of all diamonds analyzed in this work. A La_N/Y_N of 89 in sample G103 sharply contrasts with values of 2 and 7 in the other samples (DBP457 and G201, respectively) where these elements were detected. The trace-element pattern of G103 agrees well with that of low-Mg carbonatitic melt inclusions measured in the outer fibrous coat of sample ON-KAN-381 from Kankan, Guinea (Weiss et al., 2009). The REE_N concentrations of ON-KAN-381 can be superimposed on G103 (Figure 2.3) if the former values are diluted by a factor of 40,000, implying a low modal abundance (~25 wt. ppm) of melt inclusions.

Disseminated melt inclusions at such a concentration level may affect the transparency of sample G103 (which is not observed). Light scattering by nanometer sized particles contained within diamond (Rayleigh scattering) was calculated to constrain qualitatively the maximum permissible size of the melt inclusions (at the given concentration level of 25 ppm) using

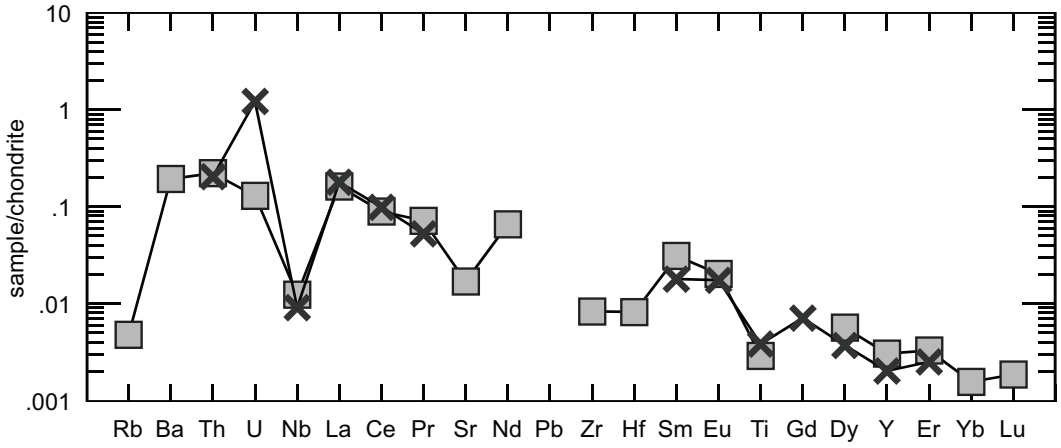

Figure 2.3. C1 chondrite normalized trace-element plot of sample G103 (squares) and ON-KAN-381 (crosses, Weiss et al., 2009). The trace-element concentrations of the fibrous Kankan diamond has been diluted by a factor of 40,000 in order to be superimposed on G103.

equation 3 from Elim et al. (2011) for spherical inclusions with diameters between 1 and 80 nm. I assumed a bulk index of refraction of 1.6 (average carbonate) for the melt inclusions and constrained the maximum Rayleigh ratio for fully transparent diamond to 0.007 cm^{-1} (Elim et al., 2011).

Rayleigh scattering strongly increases with decreasing wavelength of the incident light. Therefore, within the visible light spectrum, a maximum permissible particle size for fully transparent diamond is obtained by looking at light of 400 nm wavelengths. With these (approximate) constraints, for diamond G103 the carbonatitic melt inclusions cannot exceed 25 nm in diameter without affecting transparency.

Sample G103 is, however, distinct from all other samples, which have significantly lower $LREE_N/HREE_N$ and $LREE_N/MREE_N$ implying a different host for their trace impurities and requiring a different explanation.

2.5.2. Garnet fluid/melt modeling

To test further the possibility that trace-element impurities in diamond are contained in trapped melt pockets (Fesq et al. 1975), I converted garnet inclusion data (Stachel and Harris 1997b; Banas et al., 2009) for the analyzed diamond samples into hypothetical equilibrium fluid/melt compositions. Unfortunately, data collected for three known peridotitic gem diamonds by McNeill (2011) cannot be incorporated into this modeling as too much of the data is below the LOQ to be of use. Garnet/liquid partition coefficients for all important trace-elements are available for garnet/basalt (Johnson, 1998) and garnet/carbonatite (Dasgupta et al., 2009). These two partition coefficient datasets produce models that cover two principal end-members of metasomatic melts in the mantle. I exclude the garnet inclusion from sample G303 from the trace-element modeling because of its unusually deep origin, that may link unusually high $LREE_N/HREE_N$ to a possible pressure effect on partition coefficients (Stachel and Harris, 1997b).

A comparison of these calculated fluid/melt compositions with the host diamond analyses rests on the assumption that garnet inclusions and host diamonds are syngenetic and precipitated from or re-crystallized in equilibrium with the same fluid/melt. Irrespective of whether diamond inclusions belong to the peridotitic or eclogitic diamond growth environment, they commonly show negative diamond morphologies (Harris and Gurney, 1979; Meyer 1987). The most common shapes for these inclusions are cubo-octahedron with lesser octahedra and cube (Sobolev, 1977). Detailed X-ray studies show that the inclusions belonged to their normal crystal system despite the imposed morphology (Sobolev, 1977 and references therein). These studies also reveal crystallographic orientation between the diamond and inclusion, or deviation within the limits permitted by the rules of epitaxy and topotaxy (Harris 1968).

Furthermore, growth zones within diamond are typically observed to be cross-cut by, as opposed to wrapping around, their inclusions (Bulnova, 1995). The evidence, therefore, is that diamond externally imposes a morphologic control and internally provides a template for a preferred structural orientation for its inclusions during a period of mutual growth.

Trace-element concentrations in the basaltic and carbonatitic model melts are one to four orders of magnitude higher than in the respective host diamonds, which may well reflect dilution of the melt inclusions in the diamond matrix. For this reason, element ratios are used in the subsequent discussion instead of absolute concentrations. Ce_N/Eu_N can be used as a proxy for $LREE_N/MREE_N$ and Ce_N/Ti_N signifies the enrichment of LREE over a mildly incompatible HFSE, typically associated with melt metasomatism.

Diamond analyses and garnet-based model fluids/melts are plotted in Figure 2.4 together with melt compositions calculated from a worldwide database of peridotitic garnet inclusions. Melts calculated from Akwatia and De Beers Pool garnet inclusions overlap with worldwide values (calculated using the garnet inclusion trace-element data base of Stachel et al. 2004) and show a clear compositional dependence on paragenesis. Melts calculated for lherzolitic garnet inclusions have lower Ce_N/Eu_N and Ce_N/Ti_N ratios than their harzburgitic counterparts, indicating the lherzolitic inclusions were in equilibrium with a less fractionated fluid or melt. This observation has been related to a transition from melt metasomatism for lherzolitic diamond sources to fluid metasomatism for harzburgitic sources (Stachel et al., 1998).

Comparing the analyzed diamonds with fluids/melts modeled from garnet inclusions shows that two harzburgitic diamonds (DBP457 and G103)

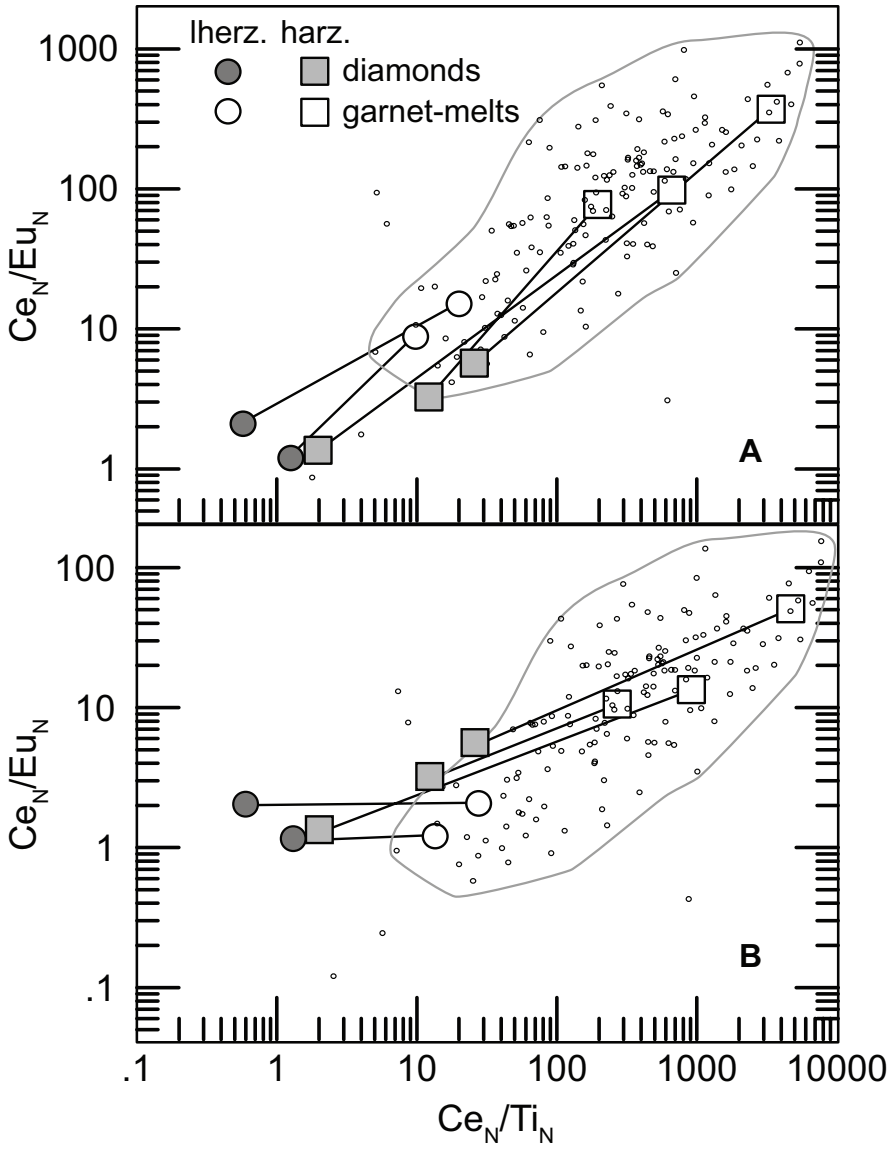

Figure 2.4. Trace-element ratio plot for lherzolitic (circles) and harzburgitic (squares) diamonds (filled) and basaltic (a) and carbonatitic (b) fluid/melt (open) calculated from garnet inclusions within them (matching diamond-melt pairs are connected with a tie line). The small black circles represent modeled fluids/melts in equilibrium with peridotitic garnets from worldwide sources. The outline contains 95% of the calculated melt compositions.

plot at the lower end of the basaltic and carbonatitic melt fields in Figure 2.4. The other harzburgitic (DBP398) and the lherzolitic diamonds (G050 and G201) plot far outside this field for both melt types at very low Ce_N/Ti_N ratios. In addition, a clear compositional separation between lherzolitic

and harzburgitic diamonds, as seen for the garnet inclusions and the melt compositions modeled from them, is not observed in the diamonds. Most importantly, the $LREE_N/MREE_N$ and $LREE_N/Ti_N$ fractionation in the basaltic model melts (Figure 2.4a) is one to three orders of magnitude greater than observed for the respective host diamonds.

Based on carbonatitic model melts (Figure 2.4b), the same comparison also shows one to three orders of magnitude difference in $LREE_N/MREE_N$ and $LREE_N/Ti_N$ ratios in the harzburgitic diamonds. The lherzolitic diamonds display better agreement in Ce_N/Eu_N ratios, but still vary by more than a factor of 10 in Ce_N/Ti_N ratios. With the exception of the latter observation, the overall large differences in Ce_N/Eu_N and Ce_N/Ti_N clearly imply that fluids/melts reflected in garnet inclusion compositions are not the principal source of trace-element impurities in the host diamonds.

The good match in Ce_N/Eu_N between the two lherzolitic diamonds (G50 and G201) from Akwatia and their associated carbonatitic model melts must be viewed with caution. It is very unlikely that these lherzolitic diamonds precipitated from carbonatites: equilibration conditions of clinopyroxene inclusions (1190˚C and 53kbar are obtained for both diamonds, applying the equations of Nimis and Taylor, 2000) suggest diamond precipitation occurred at least 50˚C above the wet solidus of lherzolite (Kessel et al. 2005 and references therein). This implies that any carbonatitic component present should have been diluted by a silicate melt component, and hence the first model (Figure 2.4a) likely is more realistic.

The above comparisons demonstrate that if trace-element impurities in diamond were accommodated as trapped fluids/melts, these fluids/melts never equilibrated with the garnet inclusions in the same diamonds. Besides this discrepancy between garnet and host diamond compositions,

the low $LREE_N/MREE_N$ and $LREE_N/Ti_N$ of the analyzed diamonds cannot be matched to the composition of possible low volume fluids/melts in equilibrium with cratonic garnet peridotite (Thompson et al., 1984; Pearson et al., 2004). All these observations strongly suggest that in the majority of gem-quality diamonds studied here, the trace-elements reside not in fluid/melt inclusions but as part of the diamond lattice, which leads to an elemental fractionation between diamond and the fluid/melt from which it precipitated. This complicates the application of gem diamond trace-elemental signatures to constraining the composition of the diamond-forming fluids.

2.5.3. Trace-elements in the diamond lattice

Instead of being hosted by melt inclusions, trace-elements could be accommodated directly by diamond through defect structures. Some transition metals (Ni and Co) have been observed substituting into synthetic HPHT diamonds (Isoya et al., 1990; Twitchen et al., 2000). Nickel, for example, has a covalent radius that is 57% greater than that of C, nevertheless, concentrations can reach ppm levels in synthetic diamond (Lowther, 1995; Collins et al., 1998; Collins, 2000; Baker, 2003 and references therein). If the trace-elements studied here were accommodated in the diamond structure in a fashion similar to that of Ni in synthetic diamonds, then the unexpectedly low $LREE_N/HREE_N$, could reflect preferential incorporation of HREE into defect structures, based on their smaller ionic radii. Such a behavior should be reflected in the existence of reasonably constant diamond/melt trace-element partition coefficients.

Values for $D^{dia/l}$ calculated from our data set vary, however, by up to three orders of magnitude from sample to sample (Figure 2.5). These partition coefficients were calculated assuming equilibrium with basaltic

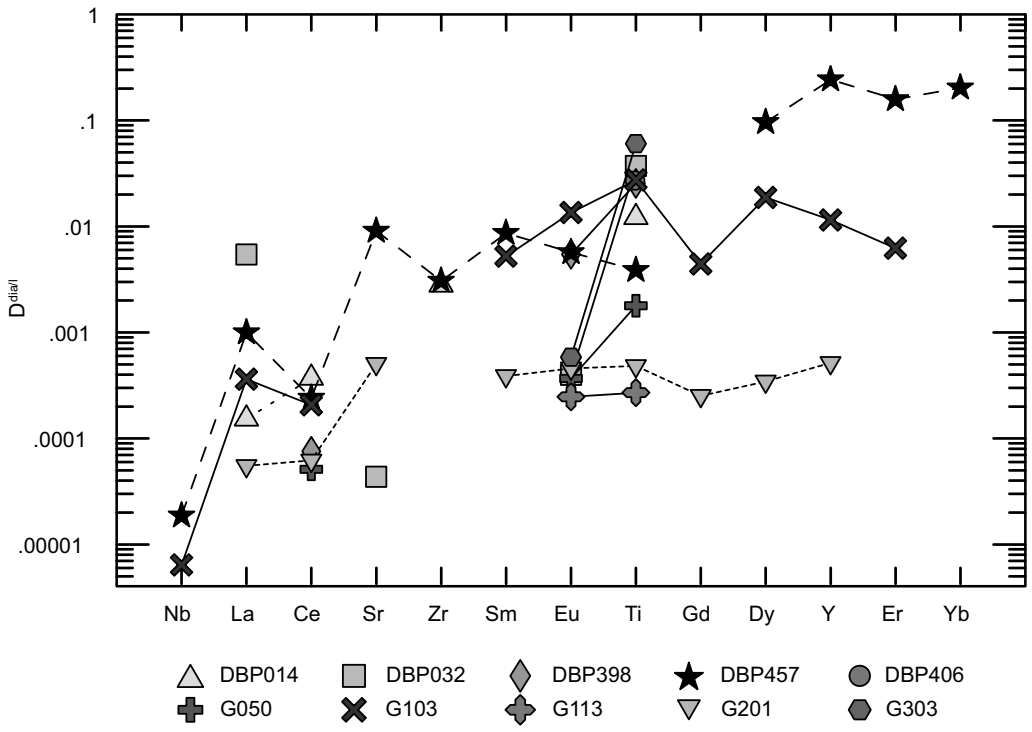

Figure 2.5. Hypothetical partition coefficients ($D^{dia/l}$) for diamond samples and melts calculated from garnet inclusions within them.

melt models calculated from inclusions from each diamond. Variability increases from LREE to HREE: cerium shows the smallest (one order of magnitude) and Y the largest (three orders of magnitude) range in calculated D values. This observation, in addition to the inconsistent inter-elemental relationships, indicate that equilibrium partitioning of trace-elements between diamond and its growth medium is unlikely for the majority of our samples.

2.5.4. Sub-microscopic inclusions

A third possibility to explain the apparently decoupled relationship between the studied diamonds and their garnet inclusions is that trace-elements in diamond are allocated in submicroscopic mineral inclusions. These inclusions could be syngenetic, i.e. precipitating from the diamond-forming melt/fluid, protogenetic, i.e. represent minute fragments of the mantle host

rock, or a combination of both. Bulk distribution coefficients, based on the relative modal proportions of all submicroscopic inclusion phases present in a given diamond chip, would then determine the incorporation of trace-elements. In this scenario, the observed low ratios of LREE to HREE and to Ti would reflect the well established incompatibility of LREE in common mantle minerals.

To test this possibility, I calculated mixtures of common mantle minerals in equilibrium with basaltic and carbonatitic fluid/melt compositions (see above) that would match the relative Ce-Eu-Ti patterns measured in the diamonds. Calculations included olivine, orthopyroxene, clinopyroxene, and garnet, i.e. a garnet lherzolite assemblage. Mg-chromite was not considered because of negligible incorporation of REE. I also evaluated the addition of minor apatite, carbonate, monazite, davidite (REE crichtonite group mineral), and fluid/melt inclusions to the various assemblages in an effort to reproduce elemental ratios observed in the diamonds.

Using the average modal proportions of peridotitic inclusions in diamonds worldwide (Stachel and Harris 2008) and excluding Mg-chromite, the mineral proportions of our initial model were 38% olivine, 40% garnet, 16% orthopyroxene and 6% clinopyroxene. The resulting REE_N pattern for this bulk mixture in equilibrium with melt/fluid modeled from lherzolitic garnets provides a poor match to the average lherzolitic diamond analysis with both Ce_N/Eu_N and Ce_N/Ti_N being < 1. Using lower garnet:cpx ratios and higher modal opx than in the initial model, increases the bulk Ce_N/Eu_N and Ce_N/Ti_N, respectively. To match the observed Ce_N/Ti_N ratio, small proportions of a Ti-bearing phase such as spinel or ilmenite may be included in the models as well (rather than choosing very high modal opx).

The best fit for lherzolitic diamonds is achieved through a mixture of 80% opx, 10% cpx, 10% garnet and 0% olivine. The Ce_N/Eu_N and Ce_N/Ti_N of a melt in equilibrium with this mineral inclusion mix is 1.60 and 1.21, respectively, compared to 1.53 and 1.20 for our average lherzolitic diamond. An inclusion mix of 95.4% opx, 4% garnet and 0.6% cpx and 0% olivine best reproduces the harzburgitic diamond composition, with Ce_N/Eu_N and Ce_N/Ti_N ratios in the equilibrium melt of 2.90 and 3.79, respectively, compared to 3.12 and 3.37 for our average harzburgitic diamond (Figure 2.6).

Incorporation of minor phases such as apatite, carbonate, monazite, davidite and pure fluid/melt were counterproductive in the modeling. These minerals all have strong inter-element fractionation behaviors that drastically affected the models, even in very low proportions. Their effects in the models consistently resulted in poor fits of the average diamond compositions.

Inclusion mixtures were also calculated for a carbonatitic melt environment using partition coefficients for common peridotitic minerals (Dasgupta et al., 2009) as well as apatite and carbonate (Dawson and Hinton, 2003). The best possible fit for our average lherzolitic diamond is achieved using an inclusion mixture of 99% garnet and 1% apatite, resulting in Ce_N/Eu_N of 0.86 (observed: 1.53) and Ce_N/Ti_N of 2.58 (observed 1.20), which clearly is not satisfactory. Mineral proportions for the best fit harzburgitic model are 99.94% garnet and 0.06% apatite with Ce_N/Eu_N of 1.11 (observed: 3.12) and Ce_N/Ti_N of 10.28 (observed: 3.37), respectively, again providing a very poor match (Figure 2.6).

The above calculations indicate that for the minerals employed only inclusion mixture models based on basalt-mineral partition coefficients

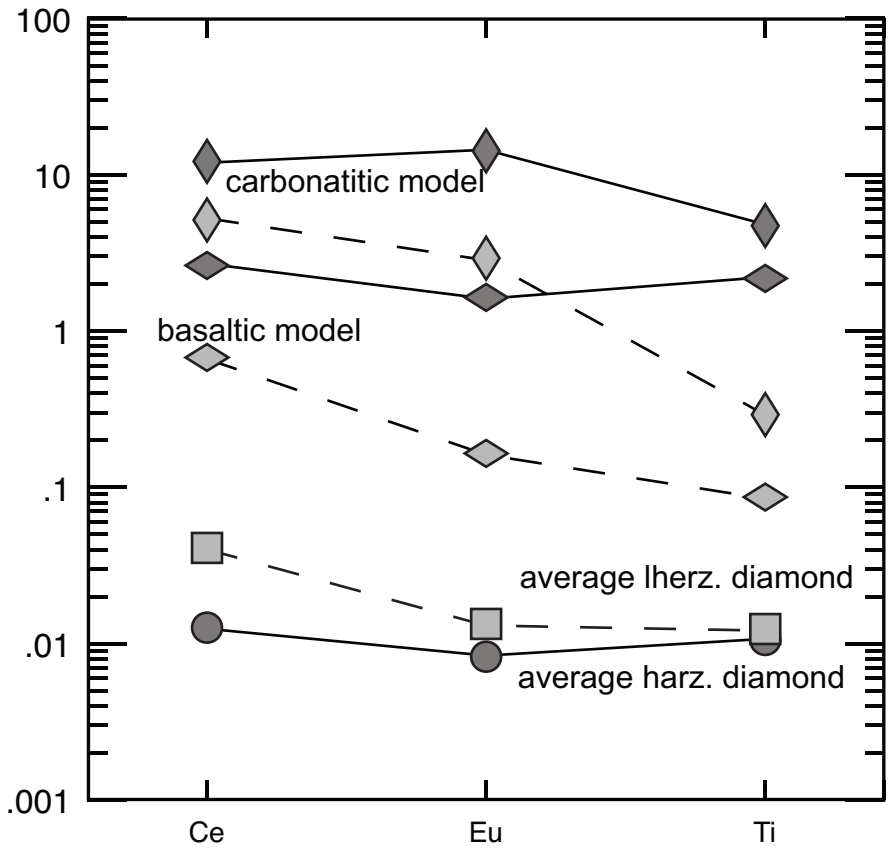

Figure 2.6. Comparison of lherzolitic (circle) and harzburgitic (square) gem diamond element concentrations (normalized to C1 chondrite) and calculated bulk concentrations of mineral inclusion mixtures based on the principal phases in garnet peridotite (olivine, orthopyroxene, clinopyroxene and garnet) for basaltic (horizontal diamonds) and carbonatitic (vertical diamonds) fluids/melts. Basaltic inclusion mixtures provide perfect matches for the diamond trace-element patterns. The approximately two orders of magnitude higher concentrations of the pure inclusion mixtures relative to the diamond analyses indicate the approximate dilution factor. Carbonatitic inclusion mixtures fail to match the diamond patterns.

can provide reasonable fits for the observed trace-element patterns for lherzolitic and harzburgitic diamonds. There are, however, some inconsistencies. Firstly, the mineral proportions in the model mixtures correlate neither with a “normal” peridotitic assemblage (McDonough and Rudnick, 1998) nor with the relative abundance of macro-inclusions in

diamond, (Stachel and Harris, 2008) but instead have no olivine and are dominated by opx.

Secondly, the best fit harzburgitic model contains minor clinopyroxene, which should not be present in this paragenesis. Clinopyroxene in this model provided an addition of Ce without affecting Eu and Ti too adversely. None of the other phases considered in this model gave this result. So although the clinopyroxene is in such low modal abundance, it is necessary for a good fit.

Thirdly, if the calculated inclusion mixtures are diluted in the diamond matrix to match absolute diamond trace-element concentrations, then the resulting inclusion concentrations likely will be too high to be consistent with the transparency of their gem quality hosts. Translucent but non-transparent coats on natural diamonds contain hundreds of ppm to >1% of finely dispersed inclusions (Lang et al., 1995; Weiss et al., 2010). The trace-element concentrations in the calculated mineral inclusion mixtures for lherzolitic diamonds are, greater than the host diamonds by a factor of up to ~500, requiring that ≥ 0.2% of these diamonds should be occupied by inclusions. This would affect transparency for inclusions >1nm in diameter. Reduced transparency is, however, not observed for the studied diamonds. Possible inclusion mixtures, therefore, need trace-element concentrations at least one order of magnitude higher than achievable with the minerals evaluated here. The addition of REE-rich minerals such as apatite (see above) or the LIMA group (Jones and Ekambaram, 1985; Haggerty, 1991**;** Charzot et al., 1996) would lower the required inclusion volume fraction, but at the same time would invariably produce high $LREE_N/HREE_N$, which is not observed. The incorporation of Ti-bearing oxide and silicate (e.g. phlogopite) minerals (Sobolev et al., 2009; Klein-BenDavid et al., 2010) – which cannot be modeled using D-values and

hence were not incorporated in our models – would eliminate the need for a large modal orthopyroxene component and may thereby lower the required volumetric abundance sufficiently to sustain transparency. Therefore, I conclude that accommodation of the trace-element content of gem diamonds in mineral inclusions remains a highly probable explanation, but that the exact modal composition of such inclusion mixtures cannot be constrained based on the relative abundance of only three trace-elements.

2.6. Conclusions

Gem-quality diamonds from De Beers Pool (South Africa) and Akwatia (Ghana), containing peridotitic garnet inclusions, show modest Ce_N/Eu_N ($LREE_N/MREE_N$) and Ce_N/Ti_N ($LREE_N/HFSE_N$) enrichment. Only one sample (G103) shows trace-element ratios compatible with trapping of a low-Mg carbonatitic melt (c.f., Weiss et al 2009). Such melt inclusions cannot exceed 25 nm in diameter without adversely affecting diamond transparency. The absence of significant LREE enrichment in the other peridotitic diamonds implies that their trace-element content cannot represent inclusions of a low volume fluid/melt fraction in equilibrium with normal cratonic garnet peridotite. In addition, fluids/melts calculated from garnet inclusions have no correlations with the analyzed trace-element composition of their host diamonds. This suggests that the trace-element content in gem diamond is not hosted in nano-inclusions of the diamond-forming fluid/melt. Most likely, trace-element patterns of gem diamonds reflect complex and variable mixtures of mineral inclusions instead. In consequence, the composition of gem-diamond-precipitating fluids/melts for all but one diamond analyzed herein from Ghana and De Beers Pool cannot be directly constrained from diamond trace-element analyses.

References

Allsopp, H.L., Bristow, J.W., Smith, C.B., Brown, R., Gleadow, A.J.W., Kramers, J.D., and Garvie, O.G., 1989, A summary of radiometric dating methods applicable to kimberlites and related rocks, in Ross, J. ed., Kimberlites and related rocks, Special Publication - Geological Society of Australia 14, Blackwell Scientific, Carlton, p. 343–357.

Appiah, H., Norman, D.I., and Kuma, J.S., 1996, The diamond deposits of Ghana: Africa Geoscience Review, v. 3, no. 2, p. 261–272.

Araújo, D.P., Griffin, W.L., O'Reilly, S.Y., Grant, K.J., Ireland, T., Holden, P., and van Achterbergh, E., 2009, Microinclusions in monocrystalline octahedral diamonds and coated diamonds from Diavik, Slave Craton: Clues to diamond genesis: Lithos, v. 112, no. Supplement 2, p. 724-735.

Baker, J.M., 2003, Do isolated interstitial nickel atoms occur in diamond? A re-examination of the electron paramagnetic resonance defects NIRIM-1 and NIRIM-2: Journal of Physics: Condensed Matter, v. 15, no. 39, p. S2929-S2940.

Banas, A., Stachel, T., Phillips, D., Shimizu, N., Viljoen, K., and Harris, J., 2009, Ancient metasomatism recorded by ultra-depleted garnet inclusions in diamonds from De Beers Pool, South Africa: Lithos, v. 112, no. Supplement 2, p. 736-746.

Bulanova, G.P., 1995, The formation of diamond: Journal of Geochemical Exploration, v. 53, no. 1–3, p. 1–23, doi: 10.1016/0375-6742(94)00016-5.

Chazot, G., Menzies, M.A., and Harte, B., 1996, Determination of partition coefficients between apatite, clinopyroxene, amphibole, and melt in natural spinel lherzolites from Yemen: Implications for wet melting of the lithospheric mantle: Geochimica et Cosmochimica Acta, v. 60, no. 3, p. 423-437.

Collins, A.T., 2000, Spectroscopy of defects and transition metals in diamond: Diamond and Related Materials, v. 9, no. 3-6, p. 417-423.

Collins, A.T., Kanda, H., Isoya, J., Ammerlaan, C.A.J., and van Wyk, J.A., 1998, Correlation between optical absorption and EPR in high-pressure diamond grown from a nickel solvent catalyst: Diamond and Related Materials, v. 7, no. 2-5, p. 333-338.

Dasgupta, R., Hirschmann, M.M., McDonough, W.F., Spiegelman, M., and Withers, A.C., 2009, Trace-element partitioning between garnet lherzolite and carbonatite at 6.6 and 8.6 GPa with applications to the geochemistry of the mantle and of mantle-derived melts: Chemical Geology, v. 262, no. 1-2, p. 57-77.

Dawson, J.B., and Hinton, R.W., 2003, Trace-element content and partitioning in calcite, dolomite and apatite in carbonatite, Phalaborwa, South Africa: Mineral Mag, v. 67, no. 5, p. 921-930.

Eggler, D.H., 1987, Solubility of major and trace-elements in mantle metasomatic fluids: experimental constraints, in Menzies, M.A. and Hawkesworth, C.J. eds., Mantle Metasomatism, Academic Press, London, p. 21–41.

Elim, H.I., Cai, B., Sugihara, O., Kaino, T., and Adschiri, T., 2011, Rayleigh scattering study and particle density determination of a high refractive index TiO2 nanohybrid polymer: Physical Chemistry Chemical Physics, v. 13, no. 10, p. 4470.

Fesq, H., Bibby, D., Sellschop, J., and Watterson, J., 1973, The determination of trace-element impurities in natural diamonds by instrumental neutron activation analysis: Journal of Radioanalytical and Nuclear Chemistry, v. 17, no. 1, p. 195-216.

Fesq, H., Bibby, D., Erasmus, C., Kable, E., and Sellschop, J., 1975, A comparative trace-element study of diamonds from Premier, Finsch and Jagersfontein mines, South Africa: Physics and Chemistry of The Earth, v. 9, p. 817-836.

Gurney, J.J., 1984, A correlation between garnets and diamonds, in Glover, J.E. and Harris, P.G. eds., Kimberlite Occurrence and Origins: A basis for Conceptual Models in Exploration, University of Western Australia, Perth, p. 143–166.

Harris, J.W., and Gurney, J.J., 1979, Inclusions in diamond, in Field, J.E. ed., The properties of diamond, Academic Press, London, p. 555–591.

Haggerty, S.E., 1991, Oxide mineralogy of the upper mantle: Reviews in Mineralogy and Geochemistry, v. 25, no. 1, p. 355.

Isoya, J., Kanda, H., Norris, J.R., Tang, J., and Bowman, M.K., 1990, Fourier-transform and continuous-wave EPR studies of nickel in synthetic diamond: Site and spin multiplicity: Physical Review B, v. 41, no. 7, p. 3905.

Johnson, K.T.M., 1998, Experimental determination of partition coefficients for rare earth and high-field-strength elements between clinopyroxene, garnet, and basaltic melt at high pressures: Contributions to Mineralogy and Petrology, v. 133, no. 1, p. 60-68.

Jones, A.P., and Ekambaram, V., 1985, New INAA analysis of a mantle-derived titanate mineral of the crichtonite series, with particular reference to the rare earth elements: American Mineralogist, v. 70, no. 3-4, p. 414-418.

Kessel, R., Schmidt, M.W., Ulmer, P., and Pettke, T., 2005, Trace-element signature of subduction-zone fluids, melts and supercritical liquids at 120-180 km depth: Nature, v. 437, no. 7059, p. 724–727.

Klein-BenDavid, O., Pearson, D.G., Nowell, G.M., Ottley, C., McNeill, J.C.R., and Cartigny, P., 2010, Mixed fluid sources involved in diamond growth constrained by Sr-Nd-Pb-C-N isotopes and trace-elements: Earth and Planetary Science Letters, v. 289, no. 1-2, p. 123-133.

Lang, A.R., Vincent, R., Burton, N.C., and Makepeace, A.P.W., 1995, Studies of Small Inclusions in Synthetic Diamonds by Optical Microscopy, Microradiography and Transmission Electron Microscopy: Journal of Applied Crystallography, v. 28, no. 6, p. 690-699.

Lowther, J.E., 1995, Nickel defect centers in diamond: Physical Review B, v. 51, no. 1, p. 91.

McDonough, W.F., Rudnick, R.L., 1998. Mineralogy and composition of the upper mantle. Reviews in Mineralogy, 37, 139-164.

McKitrick, S.A., Norman, D.I., and Appiah, H., 1993, Proterozoic Ghanaian metakimberlites (abs), American Geophysical Fall Meeting, December 6-10, San Fransisco.

McNeill, J., Pearson, D.G., Klein-BenDavid, O., Nowell, G.M., Ottley, C.J., and Chinn, I., 2009, Quantitative analysis of trace-element concentrations in some gem-quality diamonds: Journal of Physics: Condensed Matter, v. 21, no. 36, p. 364207.

McNeill, J.C.R., 2011, New techniques for trace-element and radiogenic isotope measurement of diamonds: their application to diamond petrogenesis and source tracing [PhD]: Durham University, 209 p.

Menzies, M.A., Rogers, N., Tindle, A.G., and Hawkesworth, C.J., 1987, Metasomatic and enrichment processes in lithospheric peridotites,

an effect of asthenosphere-lithosphere interaction, *in* Menzies, M. and Hawkesworth, C. eds., Mantle Metasomatism, Academic Press, London, UK, p. 313-361.

Meyer, H., 1987, Inclusions in diamond, in Nixon, P.H. ed., Mantle Xenoliths, J. Wiley & Sons, Chichester, p. 501–522.

Nimis, P., and Taylor, W.R., 2000, Single clinopyroxene thermobarometry for garnet peridotites. Part I. Calibration and testing of a Cr-in-Cpx barometer and an enstatite-in-Cpx thermometer: Contributions to Mineralogy and Petrology, v. 139, p. 541-554.

Pearson, D.G., Canil, D., Shirey, S.B., 2004. Mantle samples included in volcanic rocks: xenoliths and diamonds. In: R.W. Carlson (Editor), Treatise on Geochemistry. Volume 2: The Mantle and Core. Elsevier-Pergamon, Oxford, pp. 171-275.

Phillips, D., Harris, J.W., and Viljoen, K.S., 2004, Mineral chemistry and thermobarometry of inclusions from De Beers Pool diamonds, Kimberley, South Africa: Lithos, v. 77, no. 1-4, p. 155-179.

Raal, F.A., 1957, A spectrographic study of the minor element content of diamond: American Mineralogist, v. 42, no. 35, p. 361.Rege, S., Griffin, W., Kurat, G., Jackson, S., Pearson, N., and O'Reilly, S.Y., 2008, Trace-element geochemistry of diamondite: Crystallisation of diamond from kimberlite-carbonatite melts: Lithos, v. 106, no. 1-2, p. 39-54.

Rege, S., Jackson, S., Griffin, W.L., Davies, R.M., Pearson, N.J., O'Reilly, S.Y., 2005. Quantitative trace-element analysis of diamond by laser ablation inductively coupled plasma mass spectrometry. Journal of Analytical Atomic Spectrometry, 20(7), 601-611.

Rege, S., Griffin, W., Pearson, N., Araujo, D., Zedgenizov, D., and O'Reilly, S., 2010, Trace-element patterns of fibrous and monocrystalline diamonds: Insights into mantle fluids: Lithos, v. 118, no. 3-4, p. 313-337.

Sobolev, N.V., Logvinova, A.M., and Efimova, E.S., 2009, Syngenetic phlogopite inclusions in kimberlite-hosted diamonds: implications for role of volatiles in diamond formation: Russian Geology and Geophysics, v. 50, no. 12, p. 1234-1248.

Stachel, T., and Harris, J.W., 1997a, Syngenetic inclusions in diamond from the Birim field (Ghana) - a deep peridotitic profile with a history

of depletion and re-enrichment: Contributions to Mineralogy and Petrology, v. 127, p. 336-352.

Stachel, T., and Harris, J.W., 1997b, Diamond precipitation and mantle metasomatism - evidence from the trace-element chemistry of silicate inclusions in diamonds from Akwatia, Ghana: Contributions to Mineralogy and Petrology, v. 129, p. 143-154.

Stachel, T., and Harris, J., 2008, The origin of cratonic diamonds -- Constraints from mineral inclusions: Ore Geology Reviews, v. 34, no. 1-2, p. 5-32.

Stachel, T., Aulbach, S., Brey, G.P., Harris, J.W., Leost, I., Tappert, R., Viljoen, K.S., 2004. The trace-element composition of silicate inclusions in diamonds: a review. Lithos, 77(1-4), 1-19.

Stachel, T., Viljoen, K.S., Brey, G., and Harris, J.W., 1998, Metasomatic processes in lherzolitic and harzburgitic domains of diamondiferous lithospheric mantle: REE in garnets from xenoliths and inclusions in diamonds: Earth and Planetary Science Letters, v. 159, no. 1-2, p. 1-12.

Stosch, H., and Lugmair, G., 1986, Trace-element and Sr and Nd isotope geochemistry of peridotite xenoliths from the Eifel (West Germany) and their bearing on the evolution of the subcontinental lithosphere: Earth and Planetary Science Letters, v. 80, no. 3-4, p. 281-298.

Thompson, R.N., Morrison, M.A., Hendry, G.L., Parry, S.J., 1984. An assessment of the relative roles of crust and mantle in magma genesis - an elemental approach. Philosophical Transactions of the Royal Society of London Series A - Mathematical Physical and Engineering Sciences, 310(1514), 549-590.

Tomlinson, E., De Schrijver, I., De Corte, K., Jones, A.P., Moens, L., Vanhaecke, F., 2005. Trace-element compositions of submicroscopic inclusions in coated diamond: A tool for understanding diamond petrogenesis. Geochimica et Cosmochimica Acta, 69(19), 4719-4732.

Twitchen, D.J., Baker, J.M., Newton, M.E., and Johnston, K., 2000, Identification of cobalt on a lattice site in diamond: Physical Review B, v. 61, no. 1, p. 9.

Weiss, Y., Kessel, R., Griffin, W.L., Kiflawi, I., Klein-BenDavid, O., Bell, D.R., Harris, J.W., and Navon, O., 2009, A new model for the evolution of diamond-forming fluids: Evidence from microinclusion-

bearing diamonds from Kankan, Guinea: Lithos, v. 112, no. Supplement 2, p. 660-674.

Weiss, Y., Kiflawi, I., and Navon, O., 2010, IR spectroscopy: Quantitative determination of the mineralogy and bulk composition of fluid microinclusions in diamonds: Chemical Geology, v. 275, no. 1-2, p. 26-34.

Chapter 3 – Infrared spectral and carbon isotopic characteristics of micro- and macro- diamonds from the Panda kimberlite (Central Slave Craton, Canada)

The content of this chapter, in part, has been published as: Melton, G.L., Stachel, T., Stern, R.A., Carlson, J., Harris, J.W., Infrared spectral and carbon isotopic characteristics of micro- and macro- diamonds from the Panda kimberlite (Central Slave Craton, Canada), 2013, Lithos, v 177, p 110-119.

3.1. Introduction

The Panda kimberlite, Canada's first diamond mine, was mined from 1998 to 2003 as an open cut and from 2005 to 2010 as a sub-level retreat underground operation. The overall ore grade was approximately one carat per tonne. The Panda pipe is located on the Ekati Diamond Mine Property, 25 km north of Lac de Gras, Northwest Territories, Canada. The kimberlite is 53.3 ± 0.6 Ma, based on Rb-Sr dating of macrocrystal phlogopite (Creaser et al., 2004). Diamond source lithologies, established through inclusion studies, are dominantly peridotitic but include a small proportion of eclogitic and rare sublithospheric sources (Stachel et al., 2003; Tappert et al., 2005). These previous studies provided data on inclusion-bearing, gem-quality (i.e. fully transparent) diamonds that measure between 2.5 mm and 3.4 mm.

While most diamond studies from the Central Slave Craton focus on inclusion chemistry, much has been learned through carbon isotope and nitrogen abundance data as well. Inclusion studies have observed that sulfide-bearing diamonds of both peridotitic and eclogitic parageneses

resided in cooler portions of the subcratonic lithospheric mantle (Westerlund et al., 2006; Aulbach et al., 2009). This observation is based on nitrogen concentration and aggregation characteristics that indicate silicate inclusions span a much broader range of residence temperatures (Westerlund et al., 2006). Discrepancies between nitrogen-based temperature estimates and silicate geothermometry have been attributed to cooling below the Slave Craton by 100ºC to 200ºC after ancient (>1 Ga) diamond formation or to heating events (Stachel et al., 2003; Donnelly et al., 2007).

Most diamonds from the Central Slave Craton have a range of $\delta^{13}C$ values similar to typical mantle values of -5‰ ± 2‰ and are attributed to the peridotitic paragenesis (Donnely et al., 2007; Creighton et al., 2008; Aulbach et al., 2009; Cartigny et al., 2009). However, lower $\delta^{13}C$ values (< -8‰) are reported in coats of stones where fibrous overgrowth enclose (typically) octahedral cores (Klein-BenDavid et al., 2007; Araujo et al., 2009) and diamonds of eclogitic paragenesis (Davies et al., 1999; Davies et al., 2004). This detailed study of carbon isotope and nitrogen systematics in diamonds from Panda spanning the size range from micro- to macro-diamonds provides further insights into the diamond-forming environment beneath the Central Slave Craton.

In this study, I report new data on nitrogen and its aggregation states, the hydrogen and platelet peak areas and the isotopic properties of multiple growth zones in 121 micro-diamonds (<1 mm) from the Panda kimberlite (Table 3.1). Additionally, using macro-diamond fragments from the original work of Stachel et al. (2003), I have reproduced the nitrogen characteristics of this diamond dataset and completed hydrogen and platelet peak analyses on all the diamonds (Table 3.2).

3.2. Samples

The Panda “micro-diamonds” here defined as the Diamond Trading Company (DTC) minus 1 sieve class (i.e. passing through 1.1 mm circular aperture), were obtained by sieving and removing that entire fraction from an exploration bulk sample. To minimize sample bias, that fraction was further divided by cone and quartering (bulk sample is poured onto a surface forming a cone, then split into four equal proportions) to obtain 125 samples. Note that subsequently, four samples were lost at various stages of sample preparation (see Table 3.1). Individual sample weights range from 0.40 mg to 3.09 mg (average of 1.30 mg).

3.2.1. Physical characteristics of the diamond datasets

Morphology and color distributions of the micro-diamonds are shown in Table 3.1 and graphically represented in Figure 3.1. Octahedra dominate (40%) with less common dodecahedral (26%) and cuboid (18%) morphologies. The morphology class “other” includes aggregated, twinned and fragmented diamonds. Forty percent of the micro-diamonds are “gem-quality” (i.e. fully transparent) the remainder being cloudy (at least in part). Cloudy diamonds are mildly translucent to opaque and in this instance most of these diamonds are grey (see Figure 3.1). Only in two instances was a distinct “coat” noted, where there was a sharp contact between the inclusion-free core. Similar coated diamonds from the Central Slave Craton have previously been reported (Klein-BenDavid et al., 2004; Tomlinson et al., 2006; Araujo et al., 2009). Additionally, five samples show signs of plastic deformation during mantle residence, denoted by a series of parallel, linear surface features extending across dodecahedral faces. Surface features such as hillocks, etch pits and negative trigons, are common.

Sample	Color	Clarity	Morphology	Wt (mg)	N_{FTIR} (at. ppm)	B_{FTIR} (at. ppm)	Platelet (cm^{-2})	H (cm^{-2})	$\delta^{13}C_{VPDB}$	2σ	N_{SIMS} (at. ppm spot)	Temp 3.5
PMi001a	grey	cloudy	cube	1.70	1205	560		13.35	-2.27	0.18	1301	1101
PMi001b	grey	cloudy	cube	1.70	1205	560		13.35	-2.69	0.19	1235	1101
PMi002a	colorless	clear	octa	1.55	547	517	347.92	31.25	-5.08	0.17	1170	1195
PMi002b	colorless	clear	octa	1.55	547	517	347.92	31.25	-5.10	0.19	66	1195
PMi003a	grey	cloudy	agg (cube)	2.04					-3.84	0.18	86	
PMi003b	grey	cloudy	agg (cube)	2.04					-4.80	0.19	1	
PMi004a	colorless	clear	dodec	3.09	441	364	231.86	15.31	-5.31	0.17	678	1167
PMi004b	colorless	clear	dodec	3.09	441	364	231.86	15.31	-5.38	0.17	203	1167
PMi005a	brown	cloudy	irregular	1.74					-3.08	0.18	1256	
PMi005b	brown	cloudy	irregular	1.74					-2.90	0.17	1122	
PMi006a	colorless	clear	octa	2.21	456	0		4.56	-4.92	0.18	521	
PMi006b	colorless	clear	octa	2.21	456	0		4.56	-6.12	0.19	1552	
PMi006c	colorless	clear	octa	2.21	456	0		4.56	-5.15	0.18	893	
PMi007a	colorless	clear	dodec	1.82	803	226	132.06	0.11	-3.55	0.19	833	1092
PMi007b	colorless	clear	dodec	1.82	803	226	132.06	0.11	-3.50	0.18	943	1092
PMi008a	yellow	clear	octa	1.96	237	176	91.33	15.31	-5.95	0.16	909	1170
PMi008b	yellow	clear	octa	1.96	237	176	91.33	15.31	-5.98	0.16	960	1170
PMi009a	colorless	clear	octa	2.08	896	64	36.92	32.45	-4.82	0.18	773	1053
PMi009b	colorless	clear	octa	2.08	896	64	36.92	32.45	-4.80	0.17	743	1053
PMi010a	grey	cloudy	agg	0.63					-3.51	0.18	1017	
PMi010b	grey	cloudy	agg	0.63					-3.31	0.18	963	
PMi011a	brown	cloudy	cube	2.05					-4.08	0.17	1809	
PMi011b	brown	cloudy	cube	2.05					-4.61	0.18	1497	
PMi012a	grey	cloudy	dodec	0.97					-5.32	0.18	23	
PMi012b	grey	cloudy	dodec	0.97					-5.95	0.18	17	
PMi012c	grey	cloudy	dodec	0.97							179	
PMi013a	colorless	clear	irregular	1.69	642	15	16.37	0.40	-4.86	0.18	778	1035
PMi013b	colorless	clear	irregular	1.69	642	15	16.37	0.40	-4.81	0.19	619	1035
PMi014a	brown	cloudy	agg (cube)	1.35	1074	380		28.11	-4.24	0.18	1776	1093
PMi014b	brown	cloudy	agg (cube)	1.35	1074	380		28.11	-4.24	0.18	1729	1093
PMi015a	brown	cloudy	agg (cube)	0.89	1077	255		20.47	-3.22	0.18	1883	1080
PMi015b	brown	cloudy	agg (cube)	0.89	1077	255		20.47	-3.25	0.17	1888	1080
PMi016a	colorless	clear	octa	2.95	667	91	80.72	0.56	-4.69	0.18	774	1075
PMi016b	colorless	clear	octa	2.95	667	91	80.72	0.56	-4.65	0.18	950	1075

Table 3.1. Micro-diamonds from Panda. Octa = octahedron, agg = aggregate (intergrowths), dodec = dodecahedroid. $Nitrogen_{SIMS}$ spot analyses were measured in the same location on the samples as the $\delta^{13}C$. Temp 3.5 are the time averaged mantle residence temperatures for 3.5 Ga mantle residence based on FTIR measurements. For samples with 0%B and 100%B, a mantle residence temperature cannot be calculated.

Sample	Color	Clarity	Morphology	Wt (mg)	N_{FTIR} (at. ppm)	B_{FTIR} (at. ppm)	Platelet (cm^{-2})	H (cm^{-2})	$\delta^{13}C_{VPDB}$	2σ	N_{SIMS} (at. ppm spot)	Temp 3.5
PMi017a	brown	cloudy	cube	0.73					-4.09	0.20	1551	
PMi017b	brown	cloudy	cube	0.73					-3.93	0.18	1465	
PMi018a	grey	cloudy	cube	1.92					-3.26	0.18	631	
PMi018b	grey	cloudy	cube	1.92					-3.18	0.19	610	
PMi019a	grey	cloudy	dodec	1.60	525	66		1.69	-6.19	0.19	1210	1079
PMi019b	grey	cloudy	dodec	1.60	525	66		1.69	-5.81	0.19	1288	1079
PMi020a	grey	cloudy	dodec	1.35	968	4		8.21	-3.89	0.19	1054	991
PMi020b	grey	cloudy	dodec	1.35	968	4		8.21	-6.69	0.18	475	991
PMi021a	yellow	cloudy	cube	1.46	806	224		15.62	-3.63	0.18	684	1091
PMi021b	yellow	cloudy	cube	1.46	806	224		15.62	-3.60	0.17	698	1091
PMi022a	brown	cloudy	dodec	1.74	570	221			-4.23	0.17	1130	1111
PMi022b	brown	cloudy	dodec	1.74	570	221			-4.25	0.18	1114	1111
PMi023a	grey	cloudy	dodec	1.63	1696	86		34.34	-3.07	0.18	1944	1032
PMi023b	grey	cloudy	dodec	1.63	1696	86		34.34	-3.01	0.19	1882	1032
PMi024a	grey	cloudy	dodec	1.91	1372	477		12.60	-4.96	0.18	1321	1087
PMi024b	grey	cloudy	dodec	1.91	1372	477		12.60	-4.37	0.19	1353	1087
PMi025a	grey	cloudy	cube	1.17					-5.65	0.18	1238	
PMi025b	grey	cloudy	cube	1.17					-4.19	0.17	1210	
PMi026a	grey	cloudy	dodec	2.03					-4.89	0.19	905	
PMi026b	grey	cloudy	dodec	2.03					-4.92	0.18	919	
PMi027a	brown	cloudy	dodec	1.29	366	0		2.63	-4.08	0.19	443	
PMi027b	brown	cloudy	dodec	1.29	366	0		2.63	-3.58	0.17	435	
PMi028a	colorless	clear	dodec	1.20	485	0	10.00	10.46	-4.66	0.17	585	
PMi028b	colorless	clear	dodec	1.20	485	0	10.00	10.46	-4.62	0.18	476	
PMi029a	brown	cloudy	octa	0.76	665	78	10.46	0.27	-3.10	0.18	448	1072
PMi029b	brown	cloudy	octa	0.76	665	78	10.46	0.27	-4.16	0.18		1072
PMi030a	colorless	clear	octa	0.79	357	70	25.71	6.04	-4.87	0.18	116	1100
PMi030b	colorless	clear	octa	0.79	357	70	25.71	6.04	-3.92	0.19	17	1100
PMi031a	colorless	clear	octa	1.07	1025	74	32.33	2.38	-4.58	0.18	1130	1050
PMi031b	colorless	clear	octa	1.07	1025	74	32.33	2.38	-4.46	0.18	867	1050
PMi032a	brown	cloudy	octa	1.51	1073	634		5.84	-2.37	0.21	871	1116
PMi032b	brown	cloudy	octa	1.51	1073	634		5.84	-2.29	0.18	863	1116
PMi033a	grey	cloudy	octa	1.64	884	43	0.73	15.01	-4.74	0.18	1028	1045
PMi033b	grey	cloudy	octa	1.64	884	43	0.73	15.01	-4.87	0.19		1045
PMi034a	grey	cloudy	octa	1.64					-2.90	0.17	205	

Table 3.1 Continued

Sample	Color	Clarity	Morphology	Wt (mg)	N_{FTIR} (at. ppm)	B_{FTIR} (at. ppm)	Platelet (cm^{-2})	H (cm^{-2})	$\delta^{13}C_{VPDB}$	2σ	N_{SIMS} (at. ppm spot)	Temp 3.5
PMi034b	grey	cloudy	octa	1.64					-3.06	0.17	287	
PMi035a	grey	cloudy	dodec	1.21	1245	408		30.46	-5.91	0.18		1087
PMi035b	grey	cloudy	dodec	1.21	1245	408		30.46	-5.80	0.19		1087
PMi036a	grey	cloudy	octa	1.03	893	464		8.13	-1.67	0.19	1061	1113
PMi036b	grey	cloudy	octa	1.03	893	464		8.13	-1.68	0.18	1007	1113
PMi037a	brown	clear	octa	1.29	739	93	30.23	1.13	-4.62	0.18	769	1071
PMi037b	brown	clear	octa	1.29	739	93	30.23	1.13	-4.41	0.17	610	1071
PMi038a	grey	cloudy	octa	1.47					-4.09	0.18	876	
PMi038b	grey	cloudy	octa	1.47					-5.03	0.17	539	
PMi038c	grey	cloudy	octa	1.47					-5.25	0.19	540	
PMi038d	grey	cloudy	octa	1.47					-3.87	0.18	877	
PMi040a	brown	clear	dodec	1.03					-4.10	0.18	801	
PMi040b	brown	clear	dodec	1.03					-4.07	0.17	797	
PMi041a	brown	clear	octa	0.68	873	164	118.48	14.80	-3.86	0.17	824	1078
PMi041a2	brown	clear	octa	0.68	873	164	118.48	14.80			808	1078
PMi041b	brown	clear	octa	0.68	873	164	118.48	14.80	-3.82	0.19	774	1078
PMi041b2	brown	clear	octa	0.68	873	164	118.48	14.80			765	1078
PMi042a	colorless	clear	octa	0.88	777	208	120.78	0.78	-5.47	0.17	505	1091
PMi042b	colorless	clear	octa	0.88	777	208	120.78	0.78	-5.48	0.18	729	1091
PMi043a	grey	cloudy	dodec	1.16	1155	506		32.19	-5.41	0.18	1330	1099
PMi043b	grey	cloudy	dodec	1.16	1155	506		32.19	-5.39	0.17	1491	1099
PMi044a	grey	cloudy	dodec	1.75	614	328			-3.99	0.19	475	1123
PMi044b	grey	cloudy	dodec	1.75	614	328			-5.04	0.18	568	1123
PMi044c	grey	cloudy	dodec	1.75	614	328			-5.03	0.20	576	1123
PMi044d	grey	cloudy	dodec	1.75	614	328			-3.83	0.18	445	1123
PMi045a	grey	cloudy	irregular	0.67	1268	73	100.98	16.19	-4.93	0.18	386	1041
PMi045b	grey	cloudy	irregular	0.67	1268	73	100.98	16.19	-3.62	0.18	452	1041
PMi046a	colorless/grey	clear/cloudy	octa	2.38	823	329	44.36	0.42	-5.25	0.18	839	1104
PMi046b	colorless/grey	clear/cloudy	octa	2.38	823	329	44.36	0.42	-5.06	0.18	1236	1104
PMi047a	grey	cloudy	octa	1.64					-5.36	0.17	1634	
PMi047b	grey	cloudy	octa	1.64					-4.72	0.17	460	
PMi048a	colorless	clear	macle	1.10	0	0			-4.61	0.18	14	
PMi048b	colorless	clear	macle	1.10	0	0			-4.59	0.19	14	
PMi049a	colorless	clear	octa	1.37	0	0		2.05	-1.84	0.19	3	
PMi049b	colorless	clear	octa	1.37	0	0		2.05	-1.24	0.18	18	

Table 3.1 Continued

Sample	Color	Clarity	Morphology	Wt (mg)	N_{FTIR} (at. ppm)	B_{FTIR} (at. ppm)	Platelet (cm^{-2})	H (cm^{-2})	$\delta^{13}C_{VPDB}$	2σ	N_{SIMS} (at. ppm spot)	Temp 3.5
PMi050a	colorless	clear	octa	0.92	466	16	10.97	0.43	-5.07	0.18	676	1051
PMi050b	colorless	clear	octa	0.92	466	16	10.97	0.43	-5.08	0.18	799	1051
PMi051a	colorless	clear	octa	1.77	765	26	39.47	0.36	-4.87	0.18	859	1040
PMi051b	colorless	clear	octa	1.77	765	26	39.47	0.36	-4.86	0.18	893	1040
PMi052a	grey	cloudy	octa	1.37	1058	411		23.62	-5.98	0.18	1397	1097
PMi052b	grey	cloudy	octa	1.37	1058	411		23.62	-6.35	0.18	1620	1097
PMi053a	yellow	cloudy	cube	0.58	687	153		22.57	-2.43	0.18	1102	1088
PMi053b	yellow	cloudy	cube	0.58	687	153		22.57	-2.47	0.18	1088	1088
PMi054a	grey	cloudy	dodec	1.08	933	341		22.43	-3.81	0.18	1608	1097
PMi054b	grey	cloudy	dodec	1.08	933	341		22.43	-4.03	0.17	1624	1097
PMi055a	grey	cloudy	dodec	0.86	704	389			-4.33	0.17	1913	1122
PMi055b	grey	cloudy	dodec	0.86	704	389			-4.49	0.18	1686	1122
PMi056a	colorless	clear	octa	0.83	471	0	7.62	1.22	-5.00	0.18	1363	
PMi056b	colorless	clear	octa	0.83	471	0	7.62	1.22	-4.97	0.19	1051	
PMi057a	brown	cloudy	cube	1.01	1303	316		31.87	-5.57	0.18	1387	1076
PMi057b	brown	cloudy	cube	1.01	1303	316		31.87	-5.74	0.19	1470	1076
PMi058a	grey	cloudy	octa	1.49	1384	212		21.98	-5.81	0.18	1224	1062
PMi058b	grey	cloudy	octa	1.49	1384	212		21.98	-4.19	0.19	1425	1062
PMi058c	grey	cloudy	octa	1.49	1384	212		21.98	-5.81	0.19	1297	1062
PMi058d	grey	cloudy	octa	1.49	1384	212		21.98	-4.22	0.19	1393	1062
PMi059a	grey	cloudy	irregular	1.00	1387	746		27.89	-5.47	0.17	1212	1104
PMi059b	grey	cloudy	irregular	1.00	1387	746		27.89	-5.68	0.18	1606	1104
PMi060a	grey	cloudy	octa	1.33	902	384		28.24	-4.35	0.19	1242	1104
PMi060a2	grey	cloudy	octa	1.33	902	384		28.24			1231	1104
PMi060b	grey	cloudy	octa	1.33	902	384		28.24	-4.54	0.19	1450	1104
PMi061a	brown	cloudy	octa	0.51	662	243		24.48	-4.22	0.19	1005	1105
PMi061b	brown	cloudy	octa	0.51	662	243		24.48	-4.62	0.20	1151	1105
PMi061b2	brown	cloudy	octa	0.51	662	243		24.48			1276	1105
PMi062a	brown	cloudy	dodec	0.73	1284	96		17.08	-2.73	0.20	1423	1046
PMi062b	brown	cloudy	dodec	0.73	1284	96		17.08	-2.81	0.20	1408	1046
PMi063a	colorless	clear	octa	2.07	752	95	74.19	0.62	-3.47	0.19	91	1071
PMi063b	colorless	clear	octa	2.07	752	95	74.19	0.62	-2.95	0.21	1143	1071
PMi063c	colorless	clear	octa	2.07	752	95	74.19	0.62	-3.61	0.20	1578	1071
PMi064a	colorless	clear	octa	1.11	1173	213	19.31	15.90	-4.07	0.22	1665	1070
PMi064b	colorless	clear	octa	1.11	1173	213	19.31	15.90	-4.77	0.23	2231	1070

Table 3.1 Continued

Sample	Color	Clarity	Morphology	Wt (mg)	N_{FTIR} (at. ppm)	B_{FTIR} (at. ppm)	Platelet (cm^{-2})	H (cm^{-2})	$\delta^{13}C_{VPDB}$	2σ	N_{SIMS} (at. ppm spot)	Temp 3.5
PMi064c	colorless	clear	octa	1.11	1173	213	19.31	15.90	-4.61	0.21	782	1070
PMi065a	grey	cloudy	octa	0.62	1064	280		9.68	-2.47	0.21	988	1083
PMi066a	colorless	clear	octa	0.95	64	25	9.01	2.28	-4.92	0.22	63	1165
PMi066b	colorless	clear	octa	0.95	64	25	9.01	2.28	-4.75	0.22	37	1165
PMi067a	brown	clear	octa	0.84	631	162	80.63	0.61	-5.08	0.19	914	1094
PMi067b	brown	clear	octa	0.84	631	162	80.63	0.61	-5.08	0.20	736	1094
PMi068a	grey	cloudy	cube	1.22	966	201		13.56	-5.05	0.21	1041	1079
PMi068b	grey	cloudy	cube	1.22	966	201		13.56	-5.22	0.22	1106	1079
PMi069a	brown	cloudy	dodec	0.66	798	177		12.13	-3.70	0.22	920	1085
PMi069b	brown	cloudy	dodec	0.66	798	177		12.13	-3.63	0.21	816	1085
PMi070a	brown	cloudy	octa	0.83	1054	358		26.91	-2.58	0.22	1045	1092
PMi070b	brown	cloudy	octa	0.83	1054	358		26.91	-3.30	0.21	1331	1092
PMi071a	grey	cloudy	dodec	1.49	664	0		7.17	-2.39	0.19	881	
PMi071b	grey	cloudy	dodec	1.49	664	0		7.17	-2.12	0.20	851	
PMi072a	grey	cloudy	octa	1.10	984	243		23.02	-4.58	0.22	1599	1083
PMi072b	grey	cloudy	octa	1.10	984	243		23.02	-4.31	0.22	1696	1083
PMi073a	colorless	clear	octa	2.75	861	132	84.19	2.33	-3.31	0.22	9	1073
PMi073a2	colorless	clear	octa	2.75	861	132	84.19	2.33			9	1073
PMi073b	colorless	clear	octa	2.75	861	132	84.19	2.33	-2.92	0.22	295	1073
PMi074a	brown	cloudy	dodec	2.02	981	229		16.61	-3.15	0.21	1238	1082
PMi074b	brown	cloudy	dodec	2.02	981	229		16.61	-3.00	0.21	1242	1082
PMi075a	brown	cloudy	cube	1.26	1048	480		27.44	-3.70	0.19	1286	1103
PMi075b	brown	cloudy	cube	1.26	1048	480		27.44	-3.79	0.19	1329	1103
PMi076a	grey	cloudy	cube	1.55	1259	604		12.55	-3.39	0.19	1237	1101
PMi076b	grey	cloudy	cube	1.55	1259	604		12.55	-3.46	0.19	1233	1101
PMi077a	brown	clear	irregular	0.40	404	342	113.99	19.80	-5.47	0.19	40	1173
PMi077b	brown	clear	irregular	0.40	404	342	113.99	19.80	-5.92	0.19	575	1173
PMi078a	brown	clear	octa	2.65	122	76	45.17	22.84	-4.98	0.20	67	1173
PMi078b	brown	clear	octa	2.65	122	76	45.17	22.84	-5.27	0.20	85	1173
PMi079a	colorless	clear	octa	1.87	708	243	49.99	4.17	-3.72	0.19	575	1101
PMi079b	colorless	clear	octa	1.87	708	243	49.99	4.17	-4.10	0.20	709	1101
PMi081a	grey	cloudy	cube	0.59					-5.78	0.19	1425	
PMi081b	grey	cloudy	cube	0.59					-5.86	0.19	1467	
PMi082a	brown	clear	octa	1.12					+1.46	0.19	0	
PMi082b	brown	clear	octa	1.12					-1.80	0.19	56	

Table 3.1 Continued

Sample	Color	Clarity	Morphology	Wt (mg)	N_{FTIR} (at. ppm)	B_{FTIR} (at. ppm)	Platelet (cm^{-2})	H (cm^{-2})	$\delta^{13}C_{VPDB}$	2σ	N_{SIMS} (at. ppm spot)	Temp 3.5
PMi082c	brown	clear	octa	1.12					+1.46	0.20	0	
PMi082d	brown	clear	octa	1.12					+1.42	0.18		
PMi082e	brown	clear	octa	1.12					-1.73	0.18	19	
PMi082f	brown	clear	octa	1.12					+1.61	0.19		
PMi082g	brown	clear	octa	1.12					-1.93	0.18		
PMi083a	brown	cloudy	cube	1.23	817	481		42.85	-5.46	0.20	1274	1122
PMi083b	brown	cloudy	cube	1.23	817	481		42.85	-5.41	0.19	1410	1122
PMi084a	grey	cloudy	cube	1.11					-4.56	0.22	434	
PMi084b	grey	cloudy	cube	1.11					-4.59	0.24	425	
PMi085a	grey	cloudy	cube	0.50	812	127		18.15	-3.16	0.22	1857	1075
PMi085b	grey	cloudy	cube	0.50	812	127		18.15	-5.14	0.22	1578	1075
PMi086a	brown	cloudy	cube	1.24	454	1		0.53	-2.45	0.22	491	994
PMi086b	brown	cloudy	cube	1.24	454	1		0.53	-2.41	0.21	471	994
PMi087a	colorless	clear	irregular	0.98	129	30		6.83	-5.43	0.20	746	1129
PMi087b	colorless	clear	irregular	0.98	129	30		6.83	-6.00	0.19	335	1129
PMi088a	grey	cloudy	cube	0.60	1418	155		25.93	-4.48	0.22	1441	1053
PMi088b	grey	cloudy	cube	0.60	1418	155		25.93	-4.51	0.22	1276	1053
PMi089a	colorless	clear	octa	1.83	51	49		8.03	-4.34	0.22	3	1271
PMi089b	colorless	clear	octa	1.83	51	49		8.03	-4.30	0.22	7	1271
PMi090a	grey	cloudy	dodec	1.62	580	141			-2.67	0.22	929	1095
PMi091a	grey	cloudy	dodec	2.10					-3.96	0.19	430	
PMi091b	grey	cloudy	dodec	2.10					-3.06	0.19	364	
PMi092a	grey	cloudy	dodec	1.21	1373	255		28.47	-5.18	0.23	1539	1068
PMi092b	grey	cloudy	dodec	1.21	1373	255		28.47	-5.08	0.21	1372	1068
PMi093a	grey	cloudy	dodec	0.75	682	43		6.41	-3.11	0.22	1926	1056
PMi093b	grey	cloudy	dodec	0.75	682	43		6.41	-2.12	0.22	846	1056
PMi094a	colorless	clear	octa	1.79	463	40	22.55	0.62	-4.44	0.21	474	1072
PMi094b	colorless	clear	octa	1.79	463	40	22.55	0.62	-4.66	0.22	504	1072
PMi095a	grey	cloudy	octa	1.58	1242	186		37.13	-5.63	0.18	1334	1064
PMi095b	grey	cloudy	octa	1.58	1242	186		37.13	-5.71	0.17	1281	1064
PMi096a	grey	cloudy	irregular	1.29	1223	210		21.65	-4.89	0.21	1187	1068
PMi096b	grey	cloudy	irregular	1.29	1223	210		21.65	-4.70	0.21	1210	1068
PMi097a	colorless	clear	octa	0.77	419	20	16.59		-4.23	0.22	513	1060
PMi097b	colorless	clear	octa	0.77	419	20	16.59		-4.32	0.21	635	1060
PMi098a	colorless	clear	octa	1.62	850	126	86.63	0.87	-5.10	0.17	1027	1072

Table 3.1 Continued

Sample	Color	Clarity	Morphology	Wt (mg)	N_{FTIR} (at. ppm)	B_{FTIR} (at. ppm)	Platelet (cm^{-2})	H (cm^{-2})	$\delta^{13}C_{VPDB}$	2σ	N_{SIMS} (at. ppm spot)	Temp 3.5
PMi098b	colorless	clear	octa	1.62	850	126	86.63	0.87	-4.98	0.18	1124	1072
PMi099a	colorless	clear	octa	1.16	1625	586		25.37	-5.05	0.22	1792	1084
PMi099b	colorless	clear	octa	1.16	1625	586		25.37	-3.49	0.21	2545	1084
PMi099c	colorless	clear	octa	1.16	1625	586		25.37	-3.36	0.22	703	1084
PMi099d	colorless	clear	octa	1.16	1625	586		25.37	-3.41	0.21	1062	1084
PMi099e	colorless	clear	octa	1.16	1625	586		25.37	-3.12	0.21	766	1084
PMi100a	colorless	clear	dodec	1.65	542	0	17.54	0.93	-4.23	0.21	610	
PMi100b	colorless	clear	dodec	1.65	542	0	17.54	0.93	-4.28	0.21	627	
PMi101a	colorless	clear	agg	0.56	1545	634		112.55	-3.92	0.21	2256	1090
PMi101b	colorless	clear	agg	0.56	1545	634		112.55	-3.72	0.21	2639	1090
PMi102a	colorless	clear	agg (octa)	0.75	441	105	41.14	1.73	-5.09	0.17	544	1100
PMi102b	colorless	clear	agg (octa)	0.75	441	105	41.14	1.73	-5.38	0.18	749	1100
PMi103a	brown	cloudy	octa	0.57	583	87			-2.69	0.22	455	1081
PMi103b	brown	cloudy	octa	0.57	583	87			-2.74	0.21	447	1081
PMi104a	grey	cloudy	cube	0.68	918	371		14.41	-4.06	0.21	1843	1101
PMi104b	grey	cloudy	cube	0.68	918	371		14.41	-4.01	0.21	1874	1101
PMi105a	brown	clear	dodec	0.93	128	69	28.08	25.43	-3.47	0.24	553	1163
PMi105b	brown	clear	dodec	0.93	128	69	28.08	25.43	-3.94	0.22	229	1163
PMi105c	brown	clear	dodec	0.93	128	69	28.08	25.43	-3.90	0.21	182	1163
PMi105d	brown	clear	dodec	0.93	128	69	28.08	25.43	-3.78	0.21	647	1163
PMi106a	grey	cloudy	octa	1.40	496	13		1.97	-2.33	0.17	554	1043
PMi106b	grey	cloudy	octa	1.40	496	13		1.97	-2.37	0.17	564	1043
PMi107a	colorless/grey	clear/cloudy	octa	1.25	702	36	9.75	0.95	-3.94	0.18	687	1051
PMi107b	colorless/grey	clear/cloudy	octa	1.25	702	36	9.75	0.95	-6.24	0.17	1761	1051
PMi107c	colorless/grey	clear/cloudy	octa	1.25	702	36	9.75	0.95	-5.90	0.17	1904	1051
PMi108a	colorless	clear	dodec	1.68	1688	346	19.75	32.54	-3.89	0.17	1134	1066
PMi108b	colorless	clear	dodec	1.68	1688	346	19.75	32.54	-3.88	0.17	900	1066
PMi108c	colorless	clear	dodec	1.68	1688	346	19.75	32.54	-4.86	0.18	2442	1066
PMi109a	colorless	clear	agg (octa)	0.99	419	65	69.47	2.82	-4.11	0.17	96	1089
PMi109b	colorless	clear	agg (octa)	0.99	419	65	69.47	2.82	-4.32	0.18	135	1089
PMi110a	grey	cloudy	cube	0.77					-5.80	0.22	51	
PMi110b	grey	cloudy	cube	0.77					-4.95	0.22	53	
PMi111a	colorless	clear	agg (octa)	0.48	661	78	28.85	5.91	-4.89	0.22	1070	1072
PMi111b	colorless	clear	agg (octa)	0.48	661	78	28.85	5.91	-3.62	0.21	1171	1072
PMi111c	colorless	clear	agg (octa)	0.48	661	78	28.85	5.91	-4.80	0.21	22	1072

Table 3.1 Continued

Sample	Color	Clarity	Morphology	Wt (mg)	N_{FTIR} (at. ppm)	B_{FTIR} (at. ppm)	Platelet (cm^{-2})	H (cm^{-2})	$\delta^{13}C_{VPDB}$	2σ	N_{SIMS} (at. ppm spot)	Temp 3.5
PMi111c2	colorless	clear	agg (octa)	0.48	661	78	28.85	5.91			25	1072
PMi112a	brown	clear	dodec	1.72	776	32	14.84	48.56	-3.41	0.22	20	1044
PMi112a2	brown	clear	dodec	1.72	776	32	14.84	48.56			22	1044
PMi112b	brown	clear	dodec	1.72	776	32	14.84	48.56	-3.66	0.22	840	1044
PMi112c	brown	clear	dodec	1.72	776	32	14.84	48.56	-3.42	0.22	999	1044
PMi113a	colorless	clear	macle	2.30	392	0	10.90	0.15	-4.21	0.17	435	
PMi113b	colorless	clear	macle	2.30	392	0	10.90	0.15	-4.14	0.17	396	
PMi114a	colorless	clear	octa	1.32	902	69	82.03	2.39	-2.88	0.22	1216	1055
PMi114b	colorless	clear	octa	1.32	902	69	82.03	2.39	-4.39	0.21	1868	1055
PMi117a	brown	cloudy	dodec	1.01	887	428			-3.65	0.21	1433	1110
PMi117b	brown	cloudy	dodec	1.01	887	428			-3.38	0.22	1785	1110
PMi117c	brown	cloudy	dodec	1.01	887	428			-5.68	0.21	533	1110
PMi118a	colorless	clear	octa	0.79	832	146	101.50	0.44	-3.96	0.22	880	1077
PMi118b	colorless	clear	octa	0.79	832	146	101.50	0.44	-3.86	0.22	622	1077
PMi118c	colorless	clear	octa	0.79	832	146	101.50	0.44	-3.89	0.21	851	1077
PMi119a	grey	cloudy	cube	0.93	906	304		22.47	-5.15	0.17	1205	1095
PMi119b	grey	cloudy	cube	0.93	906	304		22.47	-3.01	0.17	1225	1095
PMi119c	grey	cloudy	cube	0.93	906	304		22.47	-3.07	0.18	1118	1095
PMi119d	grey	cloudy	cube	0.93	906	304		22.47	-3.43	0.17	1882	1095
PMi119e	grey	cloudy	cube	0.93	906	304		22.47	-3.73	0.17	1264	1095
PMi120a	brown	clear	dodec	0.83	101	58	23.63	14.33	-3.88	0.22	51	1172
PMi120b	brown	clear	dodec	0.83	101	58	23.63	14.33	-4.54	0.22	19	1172
PMi121a	grey	cloudy	irregular	0.87	1181	674		30.63	-5.57	0.22	1698	1111
PMi121b	grey	cloudy	irregular	0.87	1181	674		30.63	-5.14	0.22	1747	1111
PMi122a	brown	clear	octa	0.56	700	99	49.46	0.80	-3.99	0.17	735	1075
PMi122b	brown	clear	octa	0.56	700	99	49.46	0.80	-3.95	0.18	793	1075
PMi123a	grey	cloudy	cube	1.30	970	243		5.92	-4.55	0.18	1022	1084
PMi123b	grey	cloudy	cube	1.30	970	243		5.92	-4.83	0.18	1035	1084
PMi124a	brown	clear	dodec	1.15	1170	591	2.20	71.64	-5.67	0.17	1553	1105
PMi124b	brown	clear	dodec	1.15	1170	591	2.20	71.64	-5.27	0.18	1640	1105
PMi124c	brown	clear	dodec	1.15	1170	591	2.20	71.64	-5.32	0.17	1544	1105
PMi125a	grey	cloudy	cube	0.65					-3.01	0.18	1813	
PMi125b	grey	cloudy	cube	0.65					-3.74	0.19	1825	

Table 3.1 Continued

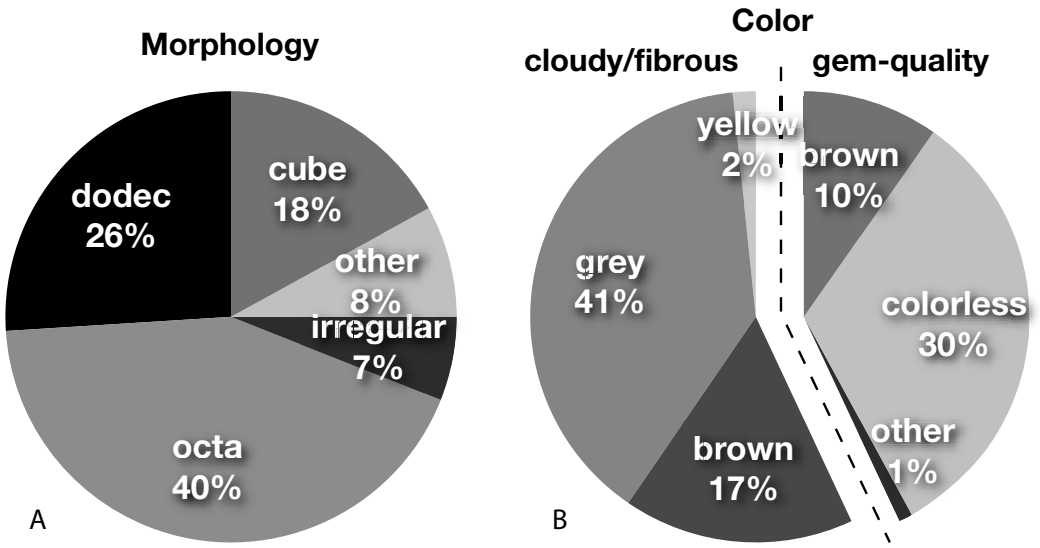

Figure 3.1. Pie charts illustrating the distribution of Panda micro-diamond physical characteristics (n=121).

Details on the morphology and color of a representative parcel of Panda macro-diamonds can be found in Table 1 of Gurney et al. (2004). Macro-diamonds of 2-3 mm size are characterized by abundant octahedra (56% of regular samples) mostly colorless but with some browns, and 13% of these octahedra have fibrous coats. The remaining population consists of 26% of opaque cubes, 14% of dodecahedra and a few percent each of twinned and aggregate diamonds. Of the total parcel of 779 diamonds, 39% are irregular: fragments with no discernible morphology. By comparison, the micro-diamonds of this study consist of smaller proportions of octahedra and cubes with much less abundant coated and irregular diamonds. Conversely, dodecahedroids are more common.

Morphology and color of macro-diamonds from Panda utilized in this study were described in detail by Tappert et al. (2005) and are listed in Table 3.2. The physical characteristics of the 90 gem-quality macro-diamonds are not representative of the overall macro-diamond population of Panda as the available parcels were preferentially sampled for clear, mineral inclusion-

Sample	Color	Clarity	Morphology	N_{FTIR} (at. ppm)	B_{FTIR} (at. ppm)	Platelet	(cm^{-2})	H (cm^{-2})	$\delta^{13}C_{VPDB}$	Temp 3.5
PA01	brown	clear	octa	176	126		69.88	12.53	-5.58	1174
PA02	brown	clear	macle	411	65		23.14	4.91	-5.22	1090
PA03	brown	clear	macle	86	19		6.21	4.72	-4.58	1137
PA04	brown	clear	macle	94	42		8.27	1.59	-4.58	1161
PA05	brown	clear	dodec	70	48		2.44	0.51	-5.81	1194
PA06	brown	clear	octa	137	76		24.17	5.53	-5.51	1162
PA07	brown	clear	octa	19	0			0.81	-5.21	
PA08	brown	clear	octa	24	11			0.74	-5.19	1198
PA09	brown	clear	octa	389	69		24.83	5.39	-5.28	1095
PA10	brown	clear	irregular	31	6		5.65	3.07	-5.65	1158
PA11	brown	clear	dodec	455	225		170.55	1.01	-5.32	1127
PA12	brown	clear	octa	175	36		23.98	2.48	-5.05	1118
PA13	brown	clear	octa	67	24		6.30	1.76	-5.07	1160
PA14	brown	clear	octa	484	88		49.03	13.96	-6.93	1090
PA15	brown	clear	octa	112	87			3.33	-14.05	1194
PA16	brown	clear	octa	116	59		11.08	10.49	-5	1162
PA17	brown	clear	dodec	46	28		1.24	1.59	-5.45	1197
PA18	brown	clear	dodec	62	30		6.75	2.96	-4.99	1176
PA19	brown	clear	octa	111	44		15.00	6.37	-5.71	1152
PA20	brown	clear	octa	184	113		59.34	5.01	-5.01	1161
PA21	brown	clear	octa	63	50		2.41	2.83	-5.5	1213
PA22	brown	clear	irregular	91	67		32.69	9.58	-4.27	1194
PA23	brown	clear	octa	473	244		161.30	4.81	-4.85	1128
PA24	colorless	clear	irregular	857	152		79.71	0.81	-3.58	1077
PA25	brown	clear	dodec	269	194		124.22	7.13	-5.73	1164
PA26	colorless	clear	dodec	62	0		2.32		-5.14	
PA27	brown	clear	irregular	199	17		6.14		-4.33	1091
PA28	brown	clear	irregular	209	58		3.68		-4.98	1123
PA29	brown	clear	irregular	299	39		12.93	0.64	-5.32	1092

Table 3.2. Macro-diamond morphology and color is from Tappert et al. (2005) and $\delta^{13}C$ is from Cartigny et al. (2009). All other data were collected in this study. Abbreviations are the same as for Table 3.1.

Sample	Color	Clarity	Morphology	N_{FTIR} (at. ppm)	B_{FTIR} (at. ppm)	Platelet	(cm^{-2})	H (cm^{-2})	$\delta^{13}C_{VPDB}$	Temp 3.5
PA30	brown	clear	irregular	123	0		1.97		-4.77	
PA31	brown	clear	irregular	189	23		5.23		-5.05	1101
PA32	brown	clear	irregular	370	36		30.33		-2.98	1080
PA33	brown	clear	irregular	380	64		22.23		-4.87	1094
PA34	brown	clear	irregular	377	97		17.46		-5.31	1107
PA35	brown	clear	irregular	151	14				-5.07	1099
PA36	brown	clear	octa	429	167		106.18	12.78	-4.73	1118
PA37	brown	clear	octa	87	47		19.46	2.76	-5.96	1173
PA38	colorless	clear	octa	295	22		44.48	3.86	-4.34	1079
PA39	brown	clear	irregular	0	0			0.90	-3.55	
PA40	brown	clear	dodec	0	0				-5.75	
PA41	brown	clear	irregular	85	36		26.46	5.72	-5.12	1161
PA42	brown	clear	macle	41	6		4.58	2.55	-4.86	1143
PA43	brown	clear	macle	303	103		64.34	7.20	-5.15	1121
PA44	brown	clear	irregular	27	0				-5.74	
PA45	brown	clear	irregular	87	44		12.06	3.52	-4.87	1169
PA46	brown	clear	irregular	161	37		23.86	8.93	-5.71	1123
PA47	colorless	clear	octa	1260	163		76.96	2.75	-4.27	1060
PA48	colorless	clear	octa	964	249		146.51	2.48	-5.03	1085
PA49	brown	clear	octa	72	42		33.06	5.67	-5.45	1182
PA50	brown	clear	irregular	0	0			1.12	-4.01	
PA51	colorless	clear	octa	545	33		30.97		-5.57	1060
PA52	brown	clear	dodec	357	91		64.12	4.65	-5.71	1108
PA53	brown	clear	irregular	0	0		1.50	0.91	-5.79	
PA54	brown	clear	irregular	402	402		5.96	0.77	-3.5	
PA55	brown	clear	octa	96	62		30.05	15.19	-5.27	1181
PA56	brown	clear	octa	843	784		432.12	126.73	-6.36	1177
PA57	colorless	clear	irregular	409	44		28.31		-4.96	1080
PA58	brown	clear	macle	196	132		16.44	11.82	-5.4	1166
PA59	brown	clear	irregular	20	19			1.42	-4.42	1291

Table 3.2 Continued

Sample	Color	Clarity	Morphology	N_{FTIR} (at. ppm)	B_{FTIR} (at. ppm)	Platelet	(cm^{-2})	H (cm^{-2})	$\delta^{13}C_{VPDB}$	Temp 3.5
PA60	colorless	clear	irregular	677	589		344.09	15.37	-6.1	1165
PA61	colorless	clear	irregular	0	0				-4.46	
PA62	brown	clear	irregular	0	0			0.97	-4.56	
PA63	brown	clear	agg	73	73		26.70	19.29	-11.21	
PA64	colorless	clear	agg (cube)	811	39			5.76	-5.1	1046
PA65	colorless	clear	macle	801	801		299.42	42.05	-19.4	
PA66	colorless	clear	macle	778	71		27.46	20.03	-9.9	1062
PA67	colorless	clear	agg	81	71			8.30	-4.59	1222
PA68	colorless	clear	agg	147	147			11.32	-5.59	
PA69	colorless	clear	agg (octa)	917	74		60.78	0.90	-5.29	1055
PA70	brown	clear	irregular	85	23		3.93	6.62	-5.07	1144
PA71	brown	clear	irregular	30	18		3.04	7.48	-8.36	1207
PA72	brown	clear	irregular	0	0				-4.46	
PA73	colorless	clear	agg (cube)	923	72			14.31	-5.45	1055
PA74	colorless	clear	agg (cube)	651	0			2.62	-4.37	
PA75	colorless	clear	octa	780	47		37.15		-4.73	1052
PA76	colorless	clear	octa	816	18		18.44		-4.91	1029
PA77	colorless	clear	octa	951	220		101.52	2.90	-3.91	1082
PA78	colorless	clear	octa	491	81		42.57	0.96	-5.12	1087
PA79	colorless	clear	irregular	473	47		33.41	0.74	-4.68	1075
PA80	colorless	clear	irregular	630	32		59.23	0.88	-4.9	1053
PA81	brown	clear	octa	61	0		4.33	1.78	-5.07	
PA82	colorless	clear	octa	236	61				-4.33	1118
PA83	brown	clear	octa	217	0		3.54		-5.37	
PA84	brown	clear	octa	712	629		407.89	8.88	-5.14	1166
PA85	brown	clear	octa	367	22		6.63		-2.98	1069
PA86	brown	clear	irregular	331	31		7.78		-4.2	1082
PA87	brown	clear	irregular	44	15		8.69	1.36	-5.21	1169
PA88	colorless	clear	irregular	510	78		41.32	0.58	-4.93	1085
PA89	colorless	clear	octa	720	93		30.08	0.69	-4.78	1072
PA90	brown	clear	irregular	72	0				-5.81	

Table 3.2 Continued

bearing diamonds (Stachel et al., 2003). As noted above, approximately 40% of our micro-diamond parcel is opaque. Thus, there is a stark contrast in physical characteristics between the present micro-diamond population (representative sample) and the available macro-diamond population (non-representative sample).

Among the diamonds described by Tappert et al. (2005), octahedral (37%) and irregular (34%) crystal shapes dominate with lesser amounts of dodecahedroids and aggregates. Also, the macro-diamonds are either brown (n= 64) or colorless (n = 26) and 49% show signs of plastic deformation (Tappert et al., 2005). Fragments of the original 90 samples from that study were reanalyzed by FTIR for this study to ensure consistent application of analytical procedures.

3.3. Methods

3.3.1. FTIR

Nitrogen concentrations (at. ppm) and aggregation states (%B=100IaB/[IaA+IaB]) and hydrogen and platelet peak areas (cm^{-2}) were measured on whole micro-diamonds and macro-diamond cleavage fragments in the De Beers Laboratory for Diamond Research at the University of Alberta, Canada (see Tables 3.1 and 3.2). Samples were cleaned with petroleum ether in an ultrasonic bath for at least 15 minutes and analyzed using a Thermo-Nicolet Nexus 470 Fourier transform infrared (FTIR) spectrometer coupled to a Continuum microscope. The instrument and the sample stage area were purged with a mixture of nitrogen and oxygen to minimize interference from the ambient air and to maintain a constant background signal. Two hundred scans were accumulated per sample and background measurements were taken every four hours. The spectral range and data

spacing were 4000 cm^{-1} to 650 cm^{-1} and 1.93 cm^{-1} (i.e. resolution of 4), respectively.

Diamond spectra were normalized to 1 cm sample thickness with an absorption coefficient of 11.92 cm^{-1} at wavenumber ~1992 cm^{-1}. Spectral deconvolution was done by a least squares method to segregate the A (nitrogen pairs), B (tetrahedron of four nitrogens surrounding a vacancy) and D (platelet related absorption at 1282 cm^{-1}) components (program provided by David Fisher, Diamond Trading Company, Maidenhead, UK). Absorption coefficient values (peak heights) for nitrogen A and B centers at 1282 cm^{-1} were converted to atomic parts per million (at. ppm) using the coefficients of 16.5 (Boyd et al., 1994) and 79.4 (Boyd et al., 1995), respectively. Detection limits range between 5 at. ppm and 15 at. ppm and spectra quality is dependent on IR transparency of the diamond.

Integration of the platelet and hydrogen peak areas (cm^{-2}) was completed using the peak area function of the Omnic software supplied by Thermo Nicolet, after local background fitting by the Omnic software to remove diamond and nitrogen related absorbance.

3.3.2. Carbon Isotope Measurements

Prior to isotopic analysis, 13 to 17 micro-diamonds were mounted in each of 8 epoxy blocks, which were then polished with 15 micron and 6 micron diamond plates, exposing randomly oriented sections through the samples. The epoxy mounts were reshaped into smaller blocks and then multiple blocks were pressed into indium pucks surrounding a centrally positioned standard, cleaned with ultra-pure ethanol and coated with 25 nm thick gold layer.

Carbon isotope ratios (reported in per mil $\delta^{13}C_{VPDB}$) and nitrogen concentrations of individual growth zones were determined using a Cameca IMS 1280 multicollector secondary ion mass spectrometer (MC-SIMS) at the Canadian Centre for Isotopic Microanalysis (CCIM) at the University of Alberta. The primary cesium ion beam had an impact energy of 20 keV and a spot size of ~15 μm diameter. Ion beam rastering to remove potential surface contamination preceded each spot analysis and spots were analyzed for a total of 100s (carbon) and 50s (nitrogen). Charge compensation with the normal incidence electron gun was not required. Carbon ($^{12}C^-$, $^{13}C^-$) secondary ions were collected by dual Faraday cups (L'2, FC2) at medium mass resolution ($\Delta m/m$ = 1850, >2600 with peak center offset) to resolve interference of $^{12}C^1H^-$ on ^{13}C. For nitrogen determinations, the secondary ions of $^{12}C^{12}C^-$ and $^{12}C^{14}N^-$ were collected simultaneously by either a Faraday-Faraday (L'2, FC2) or Faraday-electron multiplier (L'2, EM) configuration, depending on concentrations. Mass resolution for $^{12}C^{14}N^-$ was tuned to ~6900 to resolve interferences associated with $^{13}C^{13}C^-$ and $^{12}C^{13}C^1H^-$. There is no significant bias within the stated uncertainties associated with the use of FC-FC or FC-EM methods. The $^{12}C^{14}N^-/^{12}C^{12}C^-$ ratio was utilized as the proxy for relative N. Synthetic diamond reference materials S0011B and S0011C ($\delta^{13}C$ = -22.38‰, -22.78; R. Stern, unpublished data, 2012), were analyzed repeatedly during analyses of the unknowns to correct for instrumental mass fractionation (~25‰ in favor of $^{12}C^-$) and error analysis. A linear working curve (R. Stern, unpublished data, 2012) relating FTIR-determined N to $^{12}C^{14}N^-/^{12}C^{12}C^-$ in synthetic, N-zoned diamond S0011G was utilized for N calibration. Uncertainty (2σ) for $\delta^{13}C$ ranged from 0.16‰ to 0.24‰. For N, the uncertainties are estimated at ±10% of the reported value.

Macro-diamond isotopic compositions were previously determined at the Laboratoire de Géochimie des Isotopes Stables at l'Institut de Physique du Globe, Paris by Cartigny et al. (2009) using a conventional dual-inlet mass spectrometer. Procedures follow those described by Cartigny et al, (2004) and analytical uncertainty is reported to be < 0.1‰. This laboratory is where the synthetic reference material used at CCIM for diamond analyses was established, thereby ensuring comparability between the micro- and macro-diamond $\delta^{13}C$ data sets.

3.3.3. Cathodoluminescence (CL) imaging

CL imaging was conducted at CCIM using a Zeiss EVO MA 15 scanning electron micro-scope equipped with color (Gatan ChromaCL) and wide spectrum (ETP Semra Proprietary Ltd.) CL detectors. Analytical conditions were typically 15 kV and 3 nA to 5 nA beam current. Samples were coated with 5 nm Au, and imaged prior to SIMS analysis.

3.3.4. Statistical methods

The quantitative statistical comparison of gem-quality micro- and macro-diamond data involves two-tailed student's t-test and two-sample f-test for variances. The first test compares the means of two populations for significant differences and the second the variances of two independent populations. The tests assume both populations are normally distributed, but are still valid for non-normally distributed populations if they are large ($n > 40$; Moore, 2000) . The results can be compared to critical values depending on degrees of freedom and chosen confidence level (here 98% for all tests) to establish whether to reject or accept the null hypothesis. In every case in this study, the null hypothesis is that both populations being tested are the same and although some of the populations tested herein are not normally distributed, they are large and so these tests are still robust.

3.4. Results

3.4.1. Nitrogen concentrations and aggregation states

Nitrogen concentrations determined by FTIR (100 μm spot size) is similar to a bulk analysis in that the FTIR signal is integrated over the entire sample thickness. Because of a penetration depth of <1 μm, a SIMS ion beam (15 μm spot size) only probes the sample surface. In consequence, comparison of the nitrogen in the datasets presented here may be expected to show some differences.

Within the micro-diamonds, 102 diamonds were analyzed by FTIR and the remaining 19 samples were either too heavily included to transmit a detectable IR signal or yielded only poor spectra. Nitrogen contents range from detection limit (Type II < 10 at. ppm) to 1696 at. ppm with a median at 805 at. ppm (Table 3.1).

Of the 49 gem-quality (fully transparent) micro-diamonds, two are Type II (N < 10 at. ppm) and two had unreliable spectra, the remainder having a nitrogen concentration between 51at. ppm and 1688 at. ppm. Including the Type II samples, gem-quality micro-diamonds have a median of 631 at. ppm nitrogen. For the whole of this subpopulation aggregation states range from 0% to 97% and are skewed towards < 30%B (median = 18%). The 55 cloudy micro-diamonds measured by FTIR range in nitrogen from 366 at. ppm to 1696 at. ppm with a median of 966 at. ppm and are aggregated from 0% to 59%B with a normal distribution (median = 25%B). Based on previous studies, on average, greater nitrogen concentrations have been observed in cloudy/fibrous diamonds compared to gem-quality diamonds (Boyd et al., 1987; Hauri et al., 1999; Araujo et al., 2009; Howell et al., 2012).

The 90 gem-quality macro-diamonds re-examined for this study also provide additional information. Nitrogen values range from below detection (Type II (n = 4)) to 1260 at. ppm with a median at 187 at. ppm. Nitrogen aggregation states in macro-diamonds range from 0% to 100%B, but again are also strongly skewed towards < 30%B with a median at 26%B.

Nitrogen contents measured by SIMS were obtained on polished diamond surfaces, within individual growth zones exceeding 20 μm in width. The growth zones were observed by cathodoluminescence imaging, two examples being given in Figure 3.2. Samples with reasonably homogeneous luminescence patterns were typically probed in two spots to test intra-grain consistency. Samples with complex zonation were probed in up to seven locations to explore variations in nitrogen content between distinct zones (see Table 3.1).

All 121 micro-diamond samples were analyzed and “spot” concentrations range from 0.2 at. ppm to 2639 at. ppm with a median of 907 at. ppm. This is a much larger range and higher median than the “bulk” FTIR results (<10 at. ppm to 1696 at. ppm and 805 at. ppm, respectively). Bulk and individual spot measurements from the same samples differ by up to 1244 at. ppm and the median difference is 210 at. ppm, with higher concentrations in spot analyses (Figure 3.3). Similar differences between FTIR and SIMS data have previously been observed in Diavik samples (Klein-BenDavid et al., 2007). This difference likely relates to the fact that typically during polishing only a limited number of growth layers close to the crystal edge were exposed.

Individual growth zones within samples that display highly contrasting luminescence can have extremely divergent nitrogen concentrations. Intra-

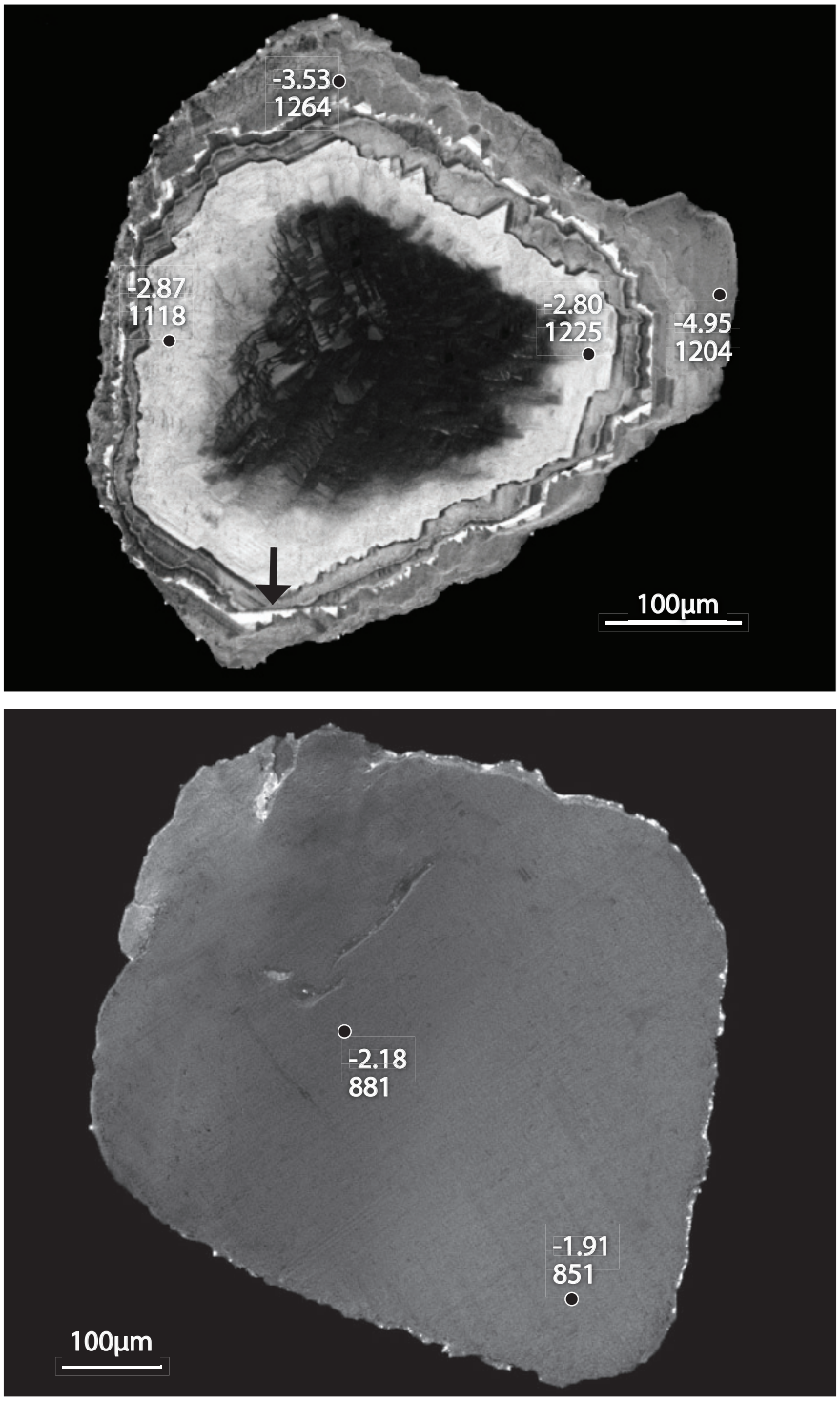

Figure 3.2. Cathodoluminescence images of PMi119 (above) and PMi071 (below). Both are sectioned in a random direction. PMi119 displays concentric growth zones while PMi071 luminesces homogeneously. $\delta^{13}C$ and N values (top and bottom numbers, respectively) from SIMS analyses are labeled. Note growth layer truncation in the bottom corner (see black arrow) of sample PMi119.

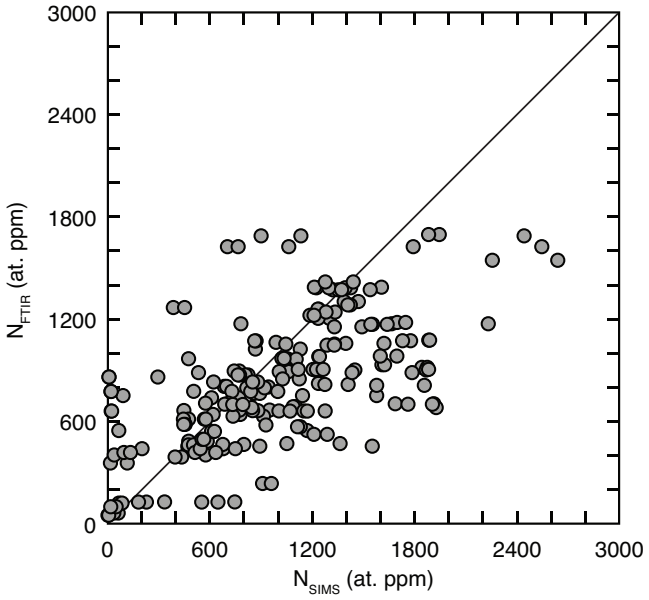

Figure 3.3. Nitrogen concentrations determined by FTIR (N_{FTIR}) and SIMS (N_{SIMS}) on the same Panda micro-diamonds.

sample variations reach up to 1842 at. ppm, but 65% of the samples vary by 164 at. ppm or less. Luminescence colors are dominantly blue with very minor yellow to yellow-green in discrete growth zones. No relationship between the intensity or color of luminescence and nitrogen content or aggregation state is apparent. High nitrogen growth zones (> 1000 at. ppm) occur as both bright and dark regions in CL imaging.

3.4.2. Platelet and hydrogen peaks

Platelets are an assemblage of interstitial carbon atoms, related to the creation of vacancies during the aggregation of nitrogen from A- to B-centers, that form extended two dimensional defects in the diamond lattice (Woods, 1986; Kiflawi et al., 1998; Goss et al., 2003). The stretching vibration of carbon-carbon bonds in the interstitial sites produces a measurable IR absorption band in the 1370 cm^{-1} region (Sobolev et al., 1968). The position of this peak, known as B', can shift from 1358 cm^{-1} to 1372 cm^{-1} likely relating to platelet size (Hanley et al.,

1977; Mendelssohn and Milledge, 1995) and the peak symmetry can change depending on bulk nitrogen concentration (Woods, 1986).

Platelet peaks in micro-diamonds were observed in 40 of the 49 gem-quality samples and in only five of the 72 cloudy diamonds. Peak areas in the gem-quality samples range from 2.2 cm^{-2} to 348 cm^{-2} and values are strongly skewed to smaller numbers (median = 38.2 cm^{-2}). Platelet peaks in the cloudy micro-diamonds appear in only five samples and are variable: 0.7 cm^{-2} up to 101 cm^{-2} (see Table 3.1). Platelet peaks in the macro-diamonds occur in similar proportions as in the gem-quality micro-diamonds (in 71 of 90 samples) with a range and median of 1.2 cm^{-2} to 432 cm^{-2} and 24.2 cm^{-2}, respectively (Table 3.2).

Hydrogen impurities in diamond result in IR absorption at various wave numbers, but are most readily observed at 3107 cm^{-1}. This sharp absorption band is attributed to vibration stretching in the vinylidene group ($C{=}CH_2$, Woods and Collins, 1983). A hydrogen peak at 3107 cm^{-1} was observed and measured in 45 (92%) of the gem micro-diamonds and 49 (68%) of the cloudy micro-diamonds. Peak areas range from < 1 cm^{-2} to 113 cm^{-2} in the gem-quality micro-diamonds and the distribution is strongly skewed (median = 2.8 cm^{-2}). Hydrogen peak areas in cloudy micro-diamonds range from < 1 cm^{-2} to 42.9 cm^{-2} and are normally distributed (median = 17.1 cm^{-2}). The macro-diamond range (< 1 cm^{-2} to 127 cm^{-2}) is similar to the gem-quality micro-diamond population. Hydrogen peaks were observed in 68 macro-diamonds (76%) and were also strongly skewed to lower numbers (median = 3.4 cm^{-2}), (see Tables 3.1 and 3.2).

Several additional peaks were observed in the FTIR spectra indicating the presence of water (1630 cm^{-1}, 3420 cm^{-1}), carbonate (1430 cm^{-1}, 876 cm^{-1}) and silicate inclusions (1080 cm^{-1} to 876 cm^{-1}) in many of the micro-

diamond samples (Navon et al., 1988; Izraeli et al., 2004). Absorption from these inclusions is particularly common in the cloudy samples (see Appendix A). Inasmuch as the focus of this paper is on the nitrogen data derived from FTIR analysis, these ancillary inclusions will not be further discussed.

3.4.3. Carbon isotopes

All 121 micro-diamonds were spot analyzed for their carbon isotope compositions. The number of analyses per sample is identical to SIMS nitrogen measurements discussed in Section 4.1 (see Table 3.1). The range in carbon isotope compositions varied between -6.9 and +1.8‰ with a normal distribution and a median of -4.2‰ (see Figure 3.4). The median is isotopically slightly heavier than the typically assumed mantle value of -5‰ (Deines, 1980). For both the gem and cloudy subdivisions, isotopic variation between growth zones is less than 0.5‰ in 88 of the 121 samples, but is more than 2‰ in six samples. Isotope compositions do not correlate with nitrogen concentrations or aggregation states. One hundred sixteen analyses on 49 gem-quality samples have a median $\delta^{13}C$ of -4.4‰ and the 72 cloudy micro-diamonds (153 analyses) have a similar median of -4.2‰. Both gem-quality and cloudy samples have identical averages: -4.2‰. Compared to micro-diamonds, macro-diamonds cover a larger range (-19.4‰ to -3.0‰) and have a slightly lower average (-5.4‰) and median (-5.1‰; Cartigny et al., 2009).

3.5. Discussion

3.5.1. Central Slave diamonds

Diamond studies from the Central Slave Craton (DO-27, Ekati and Diavik properties) have focused on mineral inclusion work that is integral to the investigation of cratonic diamond formation (Chinn et al., 1998; Davies et

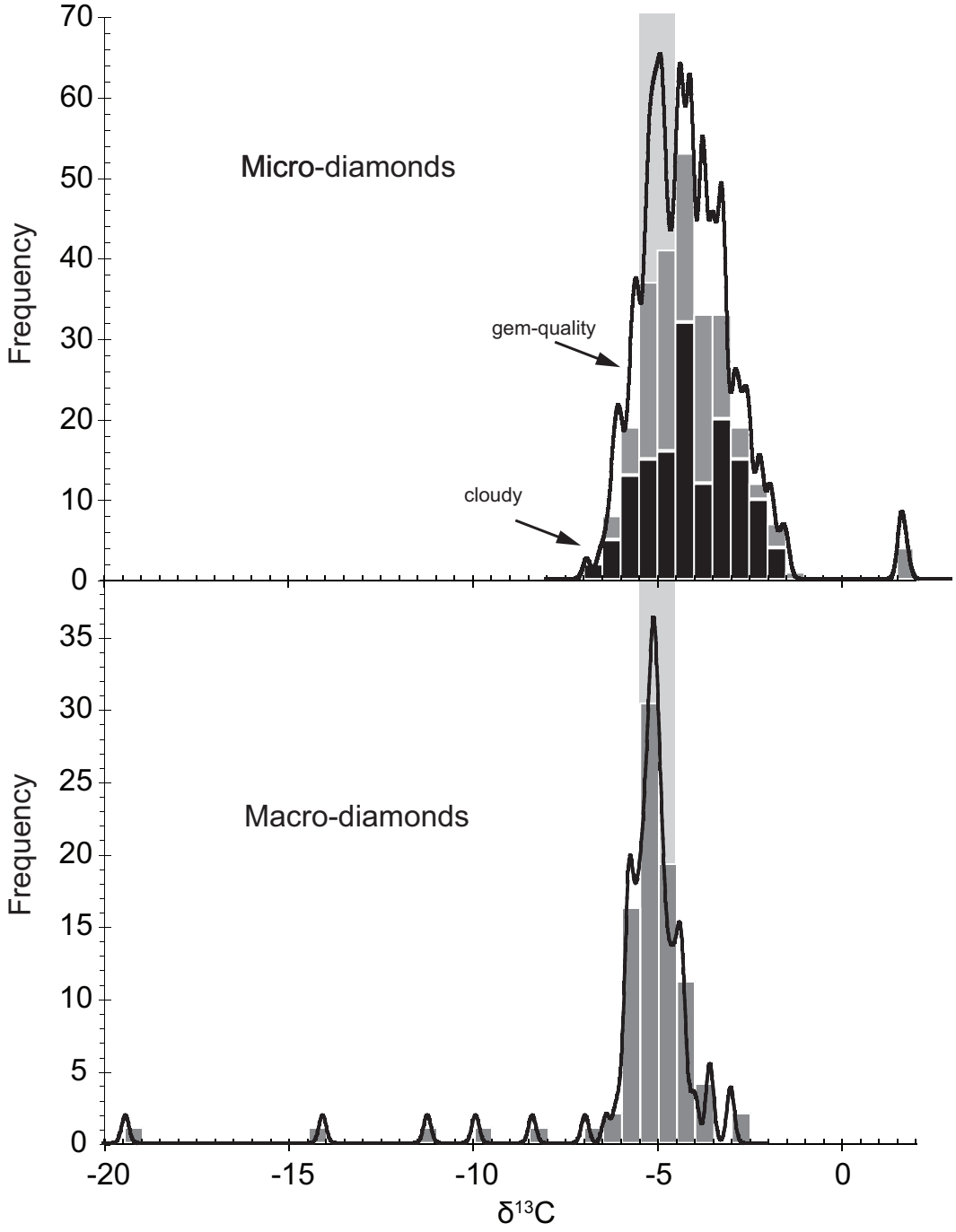

Figure 3.4. Carbon isotopic composition of Panda micro- and macro-diamonds shown as histograms (bars) and probability density curves (black line). Probability curves are calculated using a 2σ of 0.2‰. Dark and medium colored bars in the micro-diamond histogram represent cloudy and clear samples, respectively. The light grey vertical bar represents the interquartile range (values between the first and third quartile) of the macro-diamond data.

al., 1999; Stachel et al., 2003; Davies et al., 2004; Tappert et al., 2005; Klein-BenDavid et al., 2007; Creighton et al., 2007; Donnelly et al., 2007; Araujo et al., 2009; Aulbach et al., 2009; Van Rythoven and Schulze, 2009). Based on these studies $\delta^{13}C$ values of all Central Slave diamonds range from -35.8‰ to +0.7‰ with the average carbon isotope value of -6.2‰. As the $\delta^{13}C$ distribution is skewed to lower values, the median is -5.1‰ (see Figure 3.5).

Figure 3.5 also shows that the Panda micro-diamonds studied here have carbon isotope compositions that are, on average, more ^{13}C-enriched than not only Panda macro-diamonds, but also all other diamonds from Lac De Gras, regardless of size. Previous studies (see above) also show that diamond paragenesis at Panda (Ekati) and Diavik is largely peridotitic while that of DO-27 is predominantly eclogitic. Linking this evidence to Figure 3.5 confirms that the strongly $\delta^{13}C$ depleted compositions (< -10‰) almost exclusively relate to eclogitic micro-diamonds from pipe DO-27. If the “unusual” diamonds from DO-27 are excluded from the present analysis, the bulk of Lac De Gras diamonds fall between -8‰ and -4‰. When the Panda micro-diamonds are considered, this main range is extended up to +2‰ (see Figure 3.5).

The eight inclusion-bearing eclogitic macro-diamonds from Panda (Cartigny et al., 2009) have a $\delta^{13}C$ range of -19.4‰ to -4.4‰ (see Table 3.2) and half of those samples are more ^{13}C-depleted than the most depleted micro-diamond ($\delta^{13}C$ = -6.9‰). Thus, the absence of strongly ^{13}C-depleted (< -10‰) samples in the micro-diamond population may suggest the absence of an eclogitic suite within this group.

Figure 3.5 also outlines both the highly variable nitrogen concentrations in diamonds from the Central Slave Craton and the overlap with the

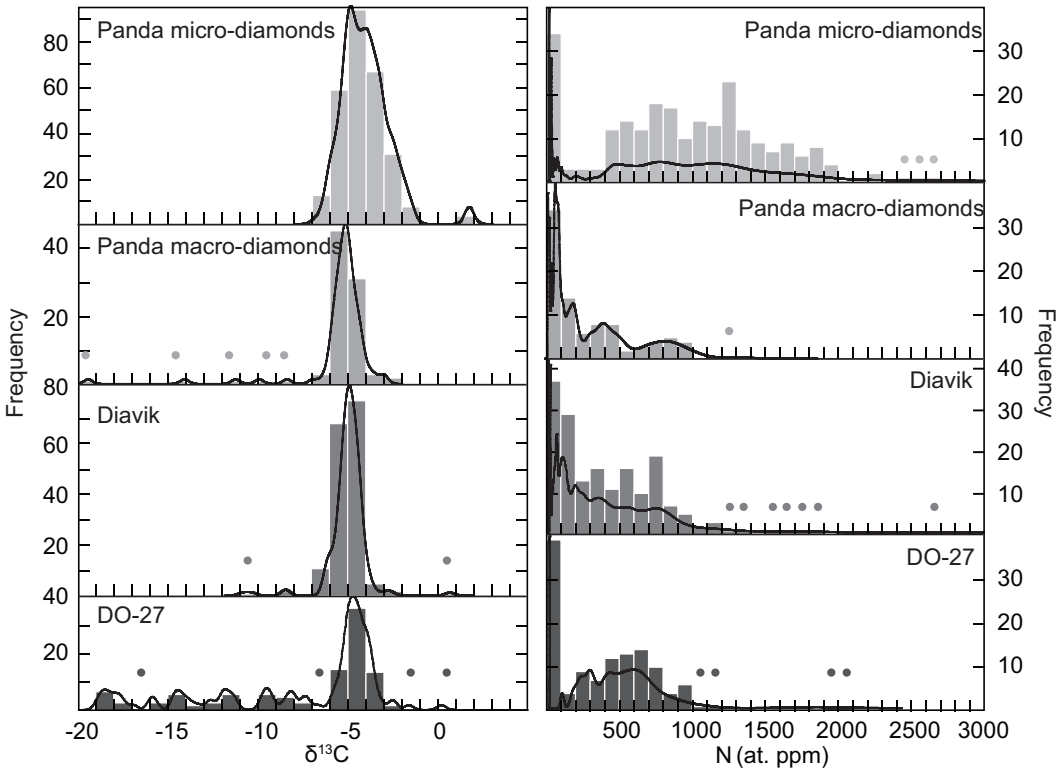

Figure 3.5. Histograms showing the nitrogen (at. ppm) concentration and carbon isotope composition (‰ $\delta^{13}C$) of diamonds from Panda, Diavik and DO-27. Panda micro-diamond nitrogen data were determined by SIMS and all others were measured by FTIR. Dots denote bars that are too small to identify because of scale and black lines are probability density curves. Black lines are probability curves calculated with a 2σ of 0.2‰ for $\delta^{13}C$ and 20% for N.

new micro-diamond measurements for Panda. Despite this overlap, a greater proportion of these micro-diamonds have N_{FTIR} concentrations above 1000 at. ppm (24%) versus all other Lac De Gras samples (5%). This observation is considered to be principally due to the inclusion of clouded and coated samples, which are not present in other studies, into the Panda micro-diamond data set. Aggregation states in micro- and macro-diamonds from Panda range from 0 to 100%B and have a median at 23%B. Diamonds from Diavik and DO-27 are overall much less aggregated with a median value of 9%B. This difference is most likely a consequence of broadly lower source nitrogen concentrations at DO-27

and Diavik although there are similar mantle residence temperatures for Diavik and Panda.

3.5.2. Panda diamond characteristics

3.5.2.1. Platelets

Woods (1986) recognized a linear correlation between platelet peak area and the absorption coefficient (peak height) related to B-centers (i.e., B-center concentration). Samples that do not fall along this correlation line are considered “irregular” (Woods, 1986) and indicate platelet degradation, most likely as a result of transient heating (Evans et al. 1995) or strain (Woods, 1986). As Figure 3.6 shows, the majority of Panda micro- and macro-diamonds are “regular” and fall close to or along the expected linear correlation between I(B’) and B-center concentration. Excluding samples that are completely aggregated (100%B), all the macro-diamond and all but six of the micro-diamond samples are “regular” and show no evidence of platelet degradation.

These six “irregular” micro-diamonds have either octahedral, dodecahedral or irregular morphologies and all of them are non-cloudy. As previously noted, the degraded samples probably reflect a local heating or straining event that has not affected the other samples. However, if these samples contained cuboid growth sectors a linear relationship between I(B’) and N_B would not be expected (Howell et al., 2012). Thus regular platelet development for the vast majority of micro- and macro-diamonds document similarly undisturbed thermal residence histories in the Central Slave subcratonic lithospheric mantle.

3.5.2.2. Nitrogen thermometry

If the age of a population of diamonds can be determined independently, additional information about their thermal residence histories can be

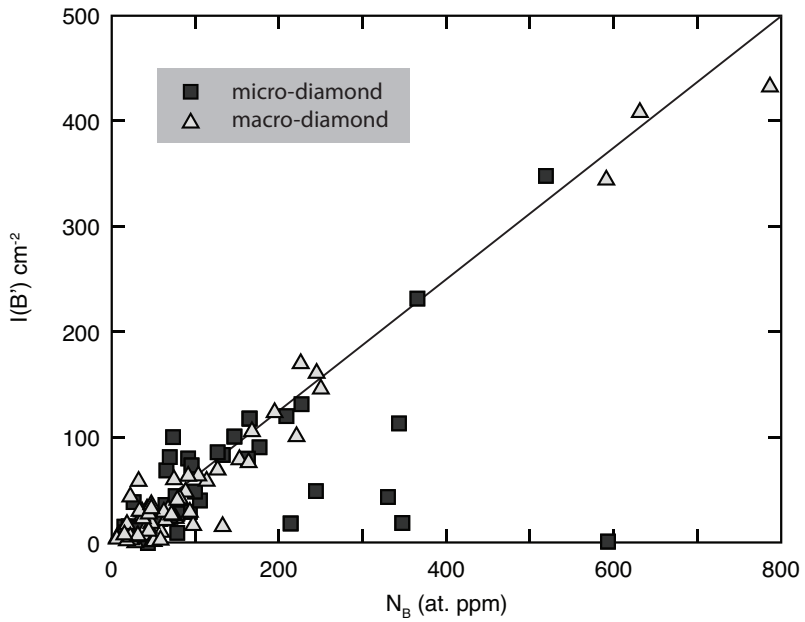

Figure 3.6. Platelet peak area (I(B'), cm^{-2}) versus the concentration of N_{FTIR} in B centers (at. ppm) for micro-diamonds (squares) and macro-diamonds (triangles). Line represents "normal" linear relationship between these two variables (from Johnson et al., 2012).

gained from their nitrogen contents and aggregation characteristics (Evans and Harris, 1989; Leahy and Taylor, 1997; Taylor et al., 1990). Panda diamonds with peridotitic sulfide inclusions give a Re-Os isotope age of 3.52 ± 0.17 Ga (Westerlund et al., 2006). Assuming the diamonds from the present study are peridotitic (see above) and share a single age of formation, time averaged mantle residence temperatures, based on nitrogen thermometry, range from 990ºC to 1290ºC (Figure 3.7).

The control of mantle residence time on temperature estimates, however, is minor, as the temperatures calculated for these diamonds at 1.5 Ga versus 3.5 Ga differ by only about 20ºC. Uncertainties associated with this nitrogen thermometer are assumed to be comparable to conventional silicate thermometry (± 50ºC, Taylor et al., 1990). Plastic deformation, observed in 5 micro-and 44 macro-diamonds, has been suggested to enhance nitrogen diffusion, thus effecting aggregation kinetics (Evans,

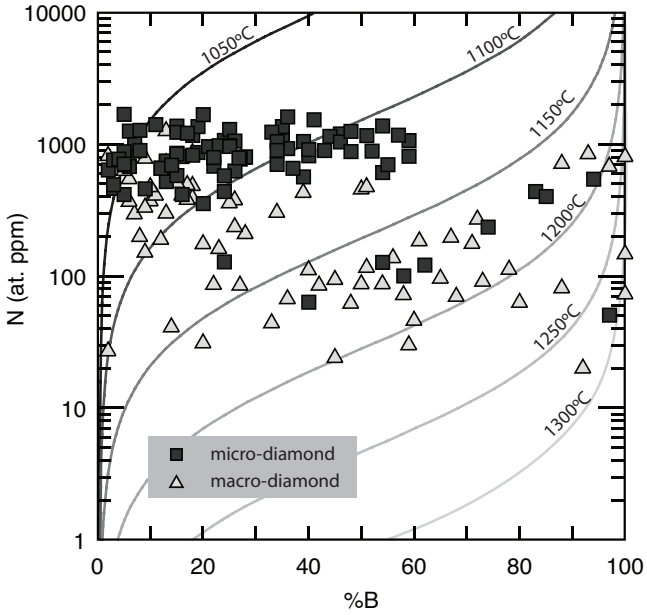

Figure 3.7. Nitrogen concentrations versus nitrogen aggregation states for Panda diamonds. Time averaged mantle residence temperature contours are shown for a 3.5 Ga mantle residence period (calculated after Leahy and Taylor, 1997).

1992). The effect of plastic deformation on nitrogen aggregation may, however, not be consistent (Shiryaev et al., 2007). Nevertheless, enhancing nitrogen aggregation by 20% would be equivalent to increasing mantle residence temperatures by < 50ºC, even in highly aggregated samples, which is within error.

As seen from Figure 3.7, the majority of the micro-diamonds cluster between about 1030ºC to 1130ºC with < 60%B and moderate to high N_{FTIR} concentrations and a second abundance maximum at 1160ºC to 1180ºC between 40%B and 100%B and N < 550 at. ppm. Macro-diamonds show an approximately bimodal temperature distribution with a first broad cluster between 1050ºC and 1150ºC, ≤ 50%B and at N > 100 at. ppm. A second cluster lies between 1160ºC and 1250ºC between 25%B and 100%B at N < 1000 at. ppm.

Re-plotting the data as a function of temperature only (Figure 3.8), more clearly identifies two distinct diamond subpopulations; a group below 1130ºC and a second group at temperatures ≥ 1160ºC. Both micro- and macro-diamonds show this temperature distribution, including the gap between the two groups, suggesting similar thermal mantle residence histories and depths of origin.

One explanation for the bimodal spread in nitrogen temperatures is that the diamonds could have variable formation ages. For example, a difference in formation ages of about 1.6 Ga between eclogitic (~1.9 Ga) and peridotitic (~2.5 Ga) diamonds is observed in the nearby A154 (Diavik) kimberlite (Aulbach et al., 2009). However, all samples are at least Paleoproterozoic. As discussed above, the control of mantle residence time on time averaged residence temperatures is minor, as long as the diamonds are generally old (>1 Ga); Paleoarchean to Paleoproterozoic diamond formation, thus, cannot generate the observed spread in $T_{Nitrogen}$.

The spread in average residence temperatures for Panda diamonds is most likely a result of diamond residence at variable depths within the cratonic mantle. Assuming a 38 mW/m^2 geotherm (Pearson et al., 1999; Menzies et al., 2004) this means a distinct depth interval below the Central Slave Craton, between ~155 km and ~165 km that either is characterized by a paucity of diamonds or was not sampled by the Panda kimberlite (Figure 3.8). However, the latter possibility is considered to be unlikely, as indicator mineral thermometry shows continuous sampling throughout the lithospheric mantle below the Central Slave Craton (Menzies et al., 2004). Rather, conditions may have been unfavorable for diamond formation or storage over a ~10 km thick region.

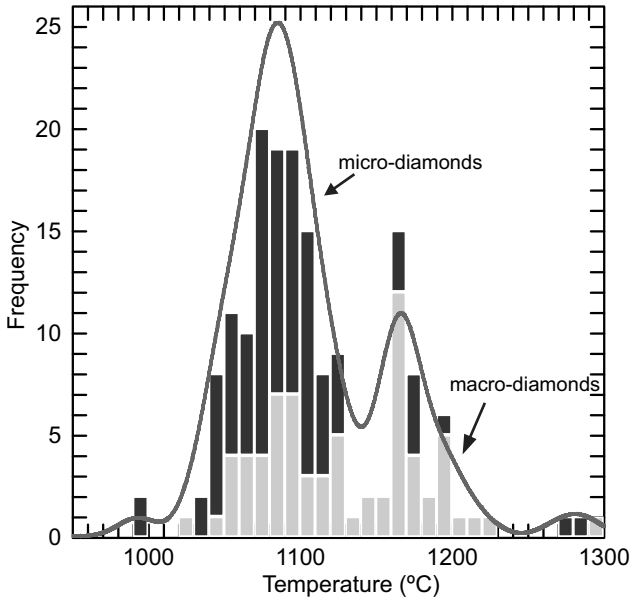

Figure 3.8. Histogram of nitrogen-based temperatures estimated for micro-diamonds (dark bars) and macro-diamonds (light bars) illustrating a significant decrease in sample density between 1130ºC and 1160ºC. Black line is a probability density curve calculated with a 2σ of 25ºC.

Lithospheric layering has been observed for the Central Slave Craton and indicates at least a two stage history (Griffin et al., 1999). The shallower, cooler lithosphere from ~100 km to 150 km depth is dominated by ultra depleted garnet harzburgite with rare lherzolite (Griffin et al., 1999; Menzies et al., 2004). The deeper layer is less depleted and dominated by garnet lherzolite and extends to ~ 200 km. It is therefore possible that the residence temperatures of the two groups reflect the upper and lower layers of the Central Slave subcratonic lithospheric mantle. At the ~150 km transition between these two layers, Griffin et al. (1999) observed an absence of Cr-pyrope garnet xenocrysts, and a distinct spike in Mg-chromite abundance in some Lac de Gras kimberlites. Malkovets et al. (2007) showed for kimberlites in the Dalldyn-Alakit Province (Yakutia) that high Mg-chromite/garnet ratios in the deep lithospheric mantle are commonly indicative of poor diamond grades. Griffin et al. (1999) estimated the garnet-poor region at ~150 km depth to be ~10 km thick,

which exactly corresponds with the depth and thickness of the diamond-poor region observed from the nitrogen thermometry of Panda diamonds.

3.5.3. Micro- and macro-diamond relationship

McCandless et al. (1994) proposed a genetic commonality between micro- and macro-diamonds, but other works suggest a genetic disconnect based on differences in morphology, inclusion chemistry and N and $\delta^{13}C$ compositions (Haggerty, 1986; Pattison and Levinson, 1995; Davies et al., 2004; Sobolev et al., 2004; Johnson et al., 2012). To investigate this relationship for the micro- and macro-diamond populations at Panda,

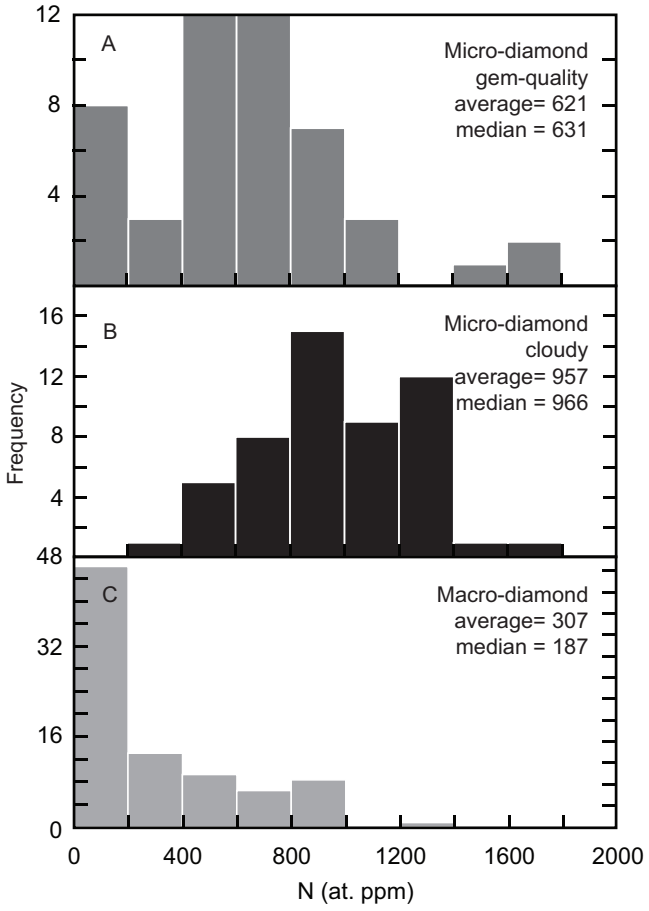

Figure 3.9. Histograms of nitrogen concentrations (as determined by FTIR) for (A) cloudy micro-diamonds, (B) clear micro-diamonds and (C) clear macro-diamonds. Cloudy micro-diamonds have significantly higher average and median N than gem-quality micro- and macro-diamonds.

statistical comparisons of the FTIR generated nitrogen concentrations and the SIMS generated carbon isotopic compositions have been completed.

As previously noted, a strong disparity in nitrogen concentrations between micro- (median = 805 at. ppm) and macro-diamonds (median = 187 at. ppm) is observed in the Panda data. Figure 3.9 illustrates the contrasting nitrogen concentration distributions of gem-type clear (Figure 3.9a) and cloudy micro-diamonds (Figure 3.9b) with that of macro-diamonds (Figure 3.9c). Gem quality micro-diamonds have lower average and median nitrogen contents than their cloudy counterparts. If those cloudy micro-diamonds are excluded from the micro-diamond population, a clear distinction between the micro- and macro-diamonds is still observed: t- and f-tests with 73 and 46 degrees of freedom, respectively, have probabilities less than 0.02 ($t(73) = 4.77$, $p < 0.02$; $f(46) = 1.80$, $p < 0.02$) for the null hypothesis (micro- and macro-diamond populations are the same) to be accepted.

Looking just at the clear micro-diamonds, Type II (N-free) diamonds have a lower abundance (4%) than among macro-diamonds (8%). Including cloudy micro-diamonds lowers the Type II abundance to 2% as none of the cloudy diamonds are Type II. This observation is in stark contrast to micro- and macro-diamonds, for example, from the Artemisia kimberlite, Northern Slave Craton (Johnson et al., 2012). There, Type II micro-diamonds are much more abundant than Type II macro-diamonds (68% versus 21%, respectively).

The carbon isotopic compositions of the gem-quality micro-diamond (-4.1‰) and macro-diamond (-5.4‰) populations from Panda are statistically distinct ($t(148) = 5.02$, $p < 0.02$; $f(89) = 0.45$, $p < 0.02$). Both populations have a near-normal distribution and exclusion of the top

and bottom 2.5% of the data gives the same statistical results. A similar result, micro-diamonds having a significantly higher average $\delta^{13}C$ values over macro-diamonds, was observed for diamonds from the Artemisia kimberlite (Johnson et al., 2012).

Because I am comparing only gem-quality micro- and macro-diamonds, the effect of sample bias should be largely eliminated. Hence, the 1.3‰ difference in average $\delta^{13}C$ between gem micro- and macro-diamonds is most likely a consequence of different growth histories.

To test the potential of isotopic subpopulations, specifically in the smaller size classes, I divided the micro-diamonds into groups of 0.25 mg, starting at a weight of 0.5 mg (Figure 3.10). Isotopic compositions in

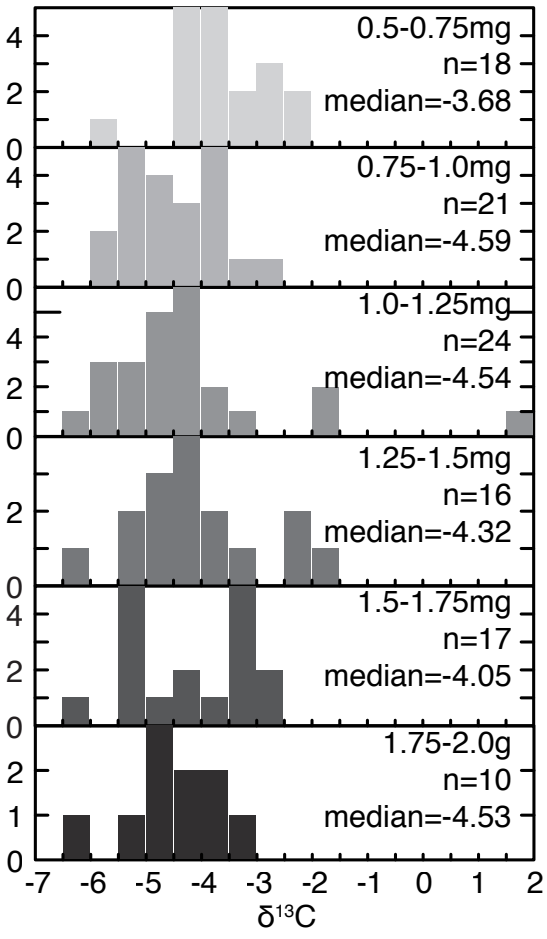

Figure 3.10. Micro-diamond carbon isotope values divided into weight increments of 0.25mg from 0.5 mg to 2.0 mg.

these weight fractions do not show any systematic bimodal (or otherwise) distribution. In addition to this, no systematic change in median isotopic values correlating with weight classes is observed. The results of this test, however, should be viewed with some caution as each weight class has between 10 and 24 samples. This low number of samples may not be sufficient to reliably represent each weight fraction and additional data is needed make more robust observations. A similar weight-based test on the macro-diamonds was not possible as their original sample weights were not recorded.

3.5.4. Carbon Isotope Evolution

Variations in carbon isotope values among growth zones of single micro-diamond samples from Panda are complex and similar observations were made on macro-diamonds from other localities (Boyd et al., 1987; Fitzsimons et al., 1999; Harte et al., 1999; Bulanova et al., 2002; Hauri et al., 2002; Klein-BenDavid et al., 2004; Schulze et al., 2004; Zedgenizov et al., 2006; Smart et al., 2011). In the present data, a few samples have $\delta^{13}C$ values (see Figure 3.2, for example) with more than ±2‰ variation from core to rim. This amount of variation can be modeled through Rayleigh fractionation of a single evolving fluid/melt (Stachel et al., 2009, Smart et al. 2011). Such a shift between growth zones would require 75% or 85% crystallization of a carbonate melt or methane-bearing fluid, respectively. Distinct growth layering with evidence for intermittent stages of resorption and non-systematic variations in N-content and $\delta^{13}C$ indicate that diamond precipitation has involved discrete pulses of fluids/melts with different isotopic signatures which may or may not have evolved through fractionation processes.

The carbon isotope data also show a qualitative trend to ^{13}C-enriched values with decreasing mantle residence temperature for both micro-

and macro-diamonds (Figure 3.11). Diamonds with mantle residence temperatures below 1130ºC have an average $\delta^{13}C$ value (-4.3‰) that is discernibly higher than the -5.0‰ average for the group of diamonds at T > 1160ºC. ($t(56) = 4.04$, $p < 0.02$). The five samples that fall between 1130ºC and 1160ºC in $T_{Nitrogen}$ are excluded from these averages (see Tables 3.1 and 3.2). Further, to eliminate outliers, the top and bottom 2.5% of the data have been excluded for each group, a procedure which did not change the 2 sigma around the averages. Thus, although overlap exists, an overall increase in $\delta^{13}C$ with decreasing residence temperature is, therefore, evident.

Taking $T_{Nitrogen}$ as an indication of residence depth, the above relationship may be attributed to two models. The first is that diamonds in the shallow harzburgitic and the deep lherzolitic layer in the lithospheric mantle

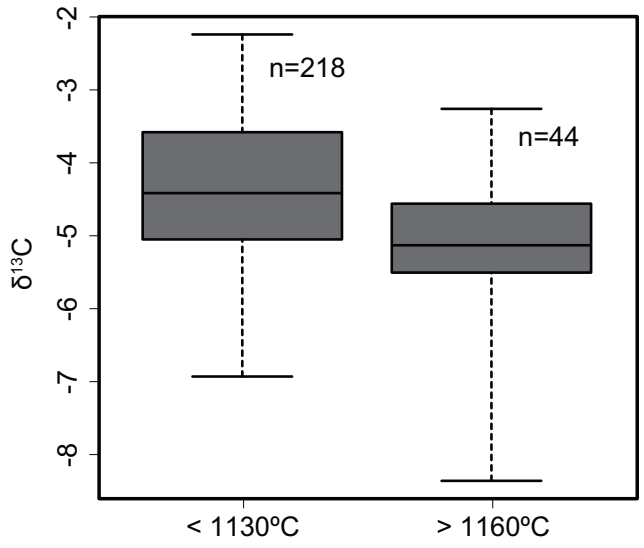

Figure 3.11. Box and whisker plot graphically displaying the spread (ends of dashed lines), first and third quartiles ("interquartile," top and bottom of boxes), and medians (line through the middle of the boxes) of the low and high temperature groups (see text). N = number of samples represented by each box and whisker. Each $\delta^{13}C$ value is treated as a single sample.

beneath Lac de Gras reflect distinct diamond-forming events with unique geochemical signatures.

The second and preferred model is continuous fractionation of diamond precipitating fluids/melts as they percolate upwards through the deeper lherzolitic and shallower harzburgitic layers in the mantle. An evolution to heavier isotope values can be explained through reduction of an oxidized C-O-H fluid or melt (Richet et al., 1977; Deines, 1980; Stachel et al., 2009). Supporting evidence comes from fO_2 studies on garnet peridotite xenoliths from Diavik, approximately 30 km southeast of Panda (Creighton et al., 2010) that identified a metasomatic event that mildly oxidized the lithospheric mantle beneath the Central Slave Craton. A reduction of the CO_3^{-2} component of upward percolating fluids/melts by the depleted and reduced lithospheric mantle would result in the precipitation of diamond and, consequently, a gradual ^{13}C enrichment in the fluid/melt.

3.6. Conclusions

Micro-diamonds from the Panda kimberlite show higher proportions of high nitrogen concentrations (>1000 at. ppm) and higher $\delta^{13}C$ values than diamonds from the other Central Slave Craton deposits of DO-27 and Diavik. Both macro- and micro-diamonds from Panda show little to no platelet degradation and indicate a broadly similar mantle residence history. Time averaged mantle residence temperatures for both macro- and micro-diamonds display bimodal distributions that indicate derivation from the depleted upper and less-depleted lower portions of the subcratonic lithospheric mantle below the Central Slave province, with the presence of a diamond-poor zone in between.

Gem quality (fully transparent) micro- and macro-diamonds show a disparity in carbon isotopic compositions that may indicate either differences in fractionation processes or growth histories.

A broad shift for Panda diamonds from lower to higher $\delta^{13}C$ values with decreasing residence temperature suggests that as the diamond-forming fluids/melts percolated up through the mantle, their isotopic signatures evolved to more ^{13}C-enriched compositions. The direction of this evolution (higher $\delta^{13}C$) is consistent with interaction between an oxidized carbonate-bearing fluid and a reduced lithosphere.

References

Araújo, D.P., Griffin, W.L., O'Reilly, S.Y., Grant, K.J., Ireland, T., Holden, P., van Achterbergh, E., 2009. Microinclusions in monocrystalline octahedral diamonds and coated diamonds from Diavik, Slave Craton: Clues to diamond genesis. Lithos 112, 724–735.

Aulbach, S., Stachel, T., Creaser, R.A., Heaman, L.M., Shirey, S.B., Muehlenbachs, K., Eichenberg, D., Harris, J.W., 2009. Sulphide survival and diamond genesis during formation and evolution of Archaean subcontinental lithosphere: A comparison between the Slave and Kaapvaal cratons. Lithos 112, Supplement 2, 747–757.

Boyd, S.R., Kiflawi, I., Woods, G.S., 1994. The relationship between infrared absorption and the A defect concentration in diamond. Philosophical Magazine Part B 69, 1149–1153.

Boyd, S.R., Kiflawi, I., Woods, G.S., 1995. Infrared absorption by the B nitrogen aggregate in diamond. Philosophical Magazine Part B 72, 351–361.

Boyd, S.R., Mattey, D.P., Pillinger, C.T., Milledge, H.J., Mendelssohn, M., Seal, M., 1987. Multiple growth events during diamond genesis: an integrated study of carbon and nitrogen isotopes and nitrogen aggregation state in coated stones. Earth and Planetary Science Letters 86, 341–353.

Bulanova, G.P., Pearson, D.G., Hauri, E.H., Griffin, B.J., 2002. Carbon and nitrogen isotope systematics within a sector-growth diamond from the Mir kimberlite, Yakutia. Chemical Geology 188, 105–123.

Cartigny, P., Farquhar, J., Thomassot, E., Harris, J.W., Wing, B., Masterson, A., McKeegan, K., Stachel, T., 2009. A mantle origin for Paleoarchean peridotitic diamonds from the Panda kimberlite, Slave Craton: Evidence from ^{13}C-, ^{15}N- and $^{33,34}S$-stable isotope systematics. Lithos 112, 852–864.

Cartigny, P., Stachel, T., Harris, J.W., Javoy, M., 2004. Constraining diamond metasomatic growth using C- and N-stable isotopes: examples from Namibia. Lithos 77, 359–373.

Chinn, I.L., Gurney, J.J., Kyser, K.T., 1998. Diamonds and mineral inclusions from the NWT, Canada, in: Extended Abstracts. Presented at the 7th International Kimberlite Conference, Cape Town.

Creaser, R.A., Grütter, H., Carlson, J., Crawford, B., 2004. Macrocrystal phlogopite Rb-Sr dates for the Ekati property kimberlites, Slave Province, Canada: evidence for multiple intrusive episodes in the Paleocene and Eocene. Lithos 76, 399–414.

Creighton, S., Stachel, T., Eichenberg, D., Luth, R., 2010. Oxidation state of the lithospheric mantle beneath Diavik diamond mine, central Slave craton, NWT, Canada. Contributions to Mineralogy and Petrology 159, 645–657.

Creighton, S., Stachel, T., McLean, H., Muehlenbachs, K., Simonetti, A., Eichenberg, D., Luth, R., 2008. Diamondiferous peridotitic microxenoliths from the Diavik Diamond Mine, NT: Contributions to Mineralogy and Petrology 155, 541–554.

Davies, R.M., Griffin, W.L., O'Reilly, S.Y., Doyle, B.J., 2004. Mineral inclusions and geochemical characteristics of microdiamonds from the DO-27, A154, A21, A418, DO18, DD17 and Ranch Lake kimberlites at Lac de Gras, Slave Craton, Canada. Lithos 77, 39–55.

Davies, R.M., Griffin, W.L., Pearson, N.J., Andrew, A.S., Doyle, B.J., O'Reilly, S.Y., 1999. Diamonds from the deep; Pipe DO-27, Slave Craton, Canada. Proceedings of the 7th International Kimberlite Conference 1, 148–155.

Deines, P., 1980. The carbon isotopic composition of diamonds: relationship to diamond shape, color, occurrence and vapor composition. Geochimica et Cosmochimica Acta 44, 943–961.

Donnelly, C.L., Stachel, T., Creighton, S., Muehlenbachs, K., Whiteford, S., 2007. Diamonds and their mineral inclusions from the A154 South pipe, Diavik Diamond Mine, Northwest territories, Canada. Lithos 98, 160–176.

Evans, T., 1992. Aggregation of nitrogen in diamond, in The properties of natural and synthetic diamond, Academic Press, London, pp. 259–289.

Evans, T., Harris, J.W., 1989. Nitrogen aggregation, inclusion equilibration temperatures and the age of diamonds, in: Kimberlites and Related Rocks, Geological Society of Australia Special Publication. Blackwell, Carlton, pp. 1001–1006.

Evans, T., Kiflawi, I., Luyten, W., Tendeloo, G.V., Woods, G.S., 1995. Conversion of platelets into dislocation loops and voidite formation

in Type IaB diamonds. Proceedings: Mathematical and Physical Sciences 449, 295–313.

Fitzsimons, I.C.W., Harte, B., Chinn, I.L., Gurney, J.J., Taylor, W.R., 1999. Extreme chemical variation in complex diamonds from George Creek, Colorado; a SIMS study of carbon isotope composition and nitrogen abundance. Mineralogical Magazine 63, 857 –878.

Goss, J.P., Coomer, B.J., Jones, R., Fall, C.J., Briddon, P.R., Öberg, S., 2003. Extended defects in diamond: The interstitial platelet: Physical Review B 67, 165208.

Griffin, W.L., Doyle, B.J., Ryan, C.G., Pearson, N.J., Suzanne, Y.O., Davies, R., Kivi, K., Van Achterbergh, E., Natapov, L.M., 1999. Layered mantle lithosphere in the Lac de Gras area, slave craton: composition, structure and origin. Journal of Petrology 40, 705 –727.

Gurney, J.J., Hildebrand, P.R., Carlson, J.A., Fedortchouk, Y., Dyck, D.R., 2004. The morphological characteristics of diamonds from the Ekati property, Northwest Territories, Canada. Lithos 77, 21–38.

Haggerty, S.E., 1986. Diamond genesis in a multiply-constrained model. Nature 320, 34–38.

Hanley, P.L., Kiflawi, I., Lang, A.R., 1977. On topographically identifiable sources of cathodoluminescence in natural diamonds. Phil. Trans. R. Soc. Lond. A 284, 329–368.

Harte, B., Fitzsimons, I.C.W., Harris, J.W., Otter, M.L., 1999. Carbon isotope ratios and nitrogen abundances in relation to cathodoluminescence characteristics for some diamonds from the Kaapvaal Province, S. Africa. Mineralogical Magazine 63, 829 –856.

Hauri, E.H., Pearson, D.G., Bulanova, G.P., Milledge, H.J., 1999. Microscale variations in C and N isotopes within mantle diamonds revealed by SIMS. Proceedings of the VIIth International Kimberlite Conference 1, 341–347.

Hauri, E.H., Wang, J., Pearson, D.G., Bulanova, G.P., 2002. Microanalysis of $\delta^{13}C$, $\delta^{15}N$, and N abundances in diamonds by secondary ion mass spectrometry. Chemical Geology 185, 149–163.

Howell, D., O'Neill, C.J., Grant, K.J., Griffin, W.L., Pearson, N.J., O'Reilly, S.Y., 2012. μ-FTIR mapping: Distribution of impurities in different

types of diamond growth. Diamond and Related Materials 29, 29–36.

Johnson, C.N., Stachel, T., Muehlenbachs, K., Stern, R.A., Armstrong, J.P., EIMF, 2012. The micro-/macro-diamond relationship: A case study from the Artemisia kimberlite (Northern Slave Craton, Canada). Lithos 148, 86–97.

Kiflawi, I., Bruley, J., Luyten, W., Van Tendeloo, G., 1998. “Natural” and “man-made” platelets in type-Ia diamonds: Philosophical Magazine Part B 78, 299–314.

Klein-BenDavid, O., Izraeli, E.S., Hauri, E., Navon, O., 2004. Mantle fluid evolution-a tale of one diamond. Lithos 77, 243–253.

Klein-BenDavid, O., Izraeli, E.S., Hauri, E., Navon, O., 2007. Fluid inclusions in diamonds from the Diavik mine, Canada and the evolution of diamond-forming fluids: Geochimica et Cosmochimica Acta 71, 723–744.

Leahy, K., Taylor, W., 1997. The influence of the Glennie domain deep structure on the diamonds in Saskatchewan kimberlites. Russian Geology and Geophysics 38, 481–491.

Malkovets, V. g., Griffin, W. l., O’Reilly, S. y., Wood, B. j., 2007. Diamond, subcalcic garnet, and mantle metasomatism: Kimberlite sampling patterns define the link. Geology 35, 339 –342.

McCandless, T.E., Waldman, M.A., Gurney, J.J., 1994. Macrodiamonds and microdiamonds from Murfreesboro lamproites, Arkansas; morphology, inclusions and carbon isotope geochemistry, in: Meyer, H.O.A., Leonardos, O.H. (Eds.), Proceedings of the 5th International Kimberlite Conference. Companhia de Pesquisa de Recursos Minerais (CPRM), Rio de Janeiro, pp. 78–97.

Mendelssohn, M.J., Milledge, H.J., 1995. Geologically significant information from routine analysis of the mid-infrared spectra of diamonds. International Geology Review 37, 95–110.

Menzies, A., Westerlund, K., Grütter, H., Gurney, J., Carlson, J., Fung, A., Nowicki, T., 2004. Peridotitic mantle xenoliths from kimberlites on the Ekati Diamond Mine property, N.W.T., Canada: major element compositions and implications for the lithosphere beneath the central Slave craton. Lithos 77, 395–412.

Moore, D.S., 2000. The Basic Practice of Statistics, 2nd ed. W.H. Freeman and Company, United States of America.

Pattison, D.R.M., Levinson, A.A., 1995. Are euhedral microdiamonds formed during ascent and decompression of kimberlite magma? Implications for use of microdiamonds in diamond grade estimation. Applied Geochemistry 10, 725–738.

Pearson, N.J., Griffin, W.L., Doyle, B.J., O'Reilly, S.Y., van Achterbergh, E., Kivi, K., 1999. Xenoliths from kimberlite pipes of the Lac de Gras area, Slave Craton, Canada. Proceedings of the 7th International Kimberlite Conference 2, 644–658.

Richet, P., Bottinga, Y., Javoy, M., 1977. A Review of Hydrogen, Carbon, Nitrogen, Oxygen, Sulphur, and Chlorine Stable Isotope Fractionation Among Gaseous Molecules. Annual Review of Earth and Planetary Sciences 5, 65–110.

Schulze, D.J., Harte, B., Valley, J.W., Channer, D.M.D., 2004. Evidence of subduction and crust–mantle mixing from a single diamond. Lithos 77, 349–358.

Shiryaev, A.A., Frost, D.J., Langenhorst, F., 2007. Impurity diffusion and microstructure in diamonds deformed at high pressures and temperatures: Diamond and Related Materials 16, 503–511.

Smart, K.A., Chacko, T., Stachel, T., Muehlenbachs, K., Stern, R.A., Heaman, L.M., 2011. Diamond growth from oxidized carbon sources beneath the Northern Slave Craton, Canada: A $\delta^{13}C$–N study of eclogite-hosted diamonds from the Jericho kimberlite. Geochimica et Cosmochimica Acta 75, 6027–6047.

Sobolev, E.V., Lenskaya, S.V., Lisoivan, V.I., 1968. Lamellar formations in the structure of natural diamonds. Journal of Structural Chemistry 9, 917–920.

Sobolev, N.V., Logvinova, A.M., Zedgenizov, D.A., Seryotkin, Y.V., Yefimova, E.S., Floss, C., Taylor, L.A., 2004. Mineral inclusions in microdiamonds and macrodiamonds from kimberlites of Yakutia: a comparative study. Lithos 77, 225–242.

Stachel, T., Harris, J.W., Muehlenbachs, K., 2009. Sources of carbon in inclusion bearing diamonds. Lithos 112, 625–637.

Stachel, T., Harris, J.W., Tappert, R., Brey, G.P., 2003. Peridotitic diamonds from the Slave and the Kaapvaal cratons--similarities and differences based on a preliminary data set. Lithos 71, 489–503.

Tappert, R., Stachel, T., Harris, J.W., Shimizu, N., Brey, G.P., 2005. Mineral inclusions in diamonds from the Panda kimberlite, Slave Province, Canada. Eur J Mineral 17, 423–440.

Taylor, W.R., Jaques, A.L., Ridd, M., 1990. Nitrogen-defect aggregation characteristics of some Australasian diamonds; time-temperature constraints on the source regions of pipe and alluvial diamonds. American Mineralogist 75, 1290–1310.

Tomlinson, E.L., Jones, A.P., Harris, J.W., 2006. Co-existing fluid and silicate inclusions in mantle diamond: Earth and Planetary Science Letters 250, 581–595.

Van Rythoven, A.D., Schulze, D.J., 2009. In-situ analysis of diamonds and their inclusions from the Diavik Mine, Northwest Territories, Canada: Mapping diamond growth. Lithos 112, Supplement 2, 870–879.

Westerlund, K.J., Shirey, S.B., Richardson, S.H., Carlson, R.W., Gurney, J.J., Harris, J.W., 2006. A subduction wedge origin for Paleoarchean peridotitic diamonds and harzburgites from the Panda kimberlite, Slave craton: evidence from Re–Os isotope systematics. Contrib Mineral Petrol 152, 275–294.

Woods, G.S., 1986. Platelets and the infrared Absorption of Type Ia Diamonds. Proceedings of the Royal Society of London. A. Mathematical and Physical Sciences 407, 219 –238.

Woods, G.S., Collins, A.T., 1983. Infrared absorption spectra of hydrogen complexes in type I diamonds. Journal of Physics and Chemistry of Solids 44, 471–475.

Zedgenizov, D.A., Harte, B., Shatsky, V.S., Politov, A.A., Rylov, G.M., Sobolev, N.V., 2006. Directional chemical variations in diamonds showing octahedral following cuboid growth. Contributions to Mineralogy and Petrology 151, 45–57.

Chapter 4 – Fourier Transform Infrared characteristics of natural diamond

4.1. Introduction

Fourier Transform Infrared (FTIR) spectroscopy is a routine analytical technique in diamond research. The diamond crystal lattice absorbs infrared radiation between 1500 cm^{-1} and 2665 cm^{-1} (two-phonon region) with characteristic sharp peaks at 1975 cm^{-1}, 2026 cm^{-1} and 2158 cm^{-1} and a broad peak between 2355 cm^{-1} and 2665 cm^{-1} (Figure 4.1). A one-phonon region due to nitrogen impurities is observed between 1055 cm^{-1} and 1345 cm^{-1} and can be integrated to obtain relative proportions and concentrations of nitrogen species.

Diamonds with singly substituted nitrogen atoms are referred to as Type Ib (Dyer et al., 1965). Single nitrogen atom defects are unstable at mantle conditions and quickly diffuses to form aggregates of nitrogen (Chrenko et al., 1977). Diamonds with aggregated nitrogen (Type Ia) are subdivided into IaA and IaB classes (Sutherland et al., 1954) for diamond with nitrogen pairs (Davies, 1976) and tetrahedrons of four nitrogen atoms surrounding vacancies (Evans and Qi, 1982), respectively. Referred to as aggregation state, the form in which nitrogen occurs can be quantitatively evaluated and is reported as $\%B = 100N_B/[N_A+N_B]$ where N_X is the concnetration of nitrogen atoms in the X center. Deconvolution of the absorption peaks in the one phonon region by a least-squares method of curve fitting returns A (N_2), B (N_4), and D (platelet related) components as absorption coefficient values (peak height) at 1282 cm^{-1}.

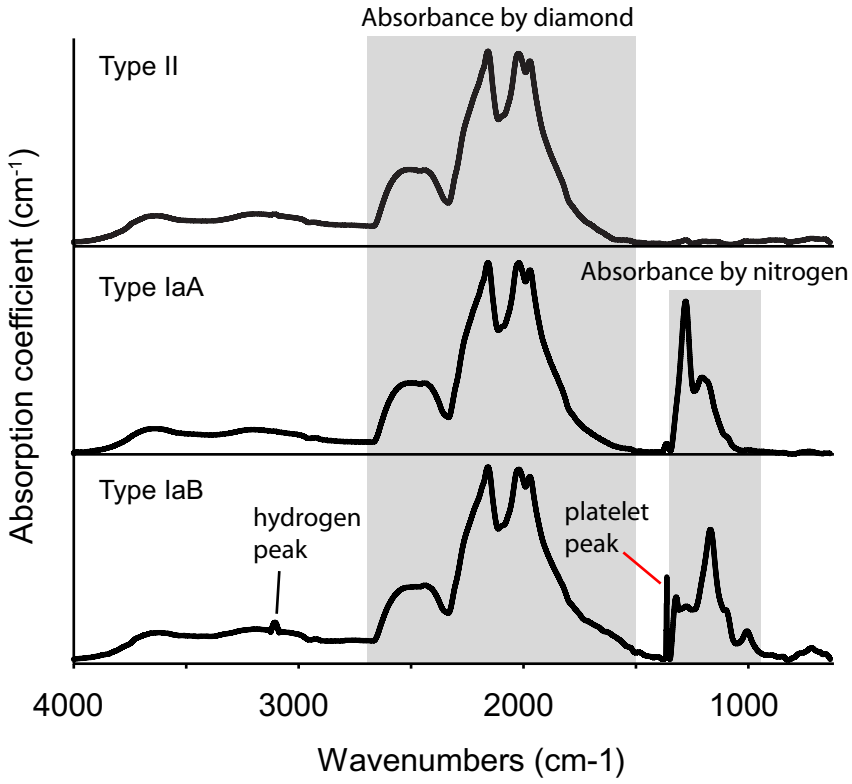

Figure 4.1. Characteristic FTIR spectra of Type II, IaA and IaB diamonds. Type IaAB diamonds have IR spectra reflecting both A and B cetners with heights proportional to the varying proportions of those nitrogen defects.

The migration of N to form pairs and tetrahedrons of four is both a function of time and temperature (Evans and Qi, 1982). A side effect of B-center development is the formation of interstitial carbon defects along {100} called platelets (Evans and Phaal, 1962). Platelets absorb infrared radiation and create a sharp peak (B') in the 1360 to 1375 cm^{-1} range (Woods, 1986) with the exact position depending on platelet size (Mendelssohn and MIlledge, 1995). Additionally, the asymmetry of the B' peak increases as it moves towards lower wavenumbers (i.e. closer to the nitrogen peaks). The platelet peak area correlates with B-center concentrations (N_B) in diamonds without cuboid growth sectors that have not experienced a complex thermal or tectonic history (Woods, 1986; Howell et al., 2012b).

Hydrogen-related peaks cannot be reliably correlated to hydrogen concentration because not all hydrogen complexes in diamond are FTIR active (Sellschop 1992; Sweeney et al., 1999). Nevertheless, integration of these peaks provides information, albeit ambiguous, about hydrogen in diamond. The most prominent and common hydrogen-related absorption peak occurs at 3107 cm^{-1} and has been attributed to either the vibration of bonds in $C=CH_2$ groups (Woods and Collins, 1983) or nitrogen (N_2-H) complexes (Goss et al., 2011).

The purpose of this study is to report new IR data from diamonds from De Beers Pool, South Africa and Akwatia, Ghana together with reprocessed IR data for diamonds from various localities in Brazil, Botswana, South Africa and Canada. This database was compiled to analyze specific IR characteristics of diamonds with various parageneses and from different cratons. With this database the relationship between platelet peak area and N_B concentration is reevaluated and the significance of the hydrogen-related peak at 3107 cm^{-1} is explored.

4.2. Samples

Sixty-nine diamonds from Akwatia, Ghana and 96 from De Beers Pool, South Africa were analyzed by FTIR. These samples were fragmented in previous works to liberate inclusions, thus analyses were performed on residual cleavage fragments. All sample fragments are inclusion free and fully transparent (i.e. “gem-quality”). The samples from Ghana were previously analyzed by Stachel et al. (1997) but that study did not report quantitative hydrogen and platelet peak information. Morphology, color, presence of deformation and carbon isotope data were also reported by Stachel et al. (1997) and are included in the diamond database discussed below. The morphology of samples from Ghana comprises

48% octahedrons, 45% dodecahedroids, 6% macles and 1% mixed. Color distribution is dominated by colorless grains (86%) with lesser brown (13%) and 1% with a transparent green coat.

Information regarding the physical properties of the De Beers Pool samples is not reported by Phillips et al., (2004) with the exception of a general size bracket: DTC -13+5 (circular sieve apertures of 2.9 mm to 1.5 mm). Light brown coloration was observed in 9 samples, and the remaining diamonds are colorless. As the samples are cleavage fragments, it is impossible to make any reliable observations on whole-stone morphology.

4.3. Methods

Prior to analysis, samples were prepared by cleaning with petroleum ether in an ultrasonic bath for 15 minutes. Analyses were made on a Thermo-Nicolet Nexus 470 Fourier transform infrared (FTIR) spectrometer at the De Beers Laboratory for Diamond Research at the University of Alberta (Canada). The spectrometer is coupled to a Continuum microscope that, together with its sample area, is purged with a mixture of nitrogen and oxygen. This gas mixture reduces interferences and helps maintain a constant background signal. Background measurements were taken periodically (every 2 hours to 3 hours) during analytical sessions and automatically subtracted from sample spectra.

Two hundred scans were averaged for each analysis and data were collected between the wavenumbers of 4000 cm^{-1} and 600 cm^{-1} at a spacing of 1.93 cm^{-1}. Subsequent to background removal, spectra were corrected to a baseline and normalized to a 1 cm Type II diamond standard to convert absorbance to absorption coefficient values. The resultant absorption coefficient at 1282 cm^{-1} was deconvoluted into A , B

and D components using a program provided by David Fisher, Diamond Trading Company, Maidenhead, UK. Conversion to atomic parts per million (at. ppm) nitrogen was achieved using the coefficients of 16.5 for A (Boyd et al., 1994) and 79.4 for B components (Boyd et al., 1995). The detection limit for nitrogen is approximately 10 at. ppm, but depends on the quality of the spectrum.

On the same spectra (baselined and converted to absorption coefficient), platelet (1360 cm^{-1} to 1375 cm^{-1} region) and hydrogen (3107 cm^{-1}) peaks were integrated after further local baselining (removal of diamond and nitrogen-related absorbance) and are reported in cm^{-2}. These measurements were carried out using the peak area tool in the Omnic software supplied by Thermo-Nicolet.

Analytical uncertainties for N_T and N_B are typically between 5% and 10%. One variable impacting uncertainty for these two parameters is the method in which a baseline and normalization are applied. To minimize this effect, applying a consistent method for all samples is important. Uncertainty for peak measurements for platelet and hydrogen peaks is < 5% on peaks > 1.0 cm^{-1}.

4.4. Results

Nitrogen concentrations for the 69 diamonds from Akwatia range from < 10 at. ppm to 1616 at. ppm (median = 106 at. ppm) and include 8 Type II (< 10 at. ppm) samples (Appendix B). N_B concentration is highly variable with a range from 0 at. ppm to 504 at. ppm and the median concentration is 38 at. ppm. Nitrogen aggregation ranges from 0% to 100% IaB, and is skewed to lower values with a median at 38% IaB. Platelet peaks occur in 52 (75%) of diamonds from Akwatia and their areas range from 1.4 cm^{-2} to 196.5 cm^{-2} (median = 23.9 cm^{-2}). Hydrogen peaks are observed in 60

(87%) samples and have a range from 0.2 cm^{-2} to 27.9 cm^{-2} (median = 1.4 cm^{-2}).

The 96 De Beers Pool diamonds have a broadly similar range of nitrogen concentration as Akwatian samples from < 10 at. ppm to 1459 at. ppm (median = 65 at. ppm) but a larger proportion (n=18) of Type II samples (Appendix B). N_B ranges from 0 at. ppm to 557 at. ppm but has a much lower median value (9.4 at. ppm.) than samples from Akwatia. Accordingly, the degree of aggregation is more strongly skewed to lower values than for samples from Akwatia: despite a range of 0% to 100% IaB, the median is 17% IaB. Platelet peaks are observed in 58 (60%) of De Beers Pool samples and their areas range from 0.5 cm^{-2} to 339.2 cm^{-2} (median = 16.6 cm^{-2}). Seventy-eight samples (81%) have hydrogen peaks with areas ranging from 0.2 cm^{-2} to 113.6 cm^{-2} but this population is strongly skewed to lower values (median = 1.1 cm^{-2}).

4.5. Database

A database of 696 diamond samples analyzed at the De Beers Laboratory for Diamond Research was compiled to investigate population characteristics and trends of samples from varying cratons and parageneses (Appendix B). The database contains paragenesis, shape, color, deformation and carbon isotope data reported in the literature. Original spectra from previous studies were reprocessed to apply a consistent methodology for applying baselines and normalization in order to minimize uncertainties. Updated nitrogen concentrations and aggregation states replace original values in the database. Additionally, integrated platelet and hydrogen peak areas were added to the database. Unreliable spectra that could not be corrected for fringing or poor signal detection were removed.

Samples in the database originate from Arenapolis, Boa Vista and Canastra, Brazil (Tappert et al., 2006); Damtshaa, Botswana (Deines et al., 2009); A154 South (Diavik), Panda (Ekati), Renard and Wawa, Canada (Donnelly et al., 2007; Tappert et al., 2005a; Hunt et al., 2012; Stachel et al., 2006, respectively) and Jagersfontein, South Africa (Tappert et al., 2005b). Numbers of samples from different locations based on paragenesis are reported in Table 4.1.

Paragenetic determinations included in the database are based on mineral inclusion type and composition. In general, samples with olivine, Mg-chromite, orthopyroxene, high Ni sulfide, Cr-pyrope garnet or clinopyroxene with Cr# (100Cr/Cr+Al) > ~7 to 10 are considered peridotitic. The peridotitic classification can be further subdivided into lherzolitic (fertile to mildly depleted) and harzburgitic (strongly depleted) based on Ca contents of garnet and the presence of clinopyroxene (e.g., Grütter et al., 2004). Eclogitic samples are those with low Cr (< 1 wt% Cr_2O_3) garnet and Na-rich clinopyroxene inclusions.

Peridotitic samples (including subdivisions of harzburgitic and lherzolitic) account for 68% of the dataset and 16% are eclogitic. Deep eclogitic

Location	p	l	h	e	w	deep-e	deep-h	lm	uk	Total
Akwatia	39	5	20	1	1		1		2	69
Arenapolis	14								4	18
Boa Vista	16		10	1					2	29
Canastra	7			1					6	14
Damtshaa	43		8	38	2					91
De Beers Pool	41		41	13			1			96
Diavik	40	3	2	7					3	55
Jagersfontein	21		10	42	4	10			23	110
Panda	40	12	22	7				5	4	90
Renard	57	6	5						32	100
Wawa	14		1				1		8	24
Total	332	26	119	110	7	10	3	5	84	696

Table 4.1. Table showing the distribution of inclusion parageneses for the different locations in the database. Parageneses are p = peridotitic (unspecified), l = lherzolitic, h = harzburgitic, e = eclogitic, w = websteritic, deep-e = majoritic eclogitic garnet inclusions, deep-h = majoritic harzburgitic garnet inclusions, lm = lower mantle and uk = unknown.

and peridotitic samples (i.e. presence of a majorite component in garnet) combined are 2% and websteritic and lower mantle samples account for 1%, each. For the remaining 12% no paragenesis is assigned because either no inclusion was recovered or their inclusions were indeterminate.

Fifty-six percent of the samples in the database have morphology information reported. Of this 56%, octahedra, dodecahedra and irregular forms are the most common with 32%, 26% and 25%, respectively. Macles account for 8% of the database and cubic samples are less than 1%. The remaining 8% of samples with morphology information have either mixed morphologies or are aggregates. Color is recorded for 70% of samples and colorless and brown samples dominate this population (64% and 30%, respectively) followed by much lower proportions of green (3%), yellow (1%) and pink (<1%). The presence or absence of plastic deformation is reported for 53% of samples and positively identified in 19% of these.

Quantitative data in the database include carbon isotopic composition, nitrogen concentration, N_B concentration, hydrogen peak area and platelet peak area. The diamond type is calculated from the proportion of IaB where $N_B < 10\%$ = IaA, $10\% \leq N_B \leq 90\%$ = IaAB and $N_B > 90\%$ = IaB.

Nitrogen concentration differences between eclogitic and peridotitic parageneses are illustrated in Figure 4.2. Peridotitic samples show a near exponential decrease in nitrogen concentration from 0 at. ppm (e.g. Type II) to 1749 at. ppm. nitrogen with a median at 110 at. ppm. The high counts in the < 100 at. ppm. bin includes 58 Type II samples (25% of bin) which predominantly come from De Beers Pool, Renard and Akwatia.

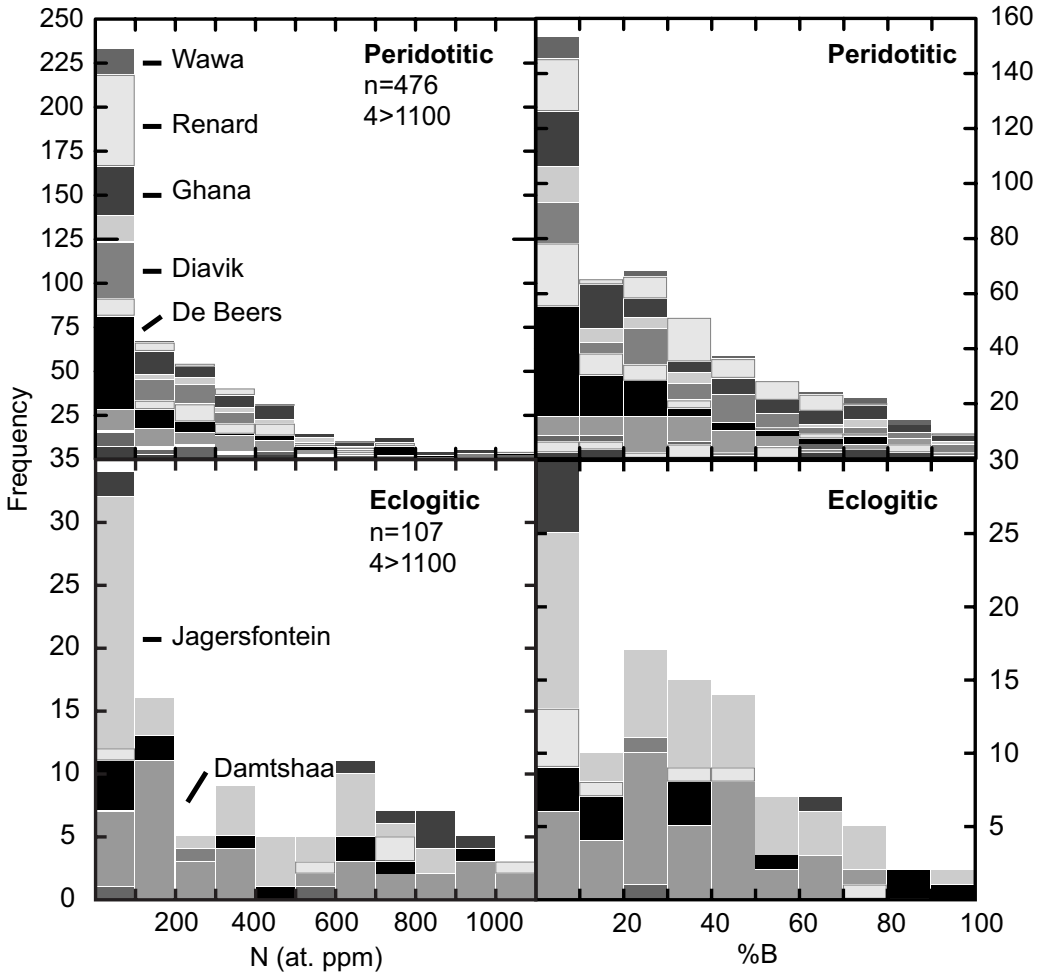

Figure 4.2. Histograms from a worldwide database of nitrogen contents (at. ppm) and %B of peridotitic (top) and eclogitic (bottom) diamonds. Locations with significant numbers of samples are labeled on the diagram.

Although eclogitic samples have a similar range (0 at. ppm to 1739 at. ppm.) as peridotitic samples, they have a more varied distribution with a higher median at 311 at. ppm. Modes occur at 0-100 at. ppm, 300-400 at. ppm and 600-700 at. ppm. nitrogen, similar to results from a larger worldwide database illustrated in Figure 11 of Stachel et al. (2009). The 0 at. ppm to 100 at. ppm nitrogen bin includes 10 Type II diamonds (29% of bin) and is dominated by samples from Jagersfontein which has a high proportion of eclogitic samples (not including deep eclogitic) with N < 100 at. ppm. (n = 20).

The degree of nitrogen aggregation in peridotitic samples has a near exponential decrease towards higher degrees of aggregation whereas the eclogitic subpopulation has a second mode in the 20% to 50% range (Figure 4.2).

4.6. Carbon Isotopes

Carbon isotope data (‰ $\delta^{13}C_{VPDB}$) are reported for 82% of the smaples in the database. When $\delta^{13}C$ data is plotted against nitrogen concentration, a majority of samples cluster around the average mantle $\delta^{13}C$ value of -5‰ (Deines, 1980) and extend up past 1500 at. ppm N. Correlations between $\delta^{13}C$ and nitrogen are not apparent, however, a relationship of decreasing nitrogen content with $\delta^{13}C$ values moving away from -5‰ in either direction is observed in Figure 4.3 (Stachel et al., 1997; Cartigny et al., 2001). The nitrogen concentration decrease is steeper towards values >-5‰ than those <-5‰. These relationships between $\delta^{13}C$ and nitrogen are explored in greater detail by Stachel et al. (2009). Figure 4.3a illustrates the lack of correlation between nitrogen concentration and carbon isotope composition in addition to degree of nitrogen aggregation (i.e. Type). Figure 4.3b, however, shows strong population differences in carbon isotope composition. This is to be expected as eclogitic (including deep samples) are, on average, isotopically ^{13}C-depleted compared to peridotitic samples (Stachel et al., 2009). Nitrogen concentration distributions completely overlap in all diamonds, regardless of parageneses. Nevertheless, eclogitic samples have an average N concentration that is 228 at. ppm greater than average peridotitic diamonds (459 at. ppm versus 231 at. ppm, respectively).

The hydrogen-related 3107 cm^{-1} center has been shown to migrate to a lower wavenumber (3098 cm^{-1}) in highly ^{13}C-doped synthetic diamonds

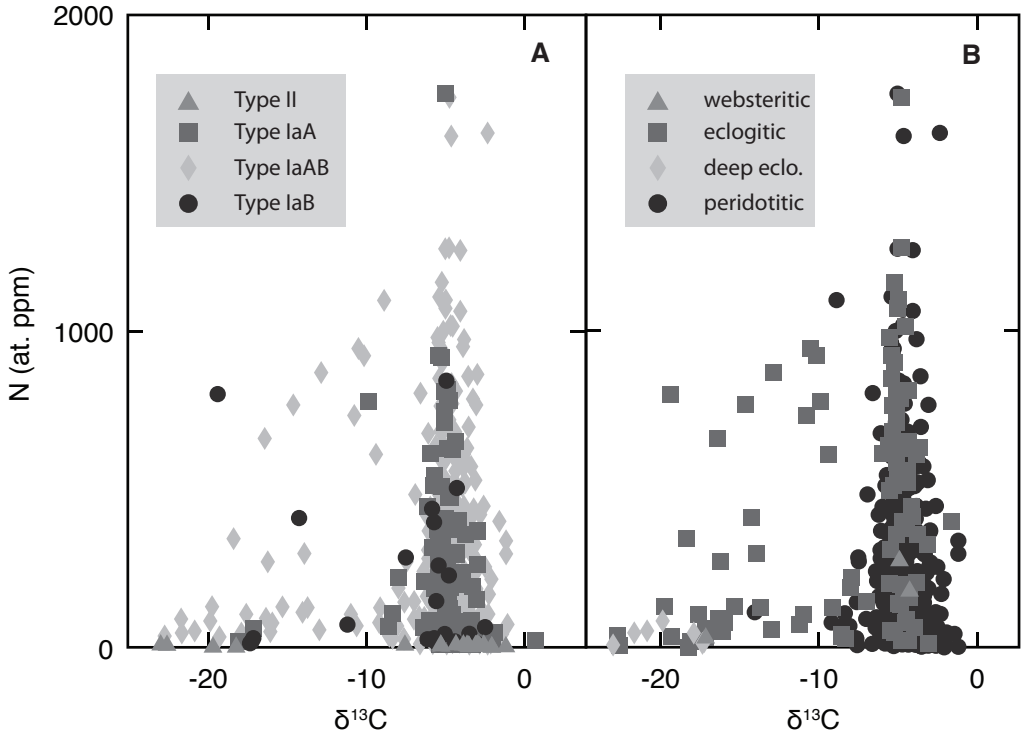

Figure 4.3. Total nitrogen (at. ppm) versus $\delta^{13}C$ values. Symbols are based on either (A) diamond Type (proxy for degree of aggregation) or (B) paragenesis.

(De Weerdt et al., 2003). Although those samples have isotopic compositions beyond natural values, nominal peaks on the shoulder of 3107 cm^{-1} centers in some natural diamonds have been attributed to absorption by ^{13}C-H bonds (Woods and Collins, 1983). These small peaks were not resolvable in any of the samples in the dataset, including those with extreme $\delta^{13}C$ values.

4.7. "Regular" diamonds

A linear relationship between the strength of the B component absorption and the integrated platelet-related absorption peak in FTIR spectra was recognized by Woods (1986). "Regular" samples are those that adhere to this linear relationship and samples that deviated significantly from this line are termed "irregular." The cause of irregularity in some samples has

been attributed to transient heating and/or shearing events that effectively anneal the defects (Evans et al., 1995; Woods 1986). Such platelet degradation results in a smaller than expected platelet peak area for a given N_B concentration.

More recent findings indicate that cuboid growth sectors are more resistant to the formation of platelets (Howell et al, 2012b). Disc-crack-like defects in cuboid growth sectors (Walmsley et al., 1987) may be responsible for preventing interstitial carbon from migrating into IR absorbing clusters. This means the term “irregular” cannot be applied meaningfully to cuboid diamonds as they may not have experienced any platelet degradation. Rather, their platelet formation has been stunted by intrinsic defects of the cuboid habit (Howell et al., 2012a). Therefore, only non-cuboid diamonds that are not fully aggregated and do not adhere to the linear relationship between N_B and I(B’) area can be termed “irregular” and a complex thermal or deformational history is implied.

The samples contained in the database (Appendix B) are inclusion bearing, “gem-quality” diamonds. These inclusions were either silicates or oxides large enough to be liberated and analyzed and are not the sub-microscopic, light-scattering inclusions commonly found in cuboid growth sectors (Welbourn et al., 1989). Despite the absence of such micro-inclusions, some gem-quality diamonds can have a mixed growth habit where octahedral and cuboid sectors grow simultaneously. This can result in a center-cross pattern that is only detectable with techniques like cathodoluminescence or X-ray topography (i.e. Lang, 1974). In the absence of such data, other information is necessary to identify samples where cuboid growth potentially accounts for a significant proportion of a diamond’s volume. One way to identify such samples is to use 3107 cm^{-1} peak data. Fritsch and Scarratt (1993) found that cuboid-growth

layers are commonly hydrogen rich (e.g. Rondeau et al., 2004) and define samples as “H-rich” when the absorbance at 3107 cm^{-1} centers exceeds the intrinsic diamond absorbance at 2450 cm^{-1}. This is the case for 28 samples in the database and therefore these are suspected of containing cuboid growth sectors. By excluding these samples, the categorization of Woods (1986) into “regular” and “irregular” can be evaluated with more confidence.

Plotting N_B concentration versus platelet peak area (Fig. 4.4) reveals an overwhelming majority of samples in the database adhere to the linear “regular” relationship. Here this relationship is established as I(B’) = 0.61 N_B where I(B’) is the integrated area of the platelet peak (cm^{-2}) and N_B is the concentration of B-centers (at. ppm) and the units of the slope of the line is cm^{-2}/at. ppm.

Based on the number of samples in the database, this line can be reliably extrapolated up to ~550 at. ppm N_B. The number of samples in our database with $N_B > 550$ at. ppm is too small to extrapolate the line with confidence beyond this point. The increase in spread in samples where $N_B < 50$ at. ppm is most likely due to increased uncertainty in the determination of N_B and platelet peak area at low total nitrogen contents and platelet concentrations. Type IaB diamonds are also excluded from Figure 4.4 as the platelet-N_B relationship breaks down once nitrogen is completely aggregated.

4.8. Platelet degradation

If degradation of platelets was a by-product of heating, as suggested by Evans et al. (1995), then a correlation between degree of “irregularity” and time averaged mantle residence temperatures should be observed. Figure 4.5 plots the degree of platelet degradation (ratio of platelet peak

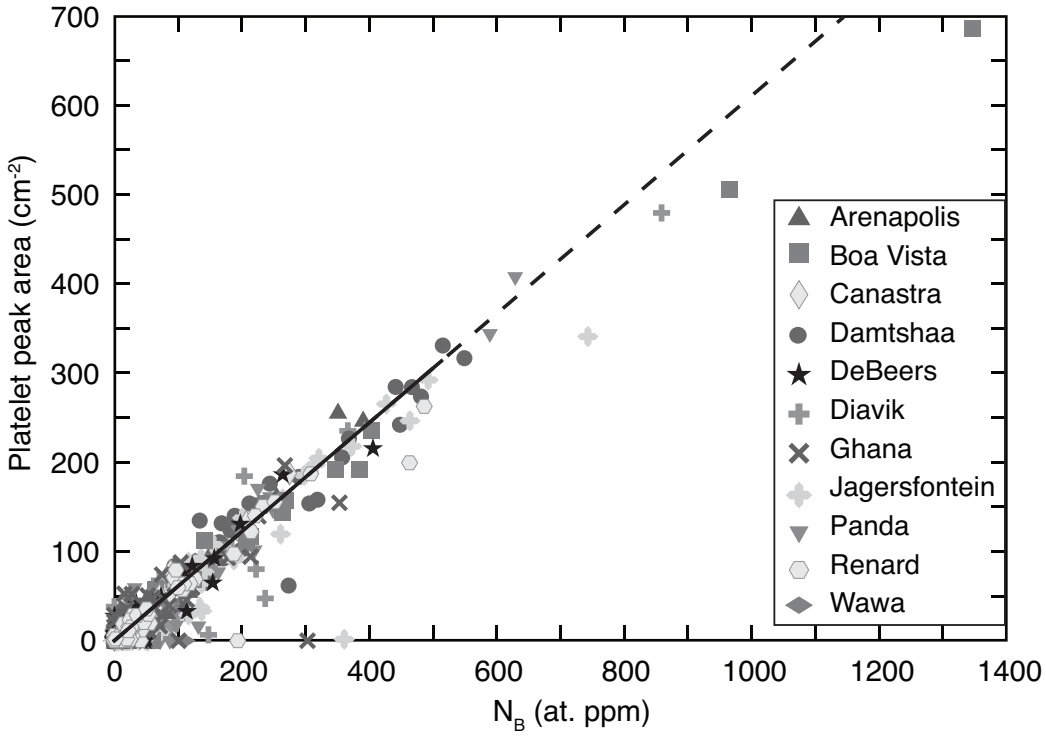

Figure 4.4. Plot of N_B (at. ppm) and platelet peak area (cm^{-2}). The solid black line defines a "regular" trend where N_B and platelet peak (I(B')) area have a linear correlation related by the equation $I(B') = 0.61N_B$. This line may be extrapolated past 550 at. ppm (dashed portion) but with reduced confidence as the number of samples beyond this point is very small. The samples plotted here are assumed to be free of cuboid growth sectors (see text for filtering procedure). Pure type IaB samples were also excluded.

area and N_B concentration normalized to the slope (0.61) of the regular trend in Figure 4.5). Those samples that plot between a normalized I(B')-N_B ratio of 0.9 and 1.1 are considered "regular" (grey bar). Samples that fall below this range are variably platelet degraded. A lack of any positive correlation in these plots suggests that platelet degradation is not principally dependent on temperature. Indeed, it would seem that temperature (as measured by T_N) has a minor role, as a large proportion of degraded samples fall below 1150ºC. This observation indicates that another process, most likely strain (Woods, 1986), is the dominant cause of platelet degradation. At temperatures > 1250ºC the proportion of

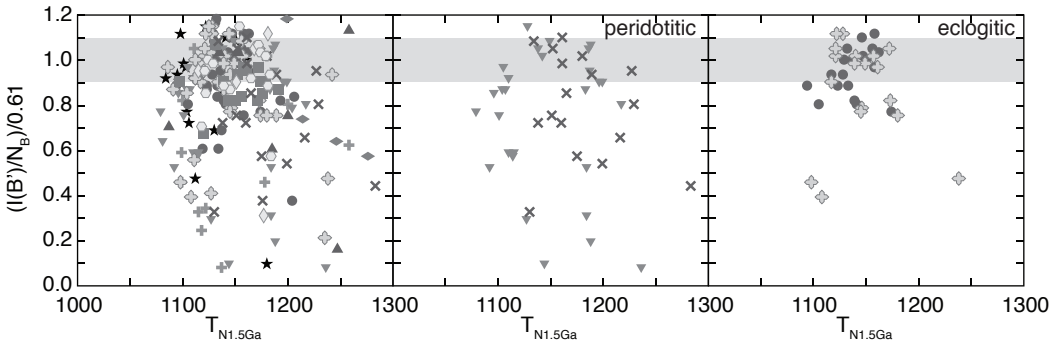

Figure 4.5. Normalized ratio of I(B')/NB versus time averaged mantle residence temperatures (TN1.5 Ga). Samples with NB < 50 at. ppm were excluded to avoid increased uncertainty associated with small amounts of B aggregates (and associated small platelet peaks). Pure IaA and IaB samples were also excluded. Peridotitic samples are from Panda and Ghana and eclogitic samples are from Damtshaa and Jagersfontein. The grey bar between x-axis values of 0.9 and 1.1 indicate the window of "regular" diamonds.

degraded samples increases which likely is a result of increased strain in the deeper (and hotter) parts of the lithosphere close to the lithosphere-asthenosphere boundary. In such a high temperature regime, softening of the diamond lattice may aid plastic deformation.

To eliminate possible scatter caused by plotting diamonds of various parageneses (possibly involving multiple generations of diamond with strongly variable residence times), peridotitic (Panda and Ghana) and eclogitic (Damtshaa and Jagersfontein) diamonds from four sources with high data density were separated out. These filtered datasets confirm that even on the level of single parageneses and individual mines, correlations between the degree of platelet degradation and residence temperature are not observed. These comparisons assume that all samples of a certain paragenesis from a single location have broadly similar ages (e.g., for all Panda peridotitic diamonds it is generally assumed that their formation occurred in the Paleoarchean, Westerlund et al., 2006).

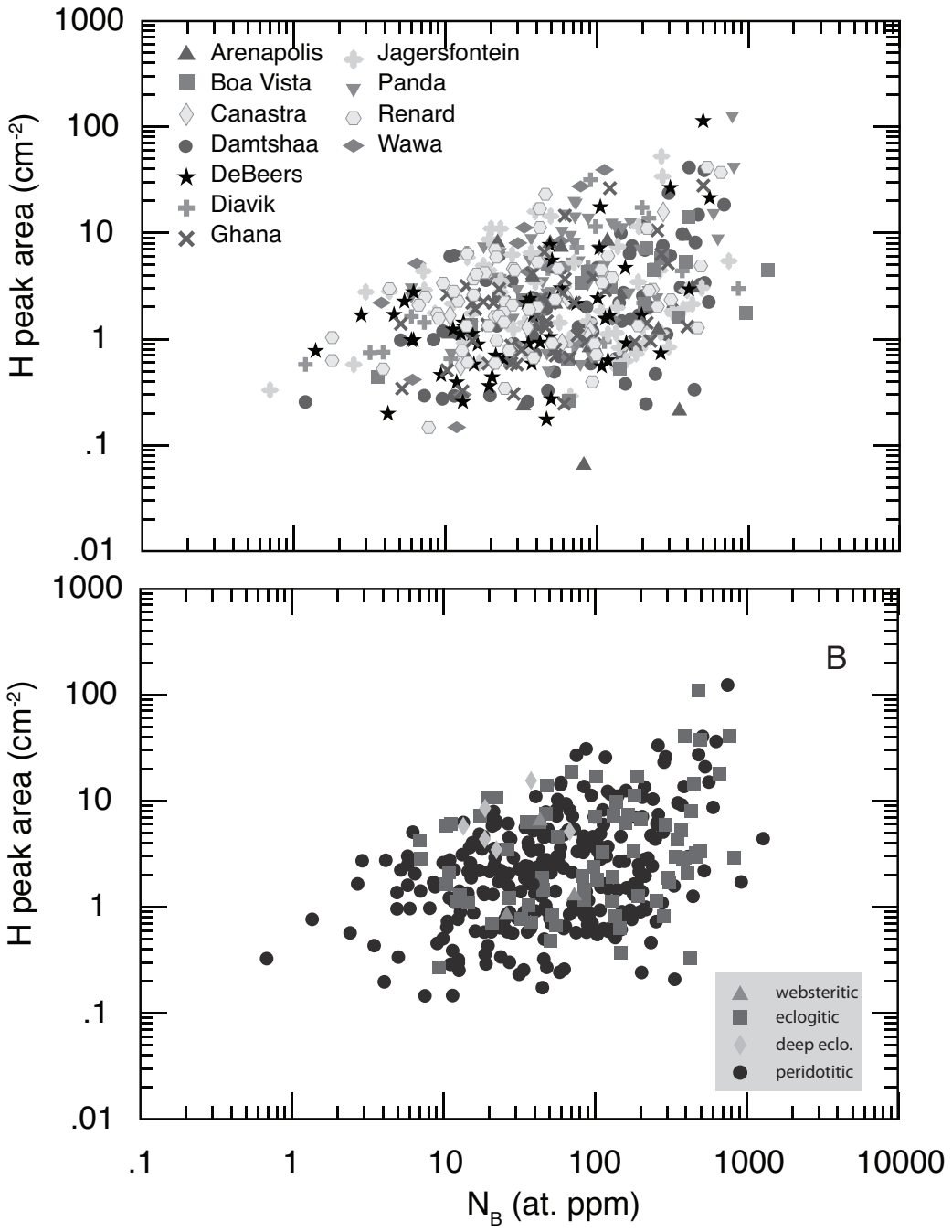

Figure 4.6. Hydrogen related peak (3107 cm^{-1}) area versus N_B illustrating the relationship between maximum H peak area and N_B concentrations. These plots exclude samples with negligible B-center nitrogen (Type II and Type IaA). The top plot shows distribution of samples based on location of origin and the bottom plot shows distribution based on paragenesis.

4.9. The hydrogen-nitrogen relationship

The presence of IR active hydrogen is commonly attributed to C-H bonding, specifically in the C=CH2 (vinylidene) complex (Woods 1986). The stretching of the C-H bonds is predicted to cause IR absorption close to the 3107 cm^{-1} peak and the associated peak at 1405 cm^{-1} can be explained by a scissoring vibration of the two C-H bonds (Bellamy, 1975). More recent theoretical models, however, link the 3107 cm^{-1} absorption with nitrogen, at least indirectly (Chevallier et al., 2002; Goss et al., 2002). Correlations between nitrogen and IR-active hydrogen have been observed in synthetic diamond (Kiflawi et al., 1996) and in natural diamond from Argyle (Iakoubovskii and Adriaenssens, 2002). This relationship is supported by experiments and theoretical calculations relating the 3107 cm^{-1} center to nitrogen aggreates (de Weerdt and Collins, 2006; Goss et al., 2011).

Using the compiled database, the potential for a relationship between the hydrogen peak area (at 3107 cm^{-1}) and nitrogen characteristics can be explored in natural diamond samples from around the world. Eighty percent of the samples in the database have detectable 3107 cm^{-1} peaks with a median peak area of 1.79 cm^{-2}. Type II and IaA diamonds have the smallest proportion of hydrogen peaks at 68% and 64% as well as the smallest median peak area values at 1.02 and 1.42 cm^{-2}, respectively. Type IaAB and IaB samples have much higher proportions at 85% and 91%, respectively. The median peak area for these two subpopulations are also higher: 2.16 and 7.30 cm^{-2}, respectively. These results indicate a link between aggregated (B-center) nitrogen and IR-active hydrogen at 3107 cm^{-1}.

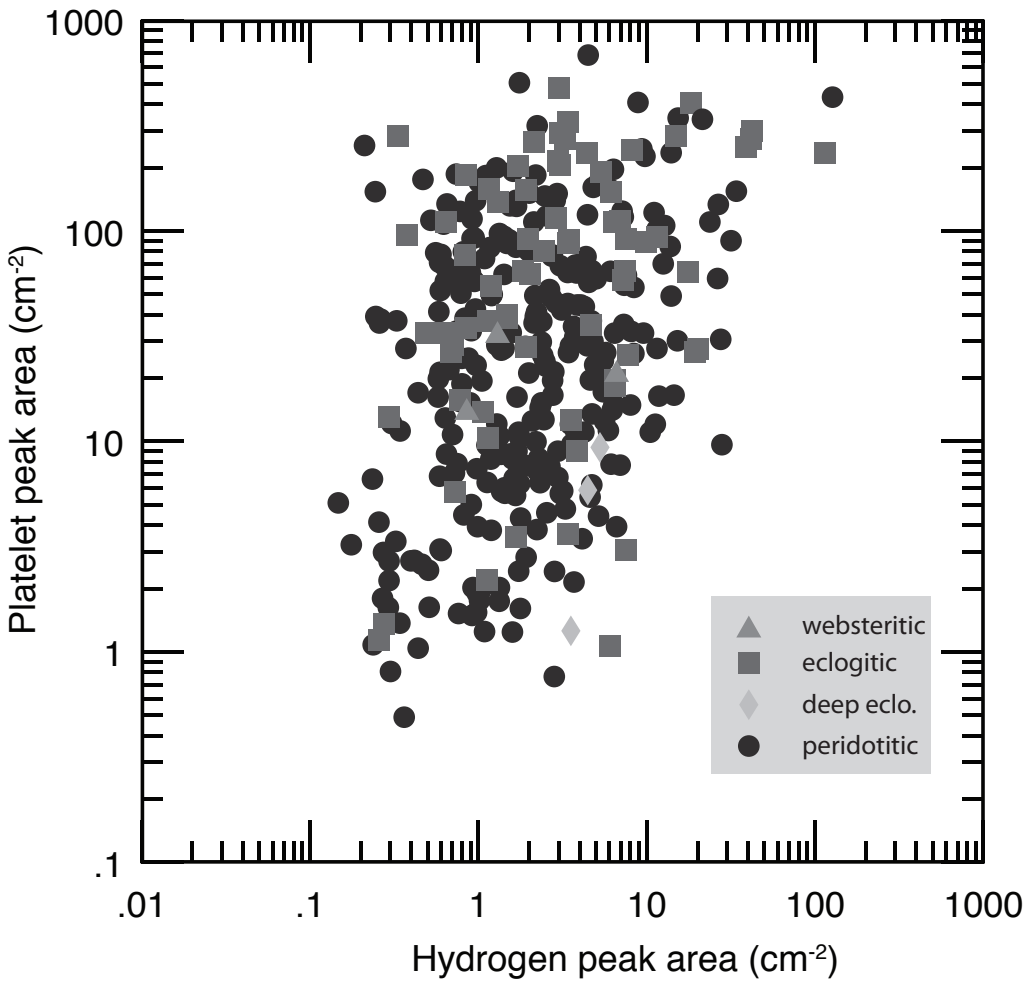

Figure 4.7. Hydrogen peaks versus platelet peaks in diamond.

This relationship is further supported by the correlation between maximum 3107 cm^{-1} peak areas and B-center concentration (see Figure 4.5). As IaB concentrations increase, a well defined limit in maximum H-peak area increases exponentially. Such a defined limit is only weakly observed with A-center concentrations, suggesting the link between nitrogen and IR-active hydrogen is strongest with nitrogen B-centers.

This relationship can be explained if the nitrogen aggregation mechanism affects hydrogen impurities in a way that converts them into IR-absorbing centers. The maximum 3107 cm^{-1} peak area then would be a function of

the available hydrogen content in the diamond, the nitrogen concentration and the degree of aggregation. As N_3 centers are well established as a by-product of progressive nitrogen aggregation from A- to B-centers, a similar relationship also appears likely for them.

Small H-peak areas in diamonds with high nitrogen concentrations and aggregation states can be explained by low concentrations of available hydrogen. Samples with high concentrations of available hydrogen, however, may still have small 3107 cm^{-1} peaks if nitrogen aggregation has not progressed far enough to allow for formulation of N_3 and B-centers, causing the hydrogen to be IR-active.

Despite the relationship between IR-active H and N_B, 3107 cm^{-1} centers are not exclusive to nitrogen bearing diamonds. Sixty-five of the 95 Type II diamonds in the database have measurable, although relatively small, hydrogen peaks (see Figure 4.5). A similar observation of a Type II diamond with weak absorption coefficient of 0.02 cm^{-1} at 3107 cm^{-1} was reported by Kiflawi et al. (1996). One possible explanation for this is if the diamond growth process incorporates a small proportion of hydrogen in intrinsically IR-active defects.

It is also observed that, regardless of location or paragenesis, samples completely overlap and show no perceptible differences nor correlations in H peak area and N_B (see Fig. 4.5). Similarly, Figure 4.6 shows how no correlation or other relationship is discernible between hydrogen peak area versus platelet peak area based on paragenesis. These tests indicate the formation of IR-active hydrogen centers, nitrogen aggregation and the associated development of the platelet peak are processes that are independent of the diamond's host rock composition.

4.10. Conclusions

A database of FTIR data for 696 samples is used to delineate the trend for “regular” samples that abide by the linear relationship between platelet peak area and N_B concentration (Woods, 1986). For cuboid diamond, this relationship does not exist (Howell et al., 2012b) The samples in the database are all fully transparent, i.e. fibrous cuboid growth was not present. In addition, all “hydrogen-rich” samples (characteristic for cuboid growth) were removed from the dataset. An overwhelming majority of samples in the remaining database follow the “regular” trend. Those samples which are irregular indicate that platelet degradation is not a consequence of transient heating events, rather, the main influence on this process is sheering.

Irfrared-active hydrogen centers at 3107 cm^{-1} can occur intrinsically in diamond, including nitrogen-free (Type II) samples. The growth of the 3107 cm^{-1} center nevertheless appears to be linked to the process of nitrogen aggregation. With increased concentrations of aggregated nitrogen, specifically the B-center, the maximum hydrogen peak area increases exponentially (Figure 4.5). This agrees with new models linking IR-active hydrogen responsible for the 3107 cm^{-1} center with highly aggregated (N_3 and B-center) defect groups in diamond (De Weerdt and Collins, 2006; Goss et al., 2011).

References

Bellamy, L.J., 1975, The infra-red spectra of complex molecules: Chapman and Hall, London.

Boyd, S.R., Kiflawi, I., and Woods, G.S., 1994, The relationship between infrared absorption and the A defect concentration in diamond: Philosophical Magazine Part B, v. 69, no. 6, p. 1149–1153.

Boyd, S.R., Kiflawi, I., and Woods, G.S., 1995, Infrared absorption by the B nitrogen aggregate in diamond: Philosophical Magazine Part B, v. 72, no. 3, p. 351–361.

Chevallier, J., Jomard, F., Teukam, Z., Koizumi, S., Kanda, H., Sato, Y., Deneuville, A., and Bernard, M., 2002, Hydrogen in n-type diamond: Diamond and Related Materials, v. 11, no. 8, p. 1566–1571.

Chrenko, R.M., Tuft, R.E., and Strong, H.M., 1977, Transformation of the state of nitrogen in diamond: Nature, v. 270, no. 5633, p. 141–144.

Davies, G., 1976, The A nitrogen aggregate in diamond-its symmetry and possible structure: Journal of Physics C: Solid State Physics, v. 9, no. 19, p. L537–L542.

Deines, P., 1980, The carbon isotopic composition of diamonds: relationship to diamond shape, color, occurrence and vapor composition: Geochimica et Cosmochimica Acta, v. 44, p. 943–961.

Deines, P., Stachel, T., and Harris, J.W., 2009, Systematic regional variations in diamond carbon isotopic composition and inclusion chemistry beneath the Orapa kimberlite cluster, in Botswana: Lithos, v. 112, Supplement 2, no. 0, p. 776–784.

Donnelly, C.L., Stachel, T., Creighton, S., Muehlenbachs, K., and Whiteford, S., 2007, Diamonds and their mineral inclusions from the A154 South pipe, Diavik Diamond Mine, Northwest territories, Canada: Lithos, v. 98, no. 1-4, p. 160–176.

Dyer, H.B., Raal, F.A., Du Preez, L., and Loubser, J.H.N., 1965, Optical absorption features associated with paramagnetic nitrogen in diamond: Philosophical Magazine, v. 11, no. 112, p. 763–774.

Evans, T., Kiflawi, I., Luyten, W., Tendeloo, G.V., and Woods, G.S., 1995, Conversion of platelets into dislocation loops and voidite formation in Type IaB diamonds: Proceedings: Mathematical and Physical Sciences, v. 449, no. 1936, p. 295–313.

Evans, T., and Phaal, C., 1962, Imperfections in Type I and Type II Diamonds: Proceedings of the Royal Society of London. Series A. Mathematical and Physical Sciences, v. 270, no. 1343, p. 538–552.

Evans, T., and Qi, Z., 1982, The Kinetics of the Aggregation of Nitrogen Atoms in Diamond: Proceedings of the Royal Society of London. A. Mathematical and Physical Sciences, v. 381, no. 1780, p. 159 –178.

Fritsch, E., Hainschwang, T., Massi, L., and Rondeau, B., 2007, Hydrogen-related optical centers in natural diamond: An update: New Diamond and Frontier Carbon Technology, v. 17, no. 2, p. 63–89.

Goss, J.P., Ewels, C.P., Briddon, P.R., and Fritsch, E., 2011, Bistable N2–H complexes: The first proposed structure of a H-related colour-causing defect in diamond: Diamond and Related Materials, v. 20, no. 7, p. 896–901.

Goss, J.P., Jones, R., Heggie, M.I., Ewels, C.P., Briddon, P.R., and Öberg, S., 2002, Theory of hydrogen in diamond: Physical Review B, v. 65, no. 11, p. 115207.

Grütter, H.S., Gurney, J.J., Menzies, A.H., and Winter, F., 2004, An updated classification scheme for mantle-derived garnet, for use by diamond explorers: Lithos, v. 77, no. 1-4, p. 841–857.

Howell, D., O'Neill, C., Grant, K., Griffin, W., O'Reilly, S., Pearson, N., Stern, R., and Stachel, T., 2012a, Platelet development in cuboid diamonds: insights from micro-FTIR mapping: Contributions to Mineralogy and Petrology, v. 164, no. 6, p. 1011–1025.

Howell, D., O'Neill, C.J., Grant, K.J., Griffin, W.L., Pearson, N.J., and O'Reilly, S.Y., 2012b, μ-FTIR mapping: Distribution of impurities in different types of diamond growth: Diamond and Related Materials, v. 29, no. 0, p. 29–36.

Hunt, L., Stachel, T., McCandless, T.E., Armstrong, J., and Muelenbachs, K., 2012, Diamonds and their mineral inclusions from the Renard kimberlites in Quebec: Lithos, v. 142–143, no. 0, p. 267–284.

Iakoubovskii, K., and Adriaenssens, G.., 2002, Optical characterization of natural Argyle diamonds: Diamond and Related Materials, v. 11, no. 1, p. 125–131.

Kiflawi, I., Fisher, D., Kanda, H., and Sittas, G., 1996, The creation of the 3107 cm–1 hydrogen absorption peak in synthetic diamond single crystals: Diamond and Related Materials, v. 5, no. 12, p. 1516–1518.

Lang, A.R., 1974, On the Growth-Sectorial Dependence of Defects in Natural Diamonds: Proceedings of the Royal Society of London. Series A, Mathematical and Physical Sciences, v. 340, no. 1621, p. 233–248.

Mendelssohn, M.J., and Milledge, H.J., 1995, Geologically significant information from routine analysis of the mid-infrared spectra of diamonds: International Geology Review, v. 37, no. 2, p. 95–110.

Phillips, D., Harris, J.W., and Viljoen, K.S., 2004, Mineral chemistry and thermobarometry of inclusions from De Beers Pool diamonds, Kimberley, South Africa: Lithos, v. 77, no. 1-4, p. 155–179.

Rondeau, B., Fritsch, E., Guiraud, M., Chalain, J.-P., and Notari, F., 2004, Three historical “asteriated” hydrogen-rich diamonds: growth history and sector-dependent impurity incorporation: Diamond and Related Materials, v. 13, no. 9, p. 1658–1673.

Sellschop, J.P.F., 1992, Nuclear probes in the study of diamond, in Field, J.E. ed., The properties of natural and synthetic diamond, Academic Press, London, p. 81–179.

Stachel, T., Banas, A., Muehlenbachs, K., Kurszlaukis, S., and Walker, E., 2006, Archean diamonds from Wawa (Canada): samples from deep cratonic roots predating cratonization of the Superior Province: Contributions to Mineralogy and Petrology, v. 151, no. 6, p. 737–750.

Stachel, T., and Harris, J.W., 1997, Syngenetic inclusions in diamond from the Birim field (Ghana) - a deep peridotitic profile with a history of depletion and re-enrichment: Contributions to Mineralogy and Petrology, v. 127, p. 336–352.

Stachel, T., Harris, J.W., and Muehlenbachs, K., 2009, Sources of carbon in inclusion bearing diamonds: Lithos, v. 112, p. 625–637.

Sutherland, G., Blackwell, D., and Simeral, W., 1954, The problem of the two types of diamond: Nature, v. 174, p. 901–904.

Sweeney, R.., Prozesky, V.., Viljoen, K.., and Connell, S., 1999, The sensitive determination of H in diamond by infrared (FTIR) spectroscopy and micro-elastic-recoil (μ-ERDA) techniques: Nuclear Instruments and Methods in Physics Research Section B: Beam Interactions with Materials and Atoms, v. 158, no. 1–4, p. 582–587.

Tappert, R., 2005, The Nature of Diamonds and Their Mineral Inclusions: A Study on Diamonds from the Panda (Canada) and Jagersfontein (South Africa) Kimberlites and from Placer Deposits in Brazil [Ph.D.]: University of Alberta (Canada), 214 p.

Tappert, R., Stachel, T., Harris, J.W., Muehlenbachs, K., Ludwig, T., and Brey, G.P., 2005, Subducting oceanic crust: The source of deep diamonds: Geology, v. 33, no. 7, p. 565–568.

Tappert, R., Stachel, T., Harris, J.W., Muehlenbachs, K., and Brey, G.P., 2006, Placer Diamonds from Brazil: Indicators of the Composition of the Earth's Mantle and the Distance to Their Kimberlitic Sources: Economic Geology, v. 101, no. 2, p. 453–470.

Walmsley, J.C., Lang, A.R., Rooney, M.-L.T., and Welbourn, C.M., 1987, Newly observed microscopic planar defects on 111 in natural diamond: Philosophical Magazine Letters, v. 55, no. 5, p. 209–213.

De Weerdt, F., and Collins, A.T., 2006, Optical study of the annealing behaviour of the 3107 cm– 1 defect in natural diamonds: Diamond and Related Materials, v. 15, no. 4–8, p. 593–596.

Westerlund, K.J., Shirey, S.B., Richardson, S.H., Carlson, R.W., Gurney, J.J., Harris, J.W., 2006. A subduction wedge origin for Paleoarchean peridotitic diamonds and harzburgites from the Panda kimberlite, Slave craton: evidence from Re–Os isotope systematics. Contrib Mineral Petrol 152, 275–294.

Welbourn, C.M., Rooney, M.-L.T., and Evans, D.J.F., 1989, A study of diamonds of cube and cube-related shape from the Jwaneng mine: Journal of Crystal Growth, v. 94, no. 1, p. 229–252.

Woods, G.S., 1986, Platelets and the infrared Absorption of Type Ia Diamonds: Proceedings of the Royal Society of London. A. Mathematical and Physical Sciences, v. 407, no. 1832, p. 219 –238.

Woods, G.S., and Collins, A.T., 1983, Infrared absorption spectra of hydrogen complexes in type I diamonds: Journal of Physics and Chemistry of Solids, v. 44, no. 5, p. 471–475.

Chapter 5 – Conclusions

For decades our understanding of the formation of diamond in the mantle has relied on investigations of mineral inclusions. Recent developments in analytical techniques now enable us to analyze diamond directly. Results indicate contrasting trace-element compositions between gem diamonds and diamond inclusions. Despite the difficulty in obtaining data above the limit of quantification for trace-elements in gem diamond, ratios of certain HFSE from De Beers Pool and Akwatia diamonds imply that these elemental impurities are not hosted by pockets of trapped melt (Fesq et al., 1975). Assuming the establishment of mineral-melt equilibrium, diamond-inclusion compositions can be used to model fluid/melt composition. Such modeled fluids/melts can then then be compared to trace-element patterns derived directly from diamond. In most cases the match between model melts and diamond trace-element patterns is very poor. I infer, therefore, that the trace-element impurities in diamond are being included through processes that are fractionating the elements relative to the diamond-forming medium. In one case, however, trace-element ratios do agree with the composition of a known carbonatitic melt.

If the trace-element impurities are being hosted in dispersed mineral micro-inclusions, then this may account for the disparity between the modeled compositions of diamond growth medium and actual concentrations. To test this, various mixtures of common minerals ± fluid were modeled to match the average compositions of lherzolitic and harzburgitic diamonds. The closest fit model consists of unrealistic modal proportions for a peridotitic source (high proportions of orthopyroxene, minor clinopyroxene and garnet and no olivine). This does not, however, preclude the possibility of trace-elements being accommodated in

gem diamond through a complex and variable mixture of fluid/melt and untested mineral (possibly exotic) inclusions.

Contrary to the difficulties in the analysis of most trace-elements in diamond, nitrogen contentsand carbon isotopic composition can be routinely analyzed with confidence. Such data from micro- and macro-diamonds from the Panda kimberlite (Ekati mine, Canada) indicate a disparity in compositions. Gem-quality micro-diamonds have an average $\delta^{13}C$ value that is 1.3‰ higher than the gem-quality macro-diamonds. Additionally, gem micro-diamonds have higher average and median nitrogen concentrations than the macro-diamonds (differences of 314 at. ppm and 444 at. ppm, respectively) and a lower Type II (N-free) abundance (4% versus 8%). The geochemical disparity between micro- and macro-diamonds indicates differences in either the composition of the diamond-forming fluids/melts or fractionation processes or growth histories.

Time averaged mantle residence temperatures, based on an age of formation of 3.5 Ga (Westerlund et al., 2006), display a bimodal distribution in micro- and macro-diamonds from Panda (Evans and Harris, 1989). The bimodal distribution is segregated by a lack of samples at temperatures between 1130ºC and 1160 ºC. This gap corresponds exactly with an observed compositional boundary between highly depleted (upper) and less depleted (lower) portions of the cratonic lithosphere below the Central Slave Craton (Griffin et al., 1999; Menzies et al., 2004).

FTIR data from world-wide locations have been used to reinvestigate the relationship between platelet development and nitrogen aggregation in diamond. “Regular” diamonds are those whose platelet peak areas are linearly correlated with N_B concentrations (Woods, 1986). This line,

expressed as $I(B') = 0.61N_B$ is only applicable to samples with non-cuboid growth sectors as cuboid growth habit may impede platelet formation (Howell et al., 2012). An overwhelming majority of the samples in the database fall along, or close to, this line. This indicates that many gem-quality, silicate inclusion bearing diamonds have not experienced significant platelet degradation and thus had a mantle residence history that is characterized by the absence of major sheering events.

The newly assembled database also shows a strong relationship between IR-active hydrogen defects measured at 3107 cm^{-1} and the degree of aggregation in natural diamonds. As the concentration of aggregated nitrogen in B-centers increases, a corresponding, exponential increase in maximum 3107 cm^{-1} peak area is observed. This is most likely a result of hydrogen defects being converted to IR-active centers as nitrogen migrates to form aggregates of three (N_3) and then four N (B-center) surrounding a vacancy.

The findings of this thesis further our knowledge of diamond growth processes in the mantle and the behavior of various defects within the diamond lattice. Additional research, however, can provide greater insight into how certain elements are being incorporated into diamond and what that implies about the diamond-forming medium. This insight can be further supported by a detailed analysis of IR-active defects that were not discussed in this text. I would expect to see correlations that relate certain IR peaks with other geochemical properties, included elemental impurities, that have not yet been identified.

References

Evans, T., Harris, J.W., 1989. Nitrogen aggregation, inclusion equilibration temperatures and the age of diamonds, in: Kimberlites and Related Rocks, Geological Society of Australia Special Publication. Blackwell, Carlton, pp. 1001–1006.

Fesq, H.W., Bibby, D.M., Erasmus, C.S., Kable, E.J.D., Sellschop, J.P.F., 1975. A comparative trace-element study of diamonds from Premier, Finsch and Jagersfontein mines, South Africa. Physics and Chemistry of The Earth 9, 817–836.

Griffin, W.L., Doyle, B.J., Ryan, C.G., Pearson, N.J., Suzanne, Y.O., Davies, R., Kivi, K., Van Achterbergh, E., Natapov, L.M., 1999. Layered mantle lithosphere in the Lac de Gras area, slave craton: composition, structure and origin. Journal of Petrology 40, 705 –727.

Menzies, A., Westerlund, K., Grütter, H., Gurney, J., Carlson, J., Fung, A., Nowicki, T., 2004. Peridotitic mantle xenoliths from kimberlites on the Ekati Diamond Mine property, N.W.T., Canada: major element compositions and implications for the lithosphere beneath the central Slave craton. Lithos 77, 395–412.

Woods, G.S., 1986. Platelets and the infrared Absorption of Type Ia Diamonds. Proceedings of the Royal Society of London. A. Mathematical and Physical Sciences 407, 219 –238.

Appendix A: FTIR spectra from Panda micro-diamonds

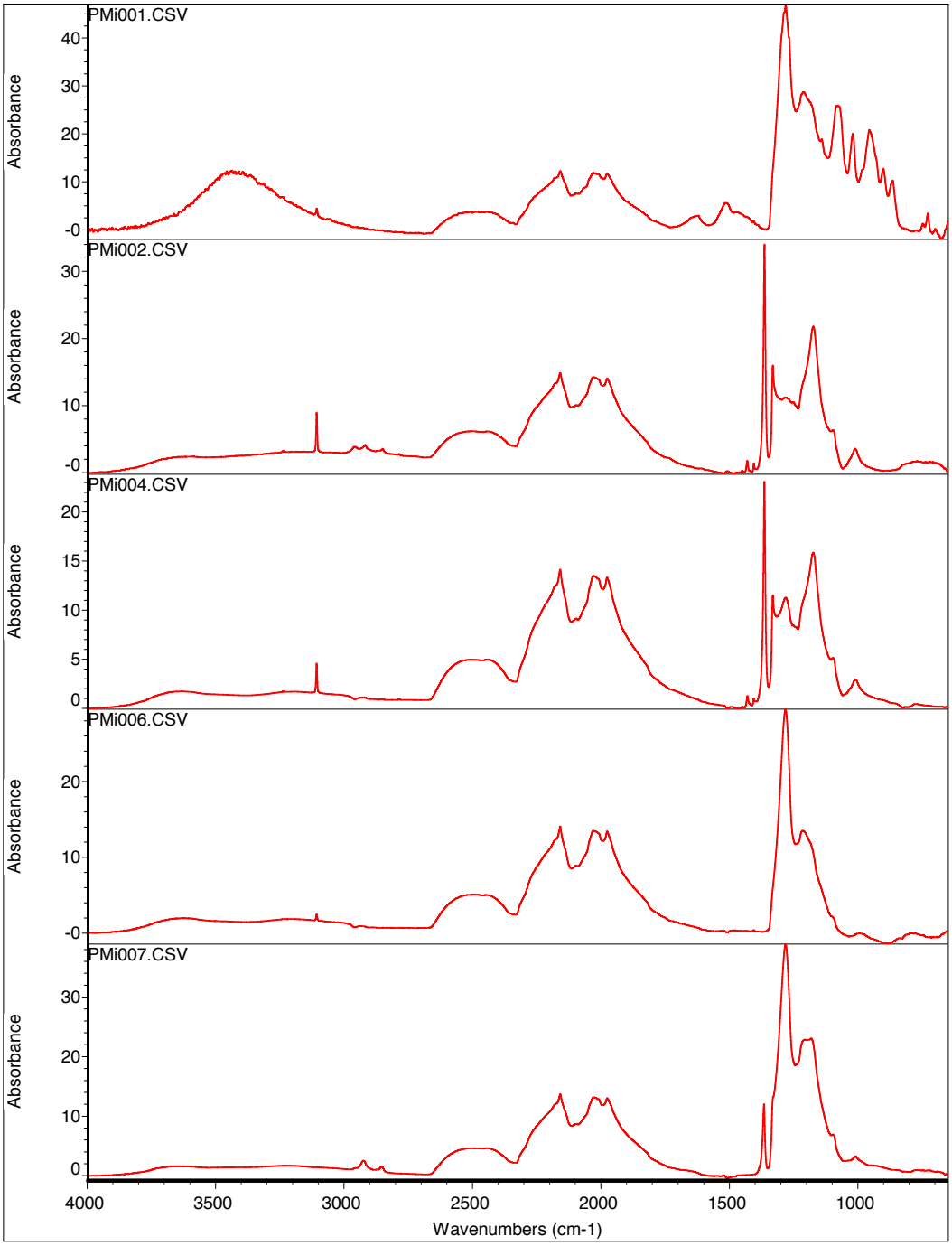

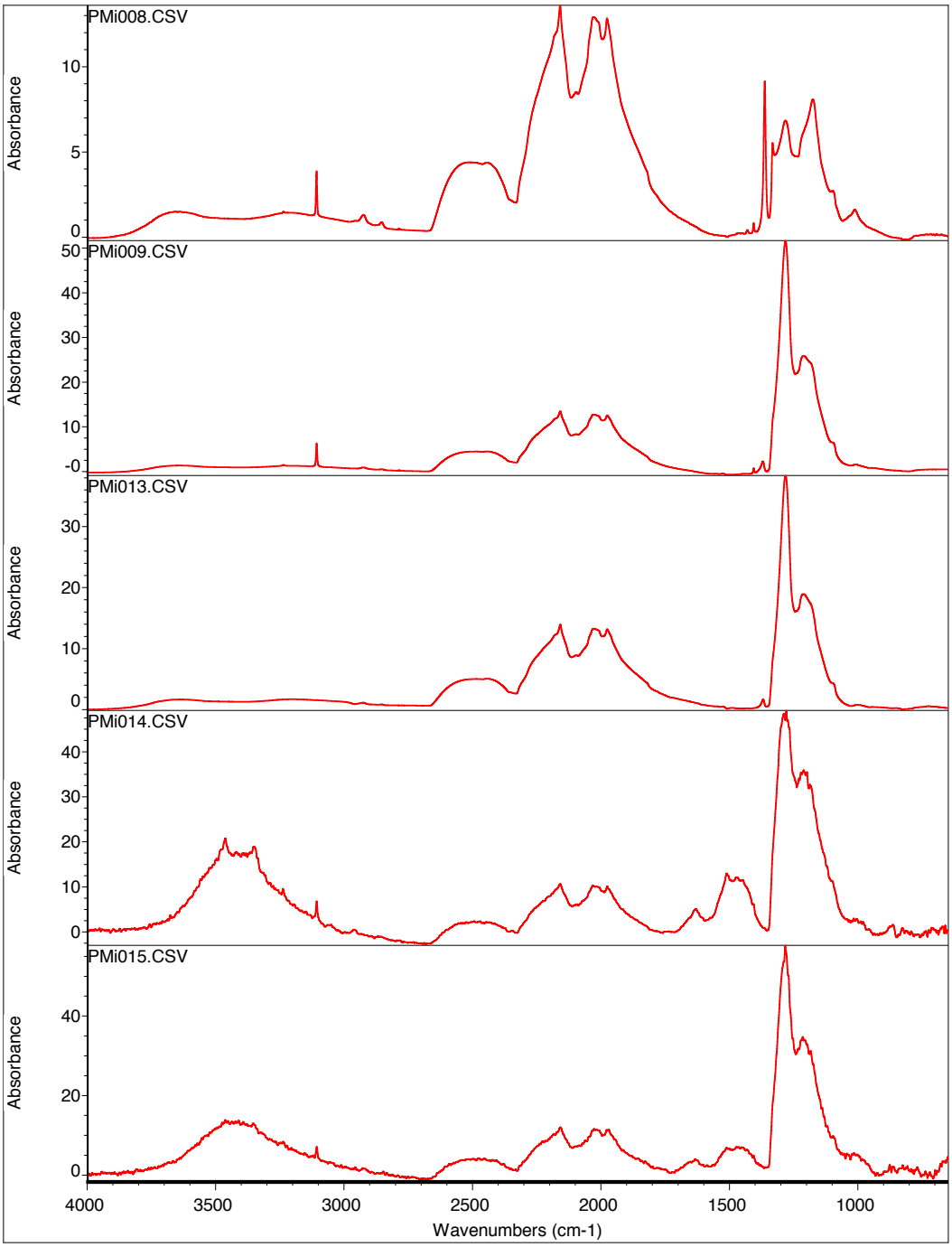
PMi008.CSV
PMi009.CSV
PMi013.CSV
PMi014.CSV
PMi015.CSV
Absorbance
Wavenumbers (cm-1)
4000
3500
3000
2500
2000
1500
1000

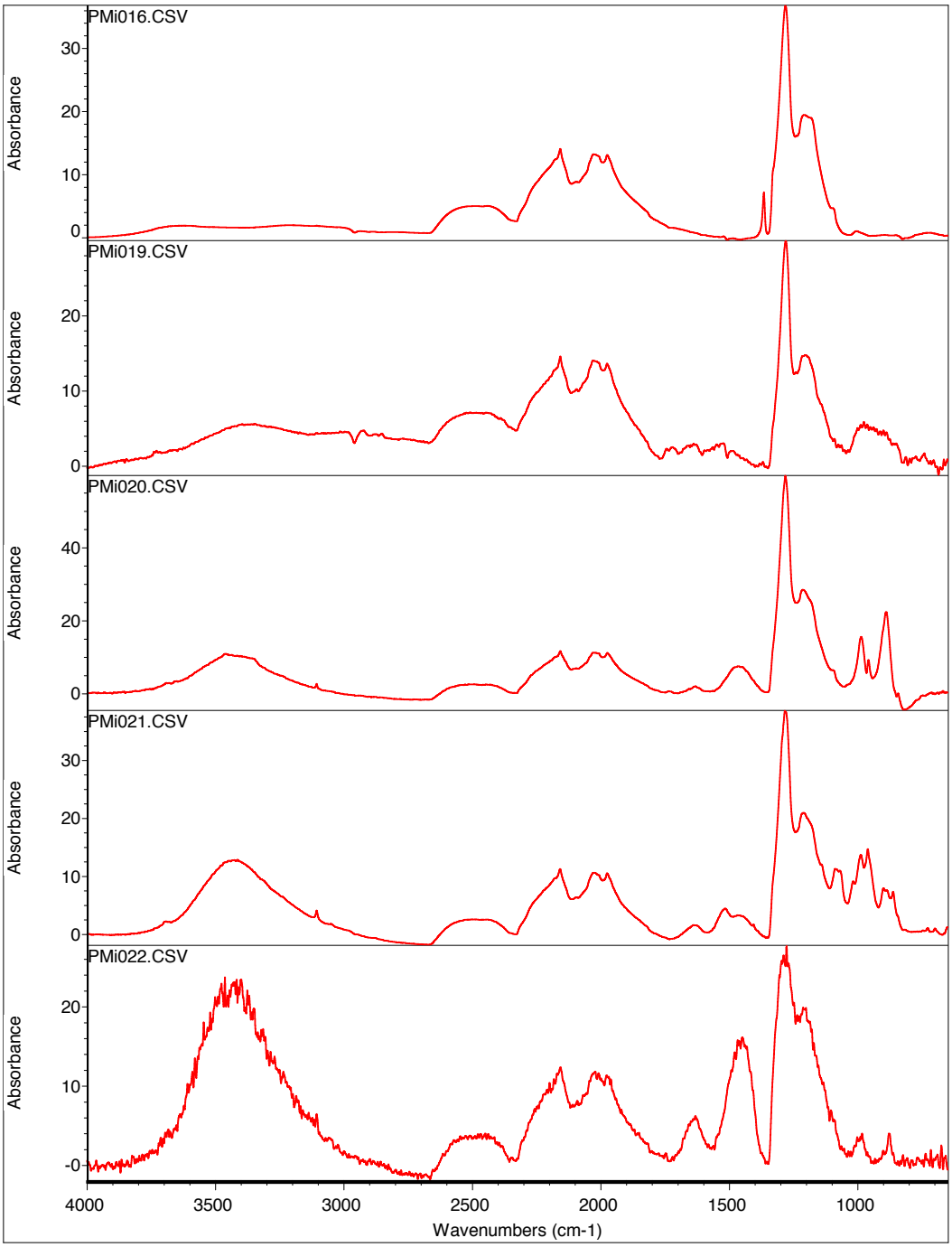
PMi016.CSV
PMi019.CSV
PMi020.CSV
PMi021.CSV
PMi022.CSV
Absorbance
Wavenumbers (cm-1)
4000
3500
3000
2500
2000
1500
1000

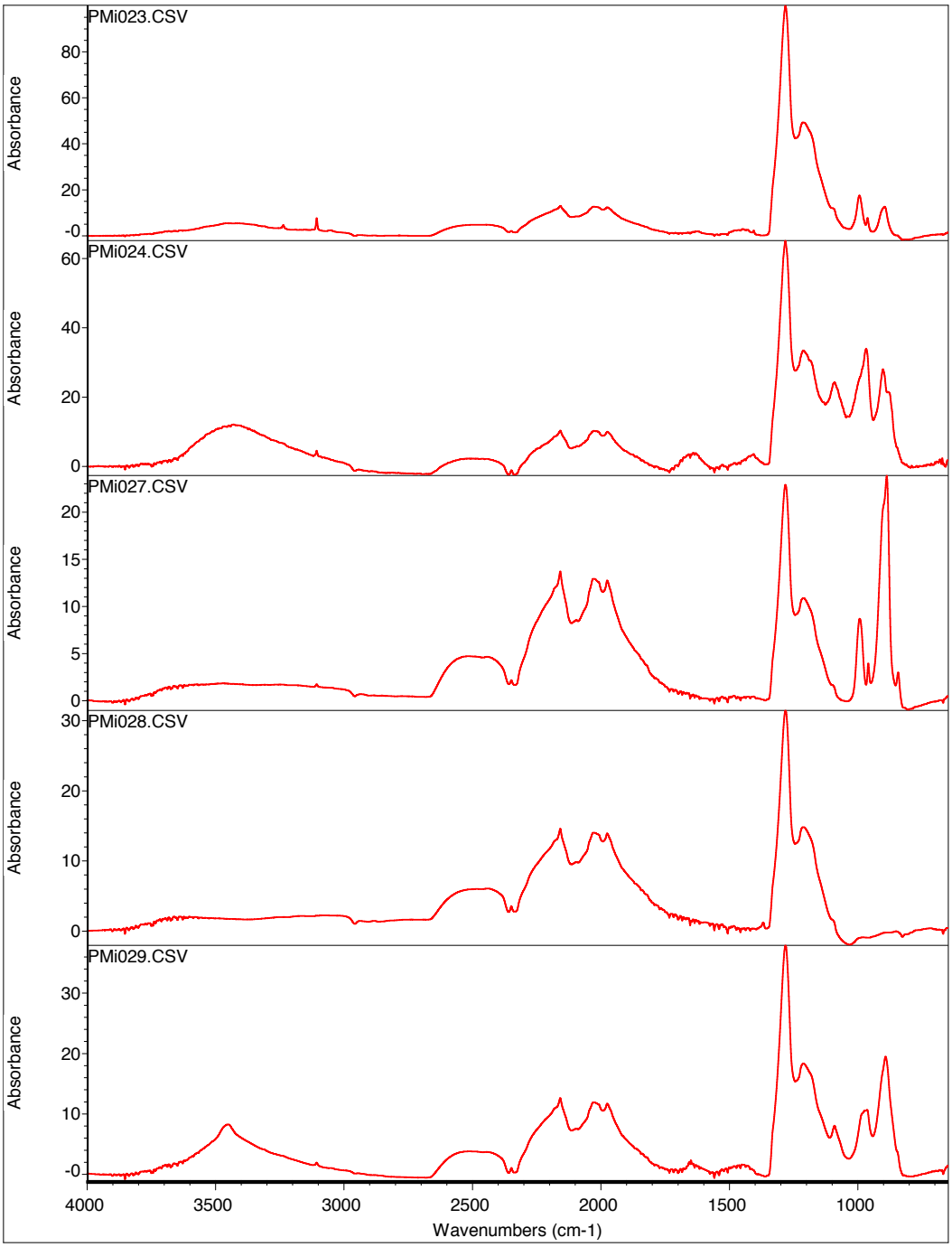
PMi023.CSV
PMi024.CSV
PMi027.CSV
PMi028.CSV
PMi029.CSV
Absorbance
Wavenumbers (cm-1)
4000
3500
3000
2500
2000
1500
1000

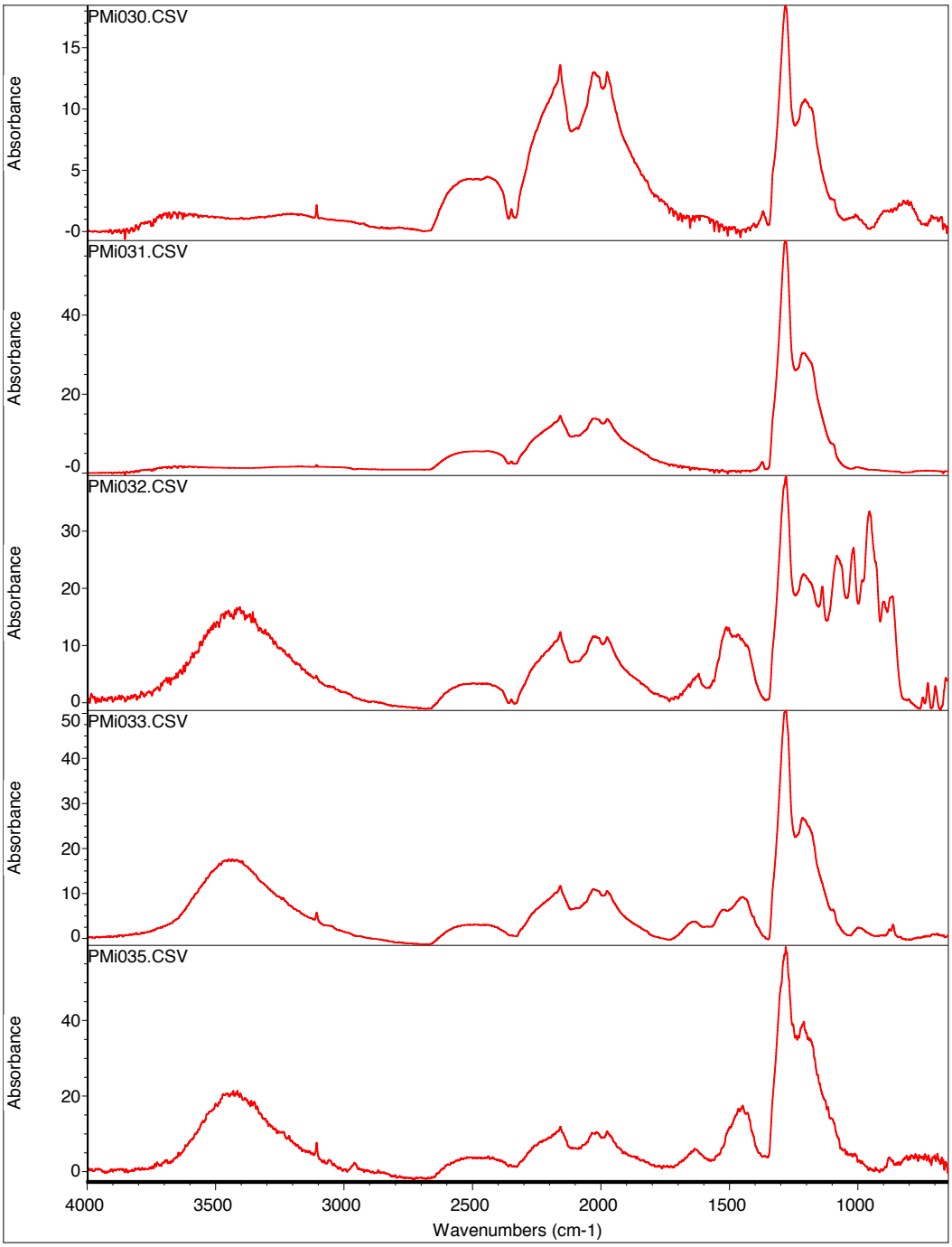
PMi030.CSV
PMi031.CSV
PMi032.CSV
PMi033.CSV
PMi035.CSV
Absorbance
Wavenumbers (cm-1)
4000
3500
3000
2500
2000
1500
1000

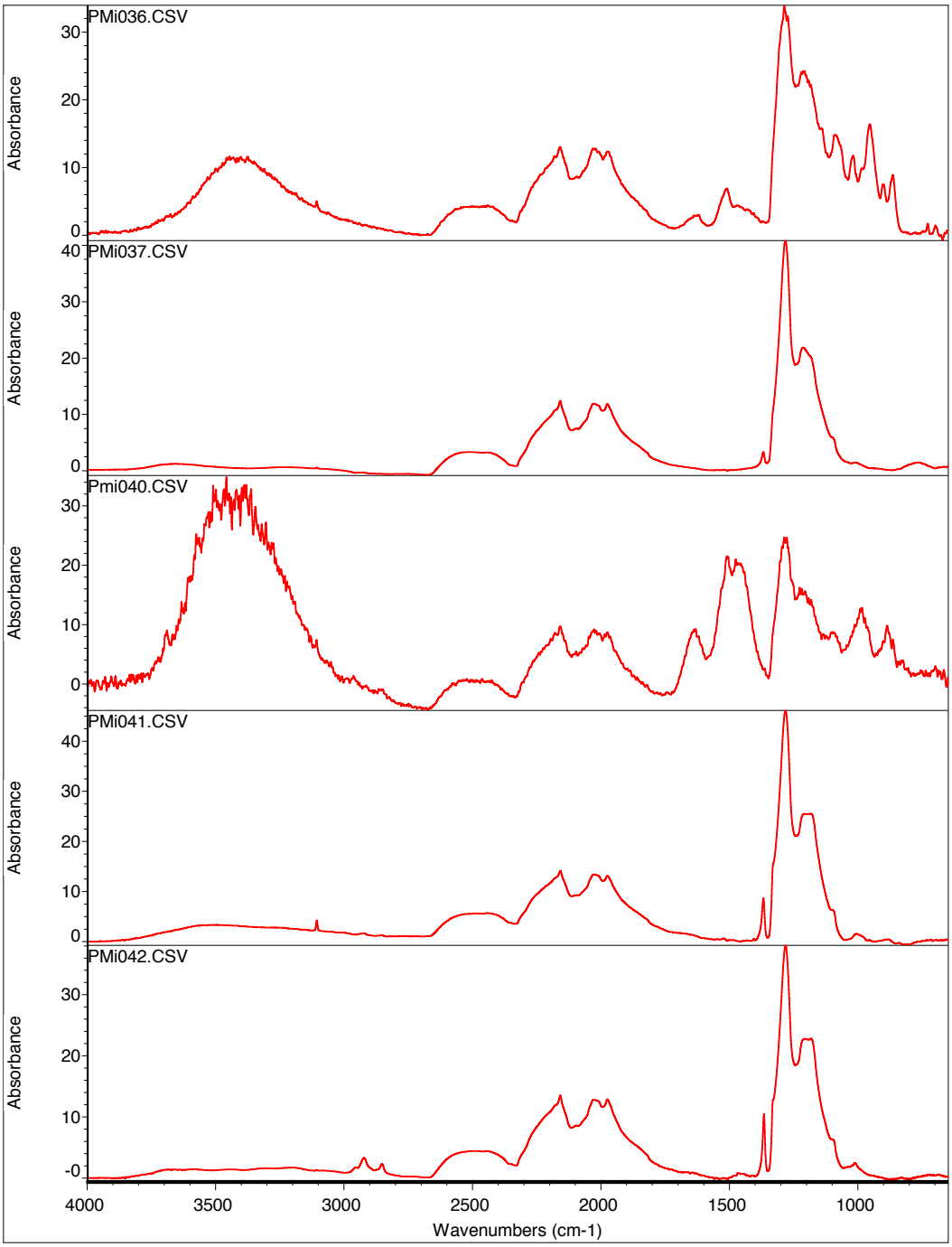
PMi036.CSV
PMi037.CSV
Pmi040.CSV
PMi041.CSV
PMi042.CSV
Absorbance
Wavenumbers (cm-1)
4000
3500
3000
2500
2000
1500
1000

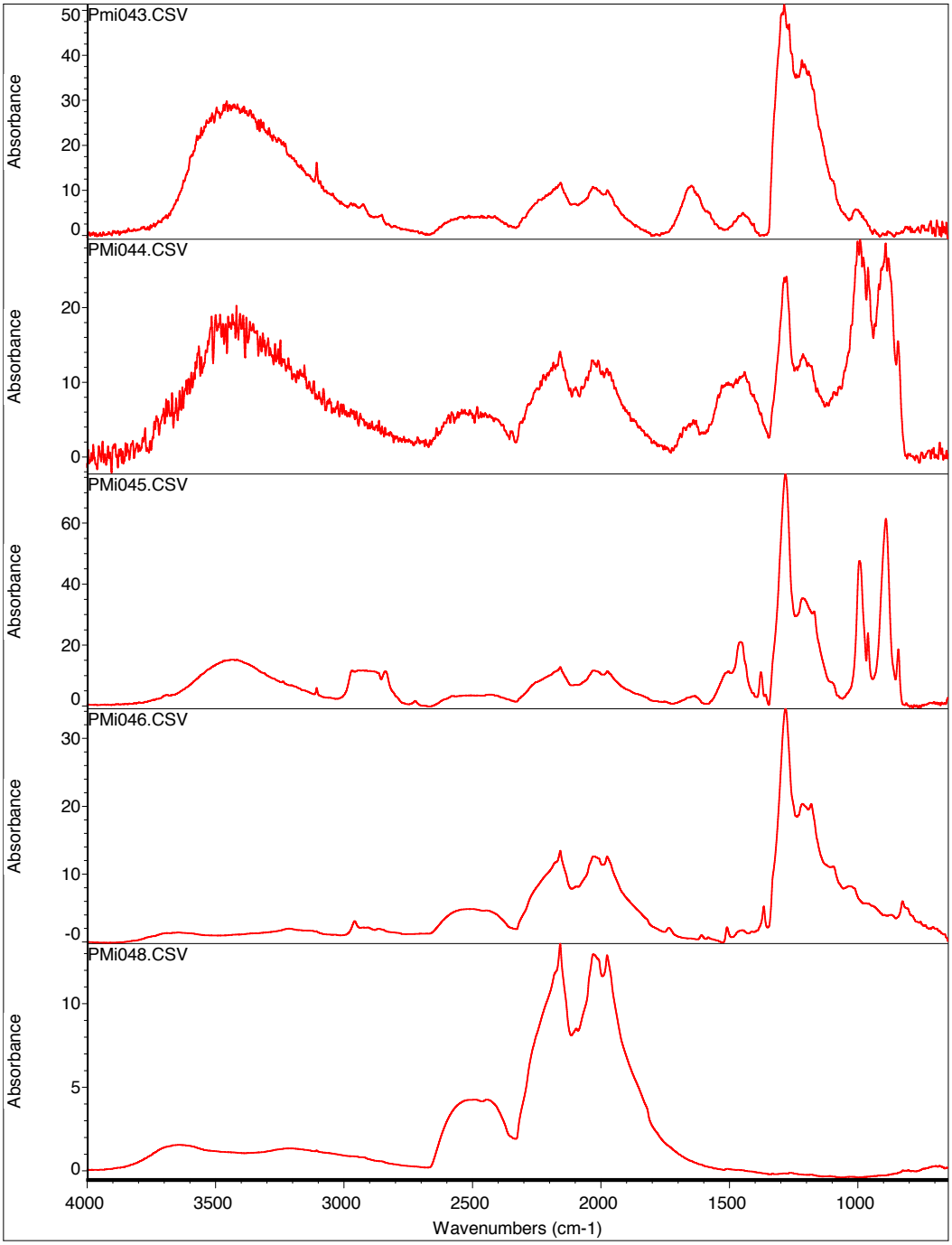
PMi043.CSV
PMi044.CSV
PMi045.CSV
PMi046.CSV
PMi048.CSV
Absorbance
Wavenumbers (cm-1)
4000
3500
3000
2500
2000
1500
1000

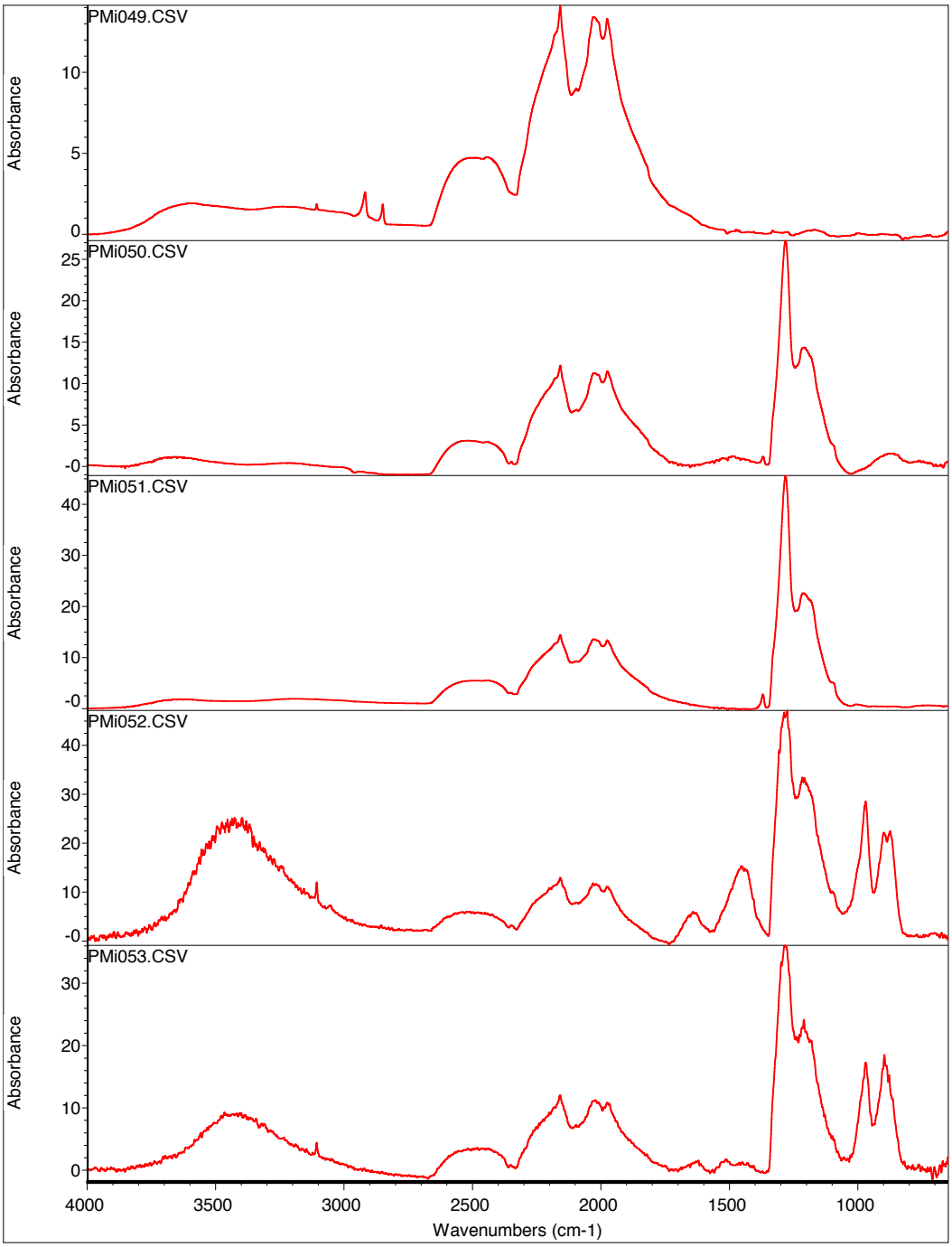
PMi049.CSV
PMi050.CSV
PMi051.CSV
PMi052.CSV
PMi053.CSV
Absorbance
Wavenumbers (cm-1)
4000
3500
3000
2500
2000
1500
1000

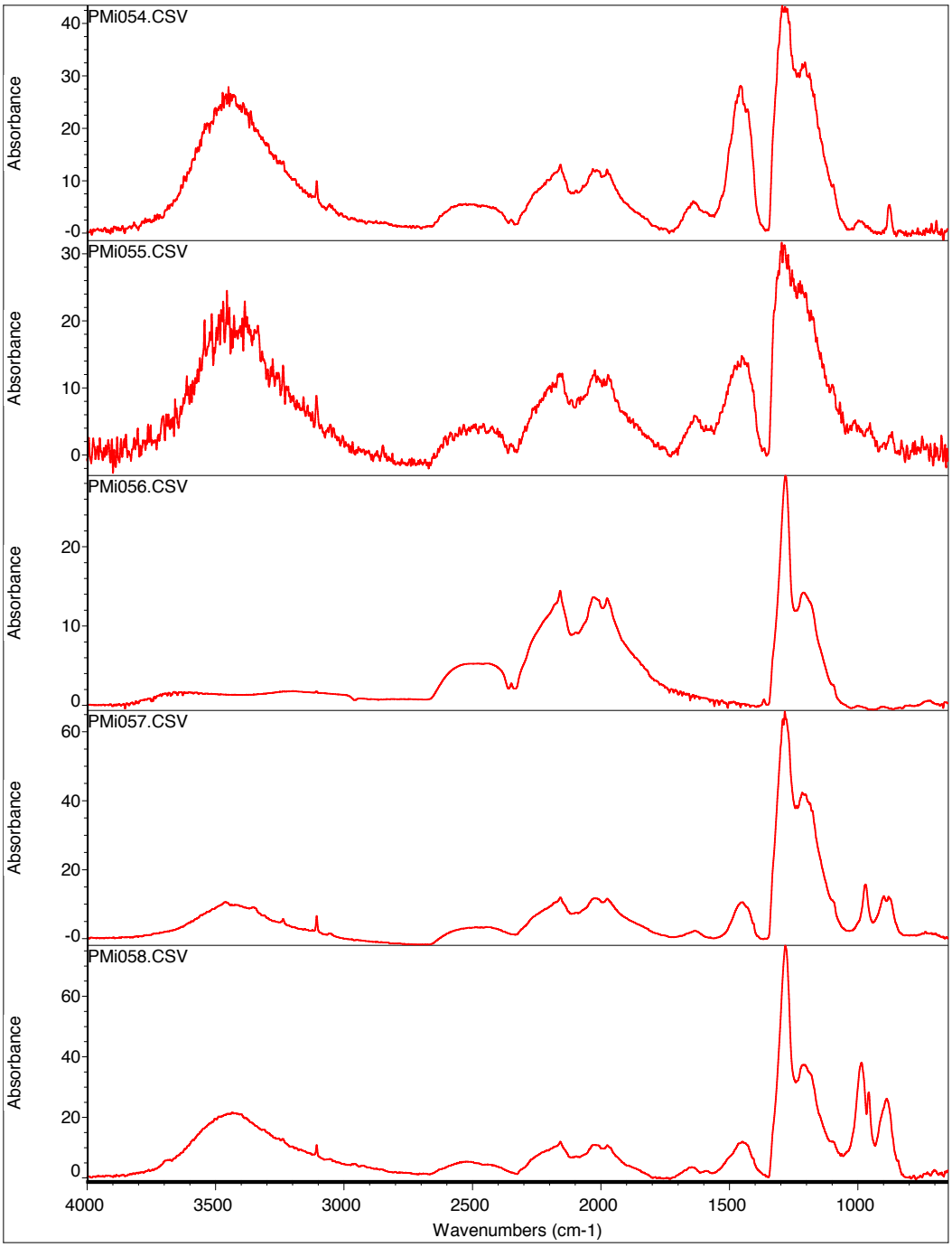
PMi054.CSV
PMi055.CSV
PMi056.CSV
PMi057.CSV
PMi058.CSV
Absorbance
Wavenumbers (cm-1)
4000
3500
3000
2500
2000
1500
1000

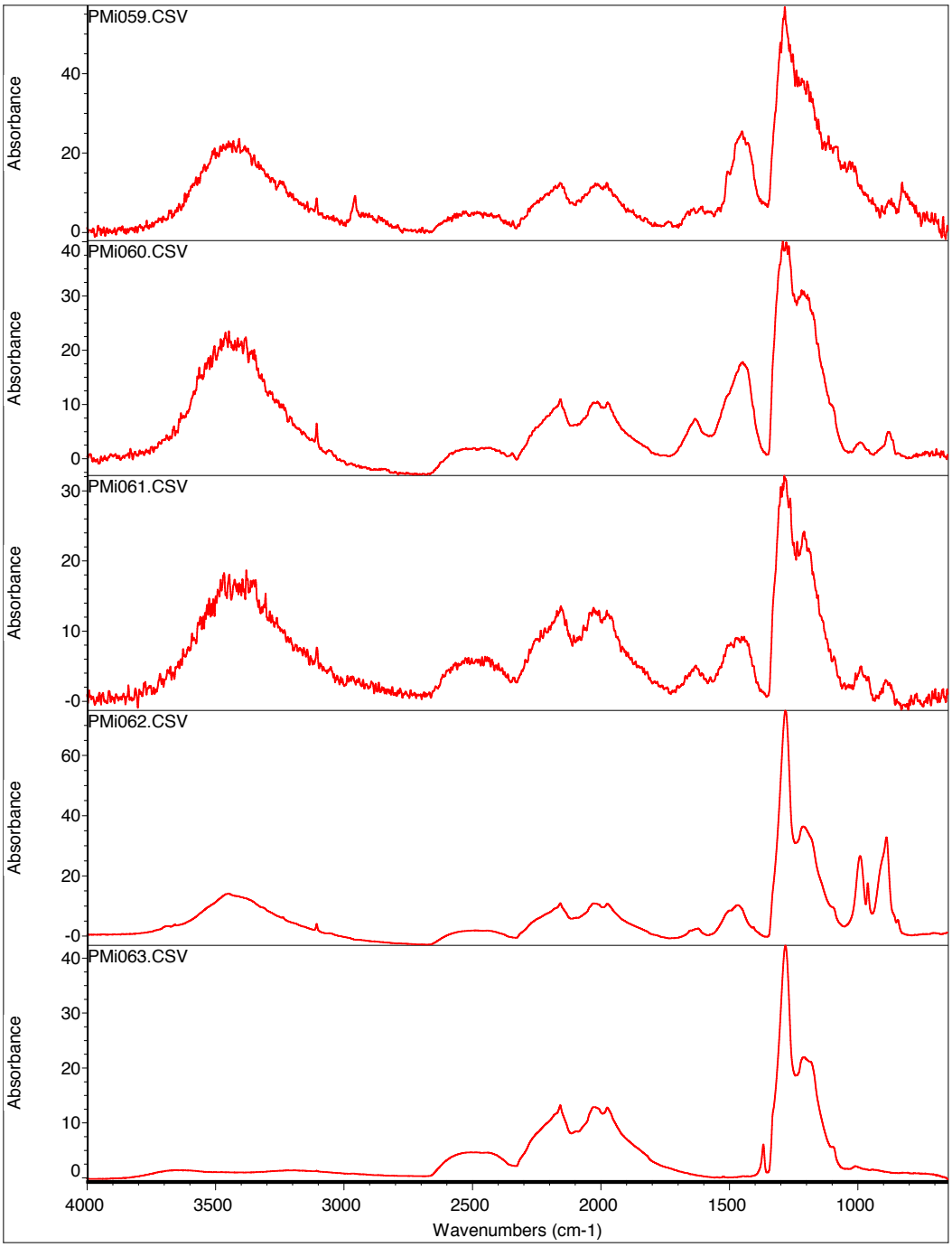
PMi059.CSV
PMi060.CSV
PMi061.CSV
PMi062.CSV
PMi063.CSV
Absorbance
Wavenumbers (cm-1)
4000
3500
3000
2500
2000
1500
1000

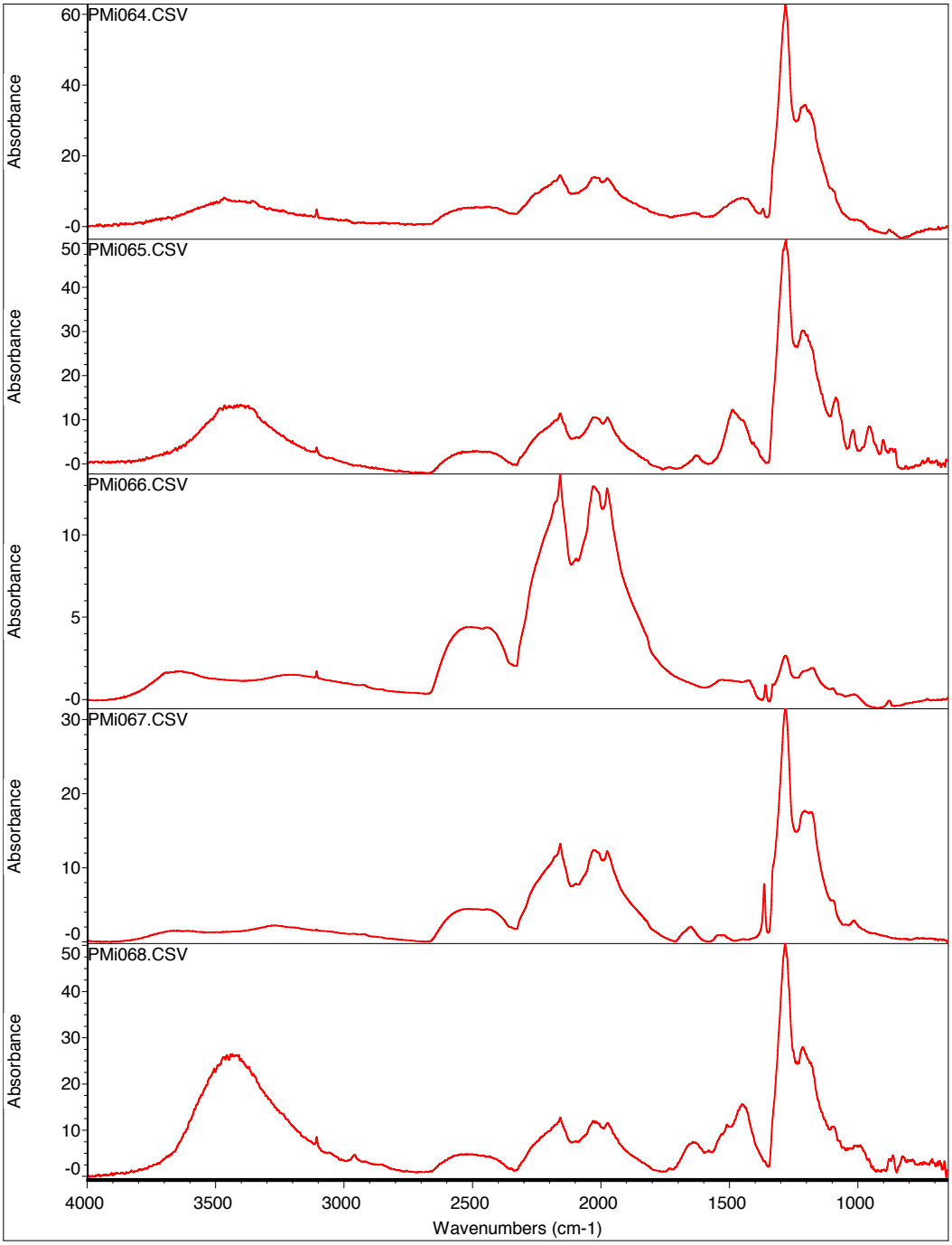
PMi064.CSV
PMi065.CSV
PMi066.CSV
PMi067.CSV
PMi068.CSV
Absorbance
Wavenumbers (cm-1)
4000
3500
3000
2500
2000
1500
1000

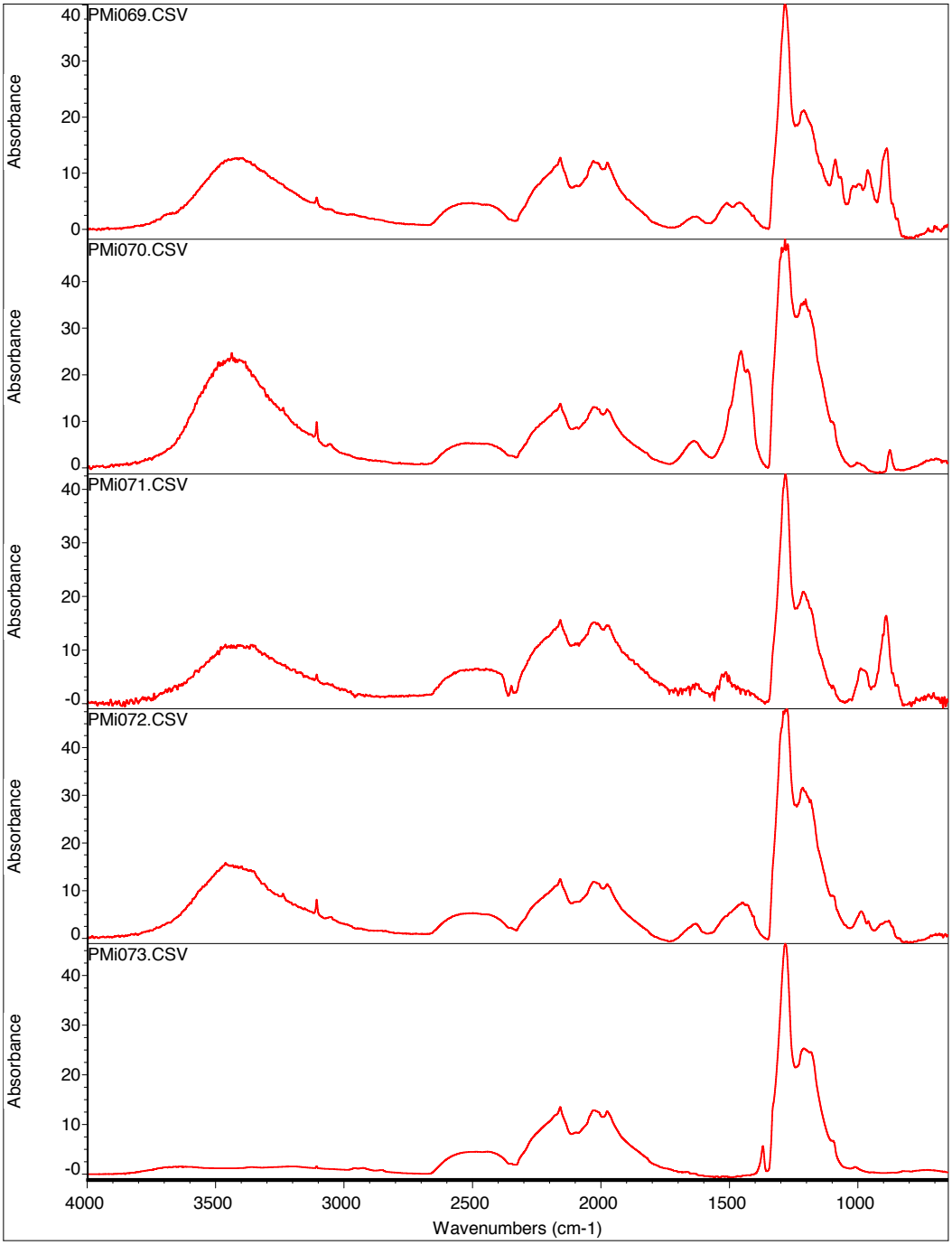
PMi069.CSV
PMi070.CSV
PMi071.CSV
PMi072.CSV
PMi073.CSV
Absorbance
40
30
20
10
0
-0
4000
3500
3000
2500
2000
1500
1000
Wavenumbers (cm-1)

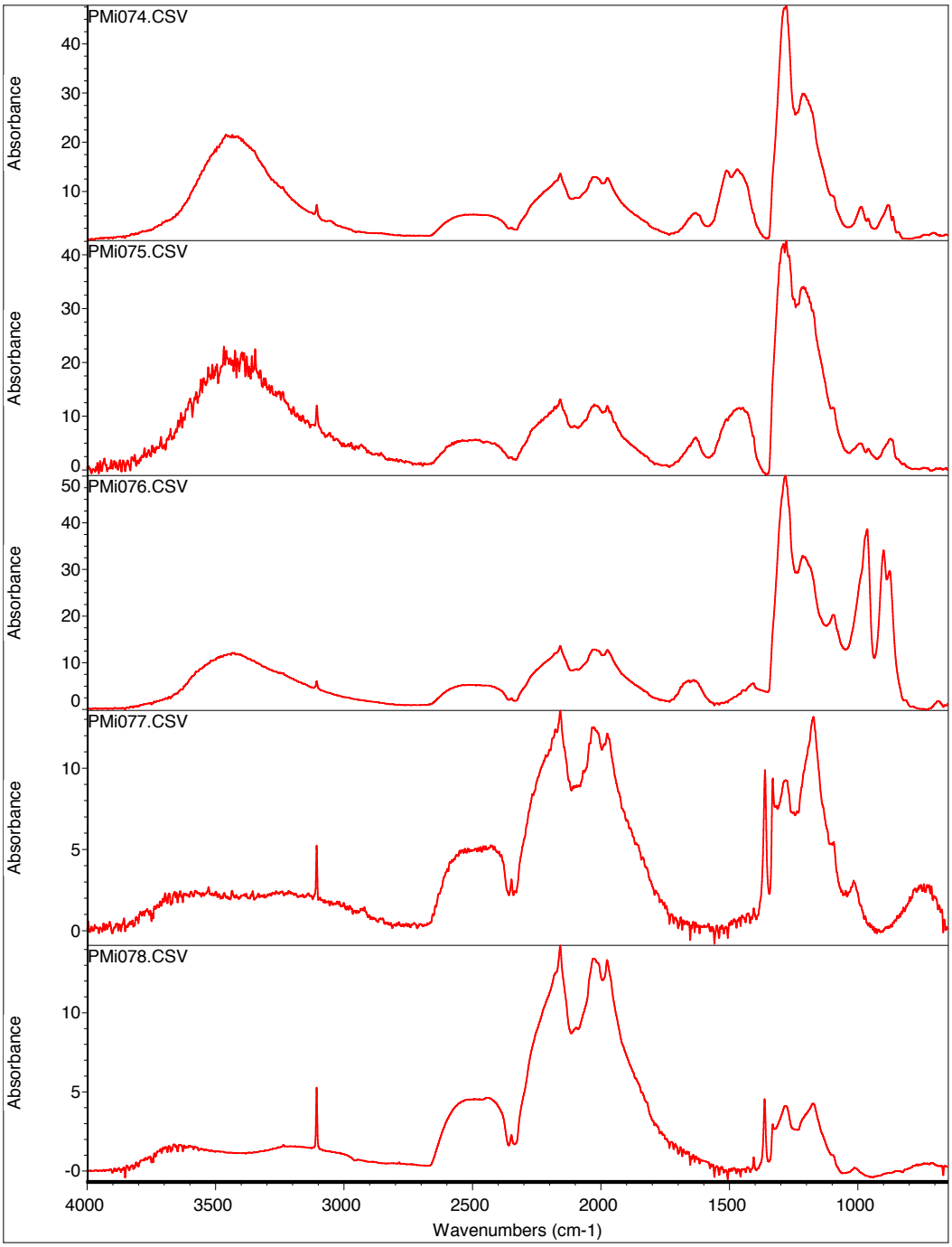
PMi074.CSV
PMi075.CSV
PMi076.CSV
PMi077.CSV
PMi078.CSV
Absorbance
Wavenumbers (cm-1)
4000
3500
3000
2500
2000
1500
1000

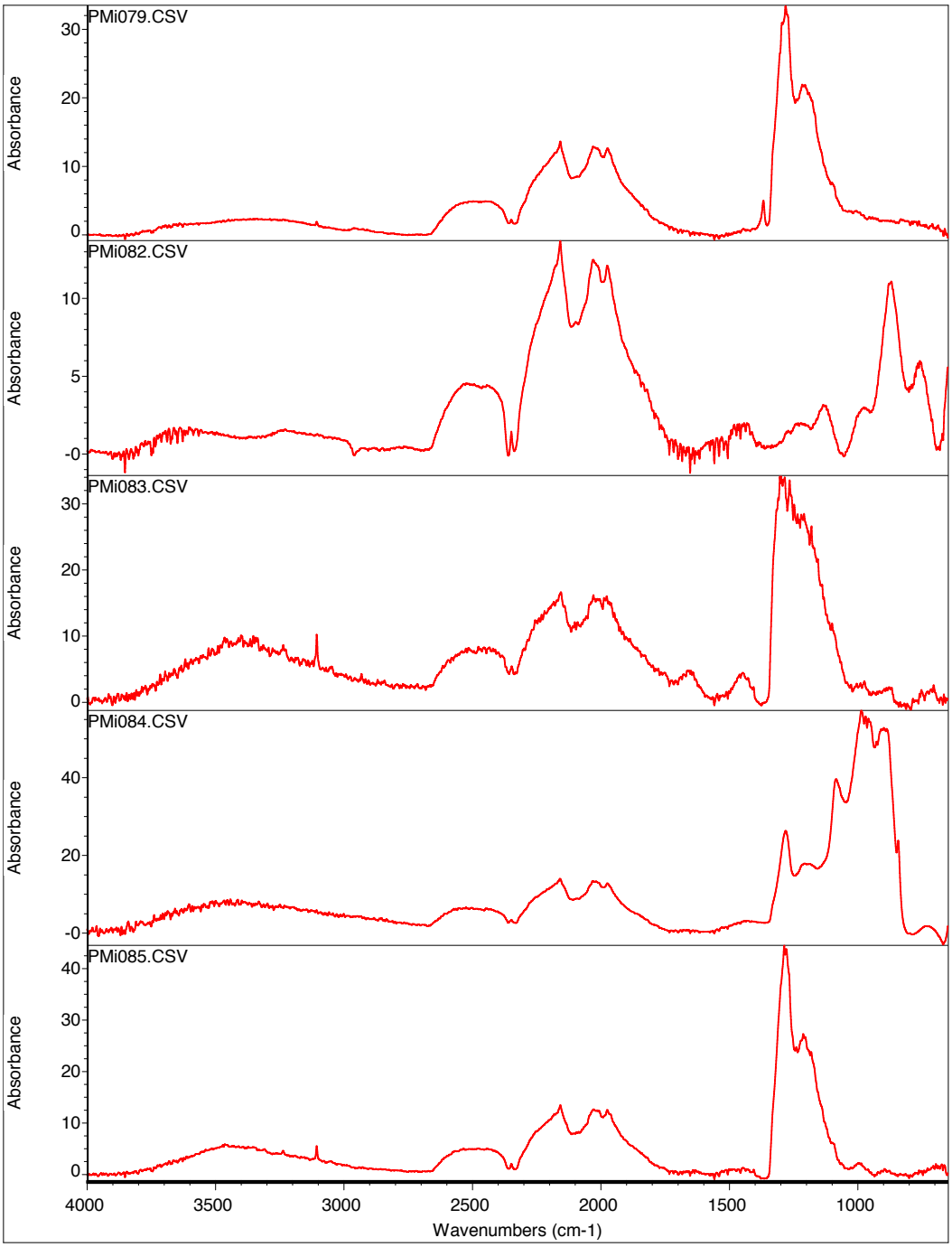
PMi079.CSV
PMi082.CSV
PMi083.CSV
PMi084.CSV
PMi085.CSV
Absorbance
Wavenumbers (cm-1)
4000
3500
3000
2500
2000
1500
1000

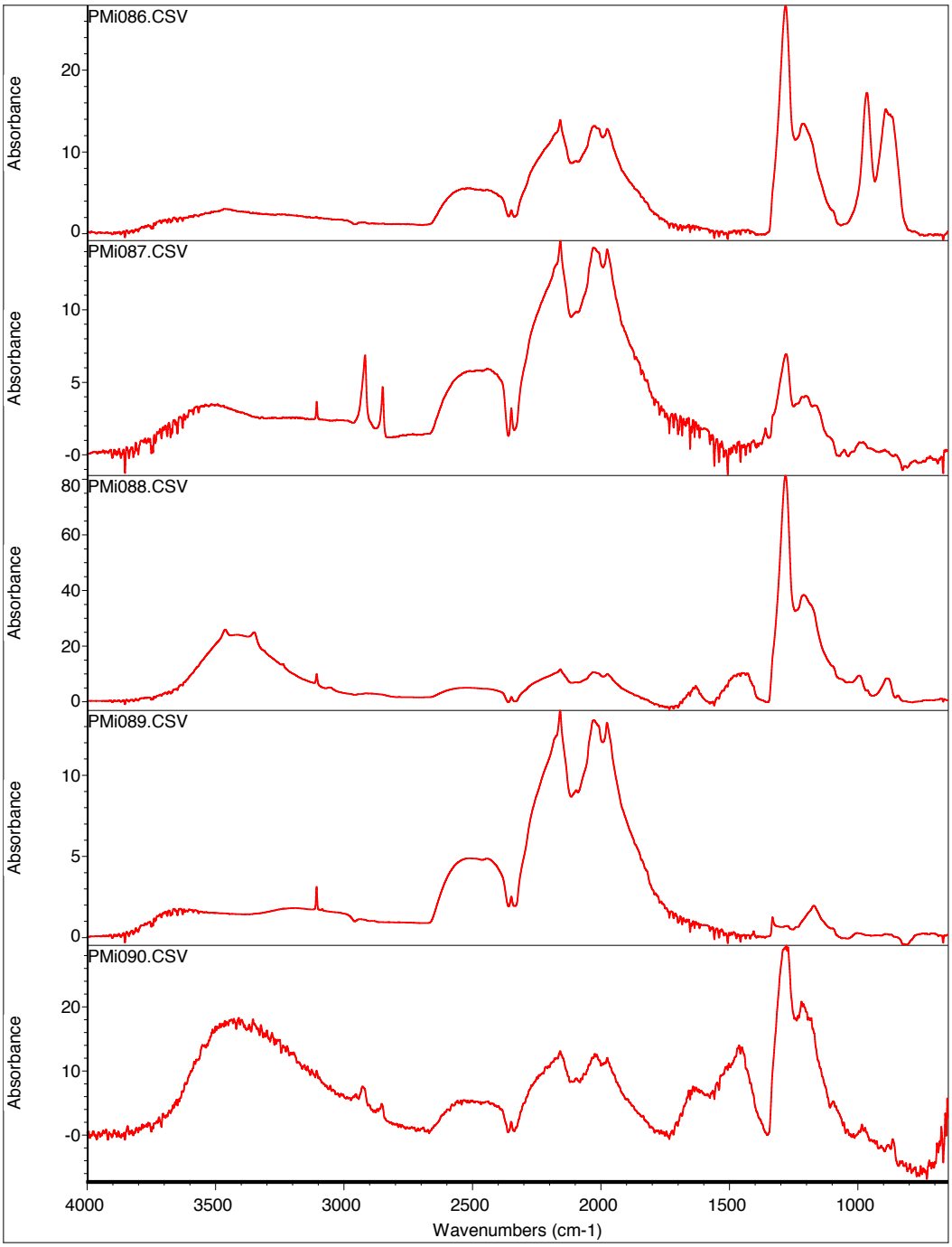
PMi086.CSV
PMi087.CSV
PMi088.CSV
PMi089.CSV
PMi090.CSV
Absorbance
Wavenumbers (cm-1)
4000
3500
3000
2500
2000
1500
1000

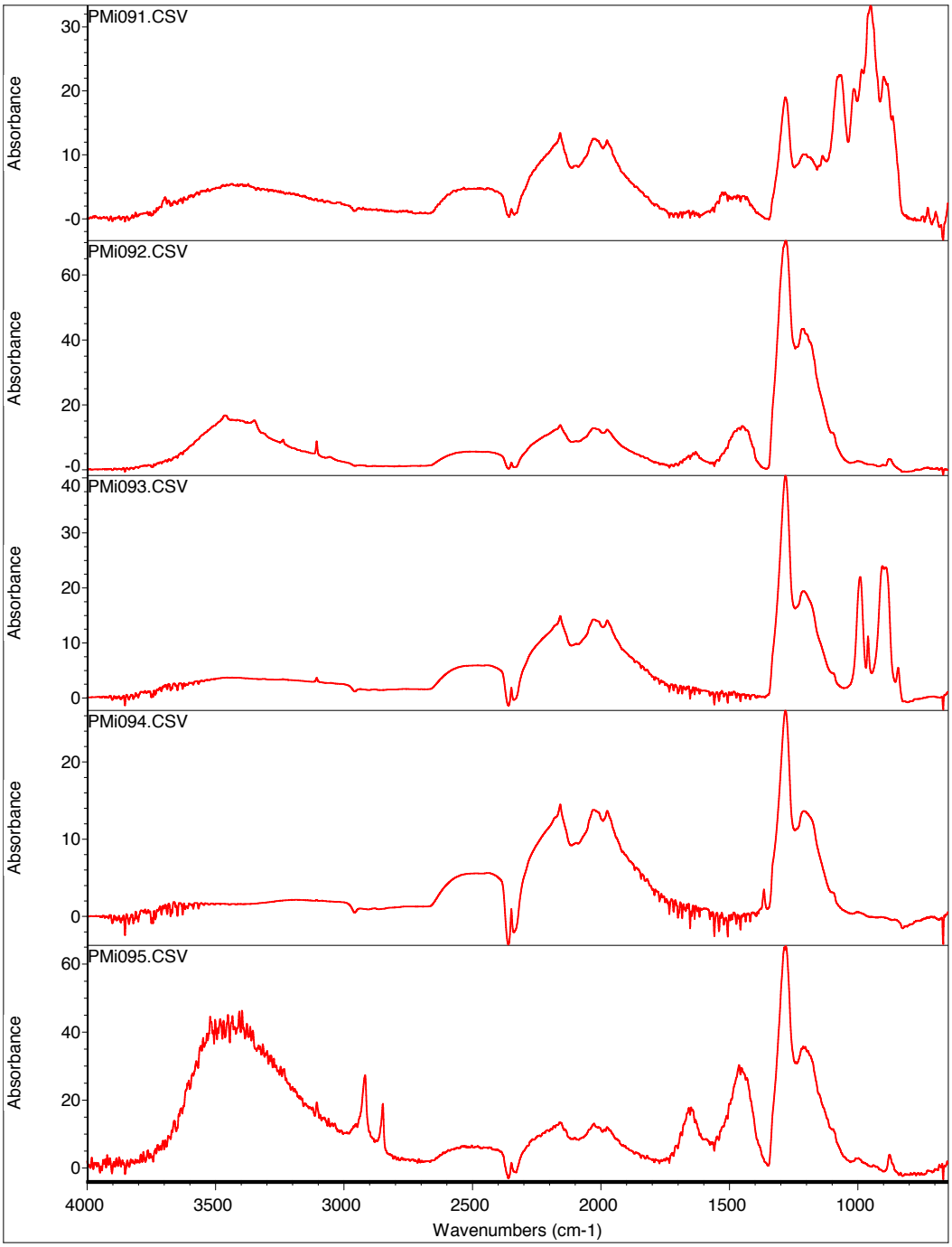
PMi091.CSV
PMi092.CSV
PMi093.CSV
PMi094.CSV
PMi095.CSV
Absorbance
Wavenumbers (cm-1)
4000
3500
3000
2500
2000
1500
1000

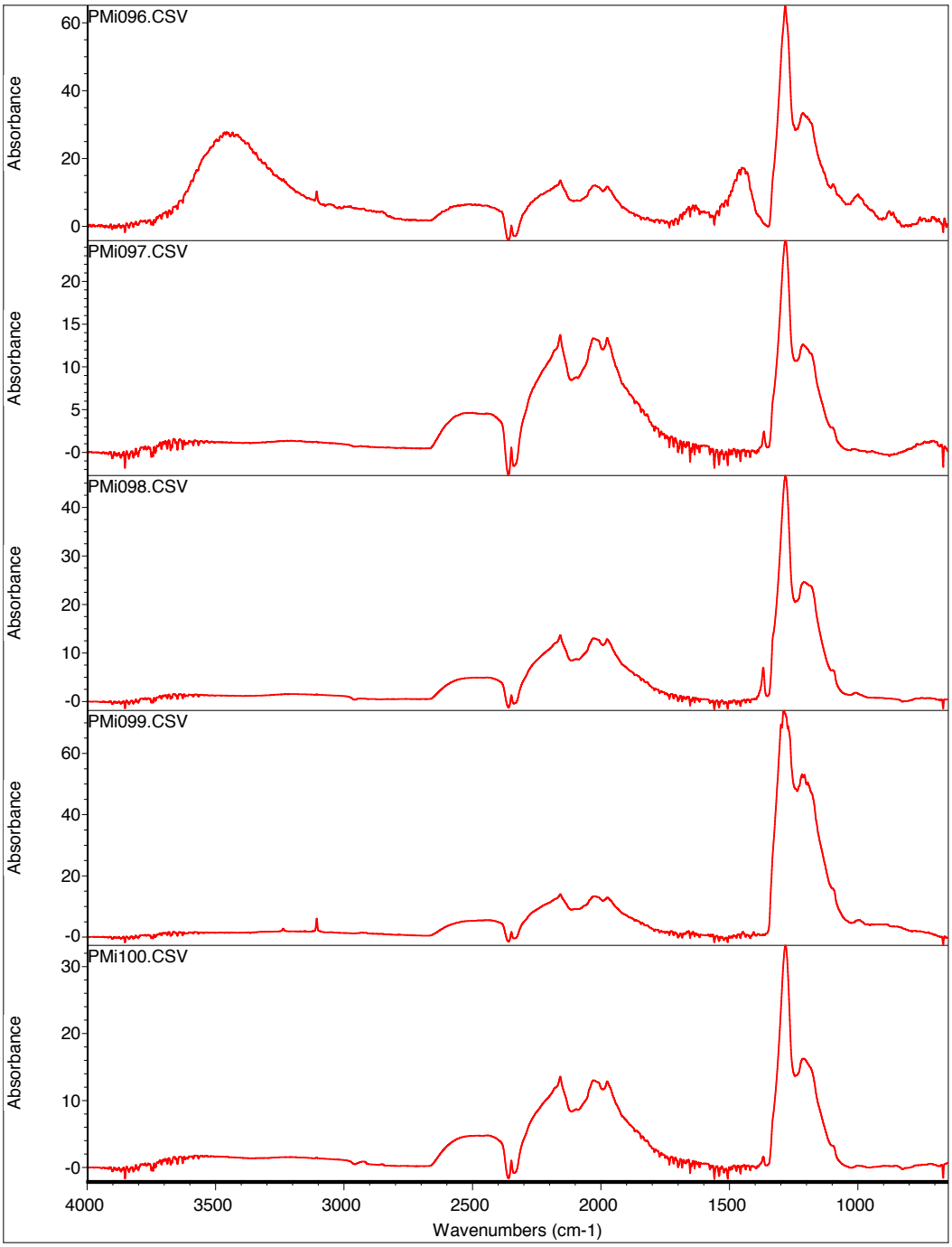
PMi096.CSV
PMi097.CSV
PMi098.CSV
PMi099.CSV
PMi100.CSV
Absorbance
Wavenumbers (cm-1)
4000
3500
3000
2500
2000
1500
1000

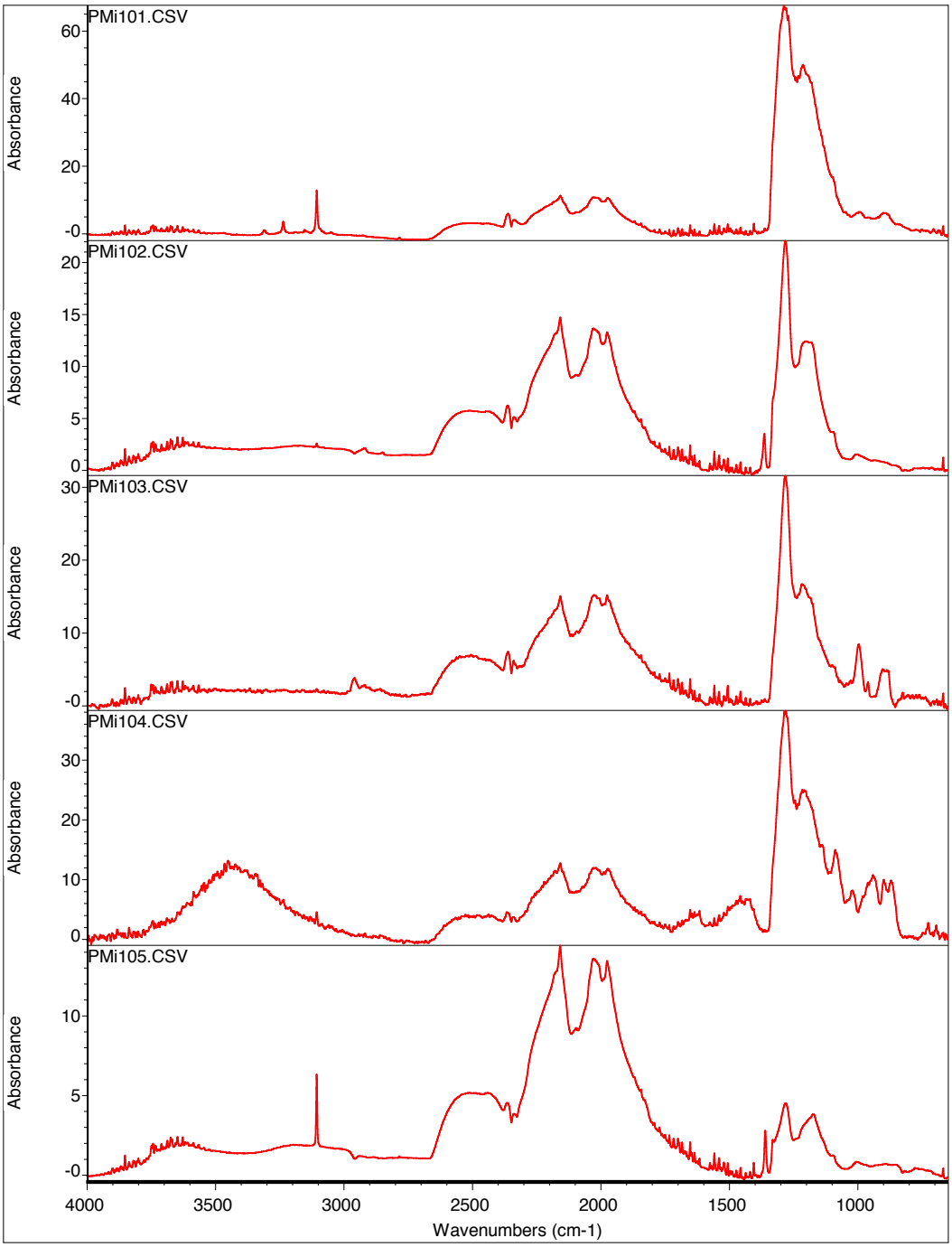
PMi101.CSV
PMi102.CSV
PMi103.CSV
PMi104.CSV
PMi105.CSV
Absorbance
Wavenumbers (cm-1)
4000
3500
3000
2500
2000
1500
1000

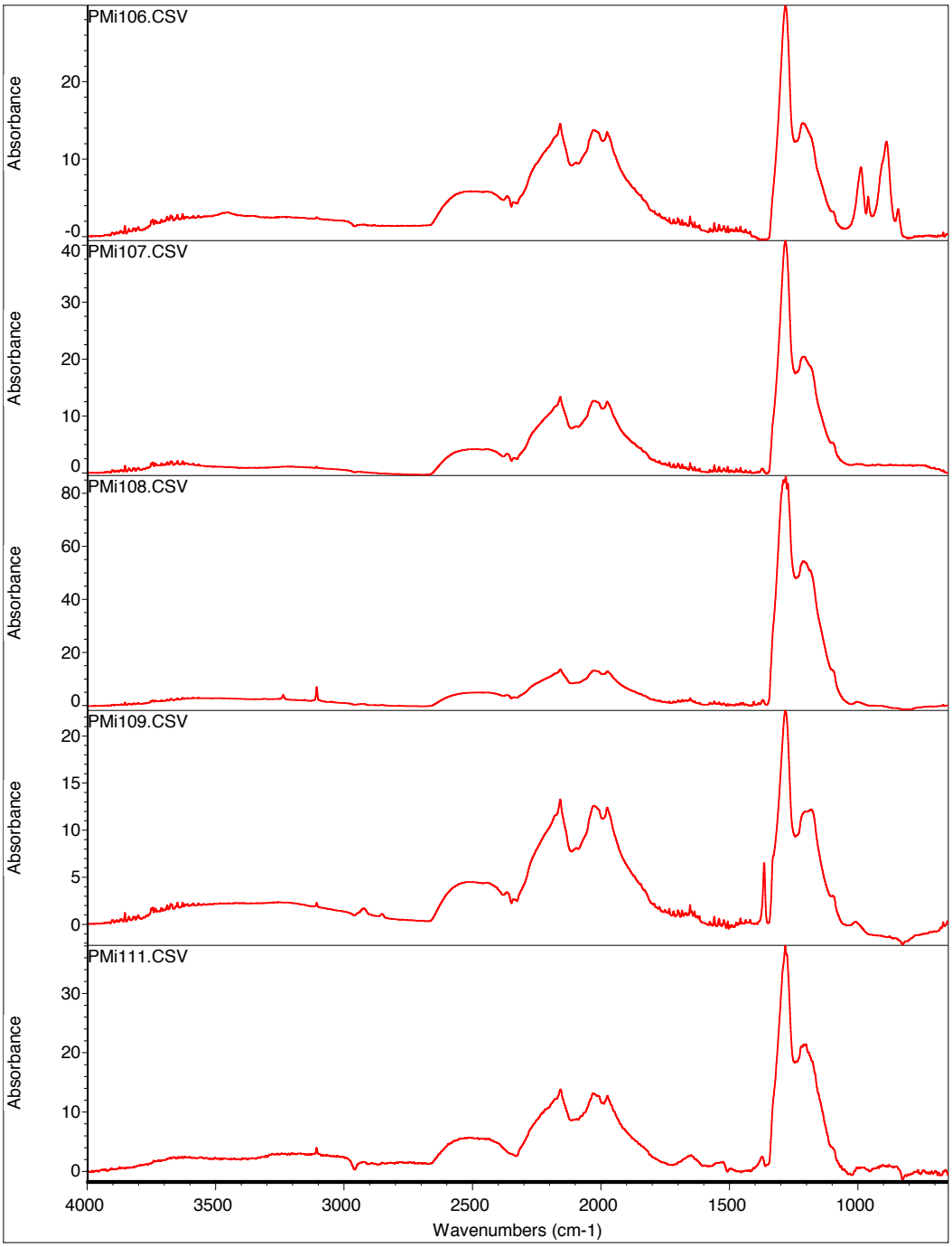
PMi106.CSV
PMi107.CSV
PMi108.CSV
PMi109.CSV
PMi111.CSV
Absorbance
Wavenumbers (cm-1)
4000
3500
3000
2500
2000
1500
1000

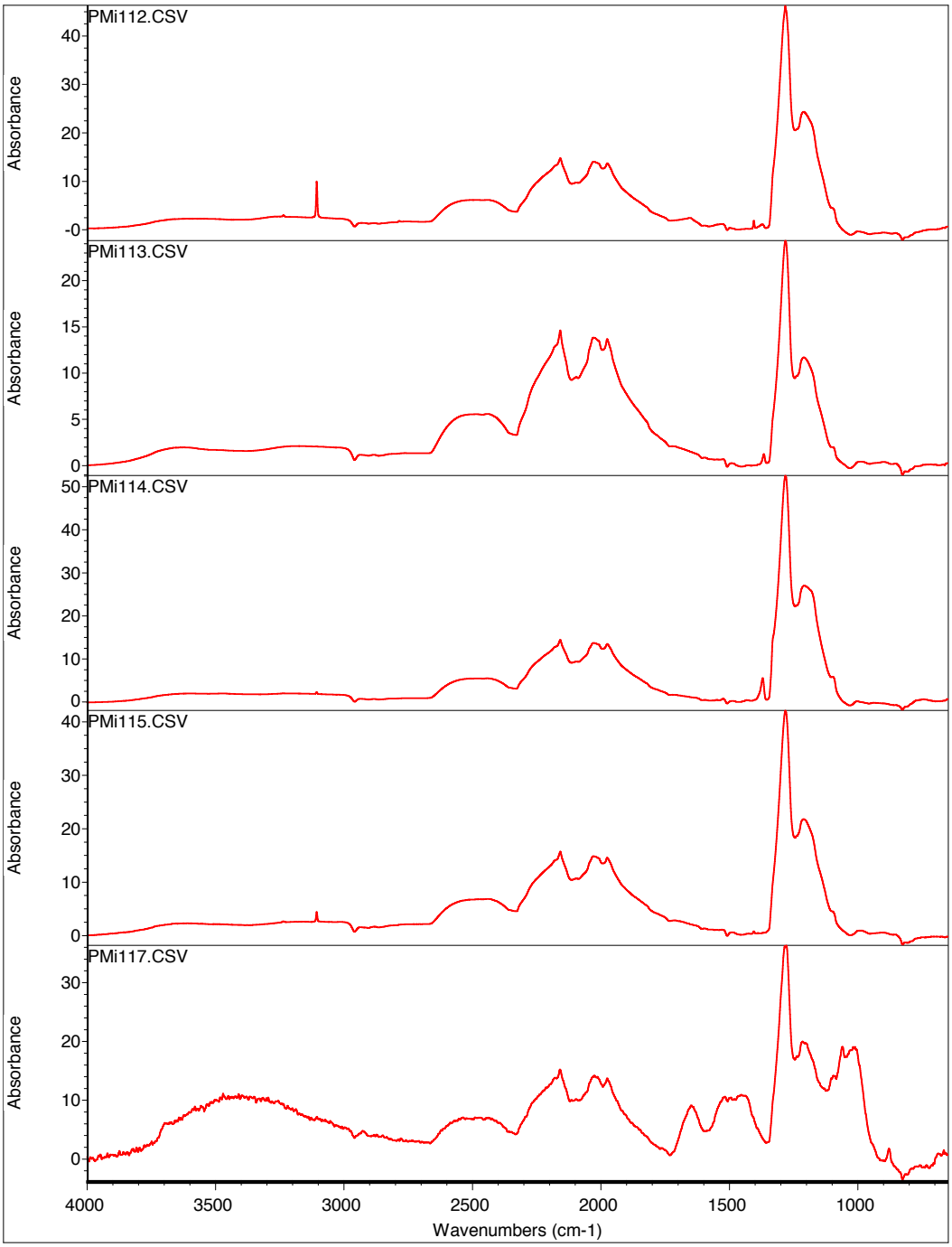
PMi112.CSV
PMi113.CSV
PMi114.CSV
PMi115.CSV
PMi117.CSV
Absorbance
Wavenumbers (cm-1)
4000
3500
3000
2500
2000
1500
1000

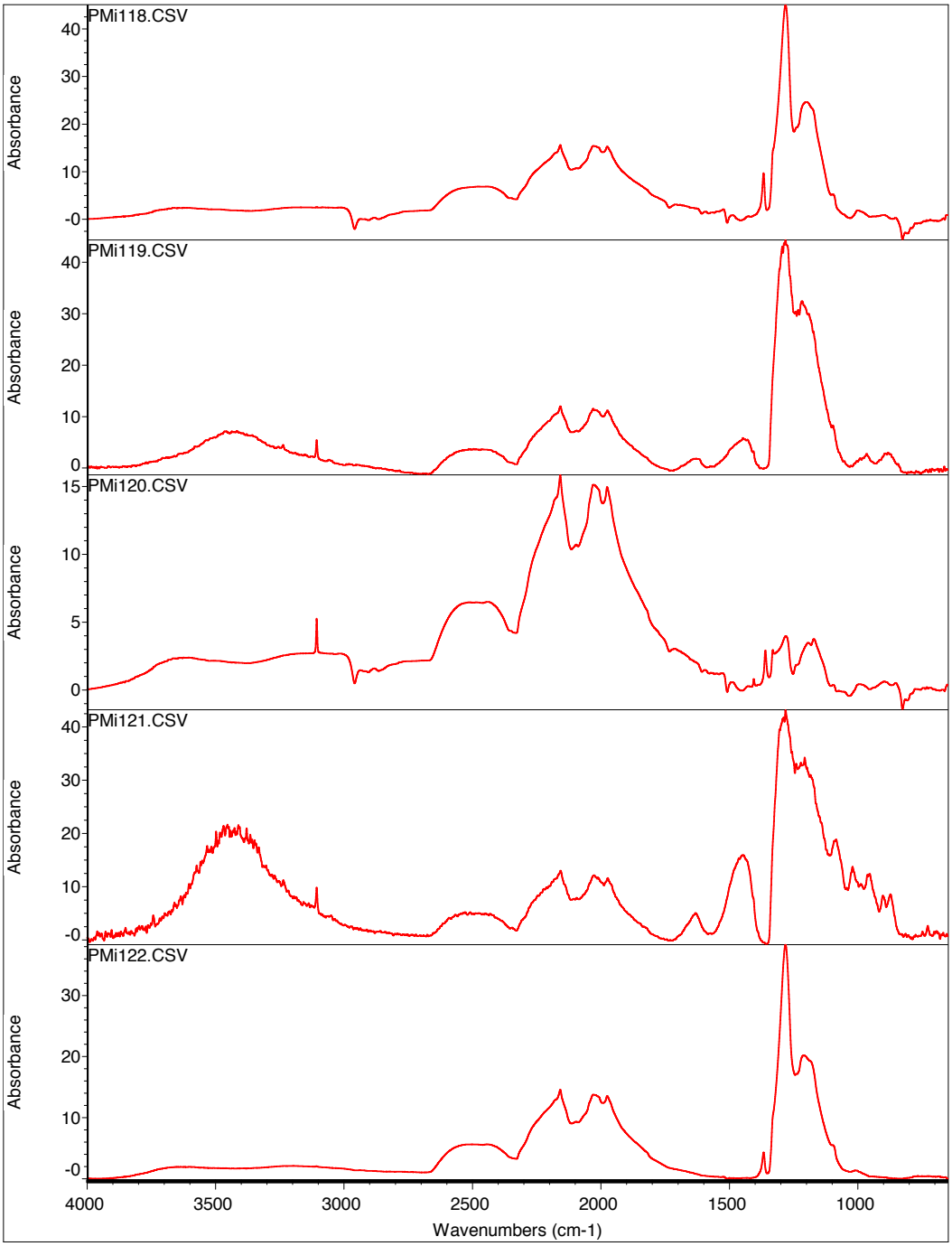
PMi118.CSV
PMi119.CSV
PMi120.CSV
PMi121.CSV
PMi122.CSV
Absorbance
Wavenumbers (cm-1)
4000
3500
3000
2500
2000
1500
1000

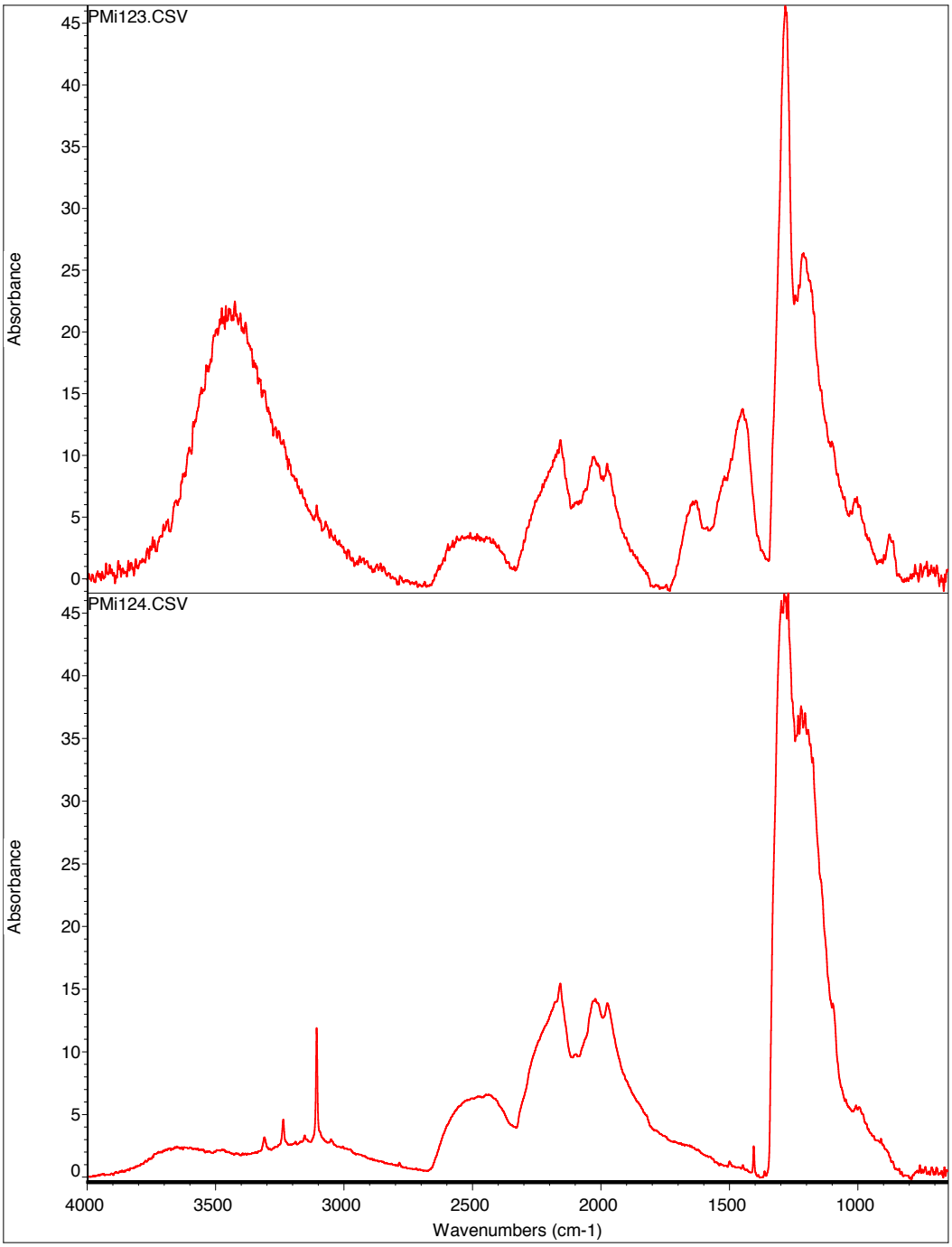
PMi123.CSV
PMi124.CSV
Absorbance
Absorbance
45
40
35
30
25
20
15
10
5
0
4000
3500
3000
2500
2000
1500
1000
Wavenumbers (cm-1)

Appendix B: FTIR database

The following tables contain results of reprocessed FTIR data (shaded columns) and new data for samples from DeBeers Pool, South Africa and Akwatia, Gahna. Paragenesis: p = peridotitic, l = lherzolitic, h = harzburgitic, e = eclogitic, w = websteritic, deep-e = majoritic eclogitic garnet inclusions, deep-h = majoritic harzburgitic garnet inclusions, lm = lower mantle. Shape: a = aggregate, d = dodecahedron, c = cube, m = macle, f = flattened, i = irregular and o = octahedra. Color: b = brown, c = colorless, g = green, l/b = light brown, p = pink, t/g = transparent/green and y = yellow. Type is based on the amount of aggregated nitrogen: N_B < 10% = IaA, 10% ≤ N_B ≤ 90% = IaAB and N_B > 90% = IaB.

Literature sources for the data:

Location	Reference
Brazil: Arenapolis, Boa Vista, Canastra	Tappert, R., Stachel, T., Harris, J.W., Muehlenbachs, K., Brey, G.P., 2006. Placer Diamonds from Brazil: Indicators of the Composition of the Earth's Mantle and the Distance to Their Kimberlitic Sources. Economic Geology 101, 453–470.
Botswana: Damtshaa	Deines, P., Stachel, T., Harris, J.W., 2009. Systematic regional variations in diamond carbon isotopic composition and inclusion chemistry beneath the Orapa kimberlite cluster, in Botswana. Lithos 112, Supplement 2, 776–784.
Canada: Diavik	Donnelly, C.L., Stachel, T., Creighton, S., Muehlenbachs, K., Whiteford, S., 2007. Diamonds and their mineral inclusions from the A154 South pipe, Diavik Diamond Mine, Northwest territories, Canada. Lithos 98, 160–176.
Canada: Panda	Cartigny, P., Farquhar, J., Thomassot, E., Harris, J.W., Wing, B., Masterson, A., McKeegan, K., Stachel, T., 2009. A mantle origin for Paleoarchean peridotitic diamonds from the Panda kimberlite, Slave Craton: Evidence from 13C-, 15N- and 33,34S-stable isotope systematics. Lithos 112, 852–864. Tappert, R., Stachel, T., Harris, J.W., Shimizu, N., Brey, G.P., 2005. Mineral inclusions in diamonds from the Panda kimberlite, Slave Province, Canada. Eur J Mineral 17, 423–440.
Canada: Renard	Hunt, L., Stachel, T., McCandless, T.E., Armstrong, J., Muelenbachs, K., 2012. Diamonds and their mineral inclusions from the Renard kimberlites in Quebec. Lithos 142–143, 267–284.
Canada: Wawa	Stachel, T., Banas, A., Muehlenbachs, K., Kurszlaukis, S., Walker, E., 2006. Archean diamonds from Wawa (Canada): samples from deep cratonic roots predating cratonization of the Superior Province. Contributions to Mineralogy

Sample	location	paragenesis	shape	colour	deformation	$\delta^{13}C$	N (at. ppm)	N_B (at. ppm)	%IaB	N_A	Type	H area (cm^{-2})	P area (cm^{-2})
ddmi-001	Diavik	p	d	b	n	-4.54	520	112	22	408	IaAB	0.95	57.56
ddmi-002	Diavik	e	o	b	n	0.69	23	1	5	22	IaA	0.58	
ddmi-003	Diavik	p	o	b	n	-5.46	39	0	0	39	IaA	4.59	
ddmi-004	Diavik	p	i	g	n	-4.96	451	53	12	398	IaAB		26.39
ddmi-005	Diavik	p	d	c	n	-5.30	31	11	36	20	IaAB	0.65	
ddmi-006	Diavik	p	o	c	n	-4.95	278	204	73	74	IaAB	2.19	184.43
ddmi-108	Diavik	p	i	c	n	-5.28	415	50	12	365	IaAB		
ddmi-110	Diavik	p	i	b	n	-4.80	476	22	5	455	IaA	1.20	49.34
ddmi-111	Diavik	p	o	c	n	-6.26	220	25	11	196	IaAB	3.52	28.47
ddmi-112	Diavik	p	o	b	y	-5.43	364	0	0	364	IaA		38.11
ddmi-114	Diavik		i	b	n	-2.93	0	0		0	II	1.21	
ddmi-115	Diavik	p	o	b	n	-5.47	79	2	2	77	IaA	0.9	
ddmi-119	Diavik	p	i	c	n	-4.93	298	0	0	298	IaA		
ddmi-120	Diavik	p	d	c	n	-4.53	644	71	11	574	IaAB	0.87	67.61
ddmi-139	Diavik	p	d/m	p	n	-6.22	420	88	21	332	IaAB	4.74	13.5
ddmi-140	Diavik	l	o	b	n	-4.59	57	4	7	53	IaA	0.75	
ddmi-141	Diavik	l	o	c	n	-5.11	57	6	11	51	IaAB	1.63	6.68
ddmi-142	Diavik	p	o	b	n	-4.58	771	237	31	534	IaAB		47.39
ddmi-144	Diavik	p	o	b	n	-4.55	367	81	22	286	IaAB		17.02
ddmi-145	Diavik	p	i	c	n	-5.20	404	148	37	256	IaAB		6.65
ddmi-147	Diavik	p	o	b	n	-5.18	161	0	0	161	IaA		
ddmi-148	Diavik	p	o	b	n	-6.12	38	3	8	35	IaA	0.75	7.84
ddmi-150	Diavik	p	d	b	n	-4.79	228	221	97	7	IaB	13.79	84.44
ddmi-151	Diavik	p	d/m	p	n	-6.33	210	14	7	197	IaA	6.5	32.73
ddmi-152	Diavik	p	d	b	n	-5.04	125	9	7	116	IaA		
ddmi-153	Diavik		i	b	n	-4.22	0	0		0	II	0.90	
ddmi-154	Diavik	h	o	b	n	-4.82	114	74	65	40	IaAB	7.31	35.97
ddmi-155	Diavik	p	o	b	n	-5.26	433	91	21	343	IaAB	31.7	89.85
ddmi-156	Diavik	p	d	b	n	-4.90	248	12	5	236	IaA		8.82
ddmi-159	Diavik	p	d/a	g	n	-5.10	747	0	0	747	IaA	3.72	
ddmi-161	Diavik	p	o	b		-6.11	308	43	14	266	IaAB	5.53	19.34
ddmi-162	Diavik	p	o/a	c	n	-8.62	66	1	2	65	IaA	5.62	12.48
ddmi-166	Diavik	e	o	y	n	-4.77	1739	859	49	880	IaAB	3.00	479.39
ddmi-167	Diavik	h	o	b	y	-4.78	41	7	18	33	IaAB	1.44	5.671
ddmi-168	Diavik	p	d	b	n	-5.61	238	48	20	190	IaAB	4.6	33.93
ddmi-169	Diavik	p	o	b	n	-5.21	43	0	0	43	IaA		
ddmi-172	Diavik	p	i	c	n	-5.00	132	0	0	132	IaA		

Sample	location	paragenesis	shape	colour	deformation	$\delta^{13}C$	N (at. ppm)	N_B (at. ppm)	%IaB	N_A	Type	H area (cm^{-2})	P area (cm^{-2})
ddmi-183	Diavik	p	o	b	n	-5.26	0	0		0	II	1.74	7.44
ddmi-184	Diavik	p	i	c	n	-5.44	262	2	1	259	IaA	1.69	
ddmi-186	Diavik	e	o	c	n	-4.88	788	0	0	788	IaA	18.62	
ddmi-187	Diavik	p	d	c	n	-4.58	373	0	0	373	IaA		13.5
ddmi-188	Diavik	p	o	b	y	-5.15	267	0	0	267	IaA		9.941
ddmi-196	Diavik	e	d/a	c	n	-5.07	711	0	0	711	IaA	2.89	
ddmi-198	Diavik	e	d/a	c	n	-5.27	511	0	0	511	IaA	3.36	
ddmi-199	Diavik	l	o	b	n	-5.17	683	113	17	570	IaAB	3.74	31.3
ddmi-200	Diavik		d/m	c	n	-4.58	626	42	7	584	IaA		35.3
ddmi-202	Diavik	p	o	b	n	-5.04	409	33	8	376	IaA		5.67
ddmi-203	Diavik	p	o	c	n	-4.32	301	0	0	301	IaA		9.26
ddmi-205	Diavik	e	o	p	n	-4.79	1263	199	16	1064	IaAB	17.4	
ddmi-206	Diavik	p	o	b	n	-5.15	1000	222	22	777	IaAB	1.99	80.17
ddmi-207	Diavik	p	i	c	y	-5.51	372	0	0	372	IaA		15.17
ddmi-208	Diavik	e	o	y	n	-5.02	1072	366	34	706	IaAB	4.4	235.24
ddmi-210	Diavik	p	o	b	n	-5.35	177	98	56	78	IaAB	11.48	27.67
ddmi-213	Diavik	p	d	b	n	-5.18	263	175	67	88	IaAB		108.79
ddmi-215	Diavik	p	i	c	n	-5.04	1749	0	0	1749	IaA	24.62	
dam 01	Damtshaa	w	i/d	c	n	-4.91	274	76	28	198	IaAB	1.30	31.85
dam 02	Damtshaa	w	i/m	b	n	-10.63	69	43	61	27	IaAB	2.34	15.76
dam 03	Damtshaa	e	i/d	c	n	-4.84	137	0	0	137	IaA		
dam 04	Damtshaa	e	d	c	n	-10.51	945	171	18	774	IaAB	7.5	92.19
dam 05	Damtshaa	e	d	c	n	-17.6	106	28	26	78	IaAB	3.53	12.6
dam 06	Damtshaa	e	d	c	n	-5.56	201	46	23	155	IaAB	1.92	28.07
dam 07	Damtshaa	e	i/d	c	n	-4.82	200	39	20	160	IaAB	0.73	5.74
dam 08	Damtshaa	e	i/d	y	n	-8.56	36	12	32	25	IaAB	6.15	
dam 09	Damtshaa	e	i/d	c	n	-4.81	22	1	5	21	IaA	0.26	1.14
dam 11	Damtshaa	e	d	c	n	-5.03	532	208	39	323	IaAB	6.90	112.18
dam 12	Damtshaa	e	o	c	n	-4.56	1015	448	44	567	IaAB	8.16	241.89
dam 13	Damtshaa	e	o	c	n	-10.78	734	467	64	267	IaAB	14.81	284.08
dam 14	Damtshaa	e	f/d	c	n	-4.55	79	11	14	68	IaAB	6.0	1.07
dam 15	Damtshaa	e	o	b	y	-5.25	1154	481	42	673	IaAB	3.3	273.42
dam 16	Damtshaa	e	i/d	c	n	-4.37	189	19	10	169	IaAB		28.442
dam 17	Damtshaa	e	d	b	y	-15.32	129	57	44	72	IaAB	0.69	26.7
dam 18	Damtshaa	e	i/d	b	n	-4.83	806	357	44	449	IaAB	3.1	205.25
dam 19	Damtshaa	e	d	c	n	-4.53	378	165	44	213	IaAB	6.38	110.36
dam 20	Damtshaa	e	d	c	n	-4.45	631	306	49	325	IaAB	6.1	153.78

Sample	location	paragenesis	shape	colour	deformation	$\delta^{13}C$	N (at. ppm)	N_B (at. ppm)	%IaB	N_A	Type	H area (cm^{-2})	P area (cm^{-2})
dam 21	Damtshaa	e	o	c	n	-16.24	271	59	22	213	IaAB	4.7	35.64
dam 22	Damtshaa	p	a	g	n	-4.92	338	101	30	237	IaAB	4.69	37.44
dam 23	Damtshaa	p	i/d	b	n	-5.32	454	223	49	231	IaAB	2.00	151.42
dam 24	Damtshaa	p	d	c	n	-5.28	438	134	31	304	IaAB	0.7	134.55
dam 25	Damtshaa	p	i/d	c	n	-6.14	221	42	19	179	IaAB	1.37	27.132
dam 26	Damtshaa	p	a	g	n	-8.36	108	5	4	104	IaA	1.74	11.08
dam 27	Damtshaa	p	i/d	c	n	-5.64	360	98	27	261	IaAB	0.73	65.19
dam 28	Damtshaa	p	i/d	c	n	-4.05	0	0		0	II		
dam 30	Damtshaa	p	d	c	n	-5.68	188	10	5	179	IaA	1.18	8.234
dam 31	Damtshaa	p	i/d	b	n	-3.28	194	0	0	194	IaA	2.37	15.25
dam 32	Damtshaa	p	d/m	c	n	-7.64	27	8	31	19	IaAB	0.99	3.93
dam 33	Damtshaa	h	i/d	b	n	-9.2	79	23	29	57	IaAB	6.1	7.79
dam 34	Damtshaa	h	d/a	g	n	-5.7	143	23	16	120	IaAB	2.53	22.73
dam 35	Damtshaa	h	d	b	y	-4.08	88	22	25	66	IaAB	1.33	10.62
dam 36	Damtshaa	h	i/d/m	c	n	-4.17	35	12	33	24	IaAB	0.29	1.626
dam 37	Damtshaa	h	d	b	n	-4.08	12	0	0	12	IaA		0.54
dam 39	Damtshaa	p	d	b	n	-5	291	141	48	150	IaAB	2.20	64.76
dam 40	Damtshaa	e	o	c	n	-10.16	922	693	75	229	IaAB	18.39	407.27
dam 41	Damtshaa	p	d	b	y	-4.76	314	146	47	168	IaAB	1.48	87.32
dam 42	Damtshaa	p	d	c	n	-5.31	345	202	58	144	IaAB	2.55	117.73
dam 43	Damtshaa	p	i/d	c	n	-3.95	239	199	83	40	IaAB	11.50	101.47
dam 44	Damtshaa	p	d	c	n	-3.69	584	212	36	372	IaAB	0.24	153.72
dam 45	Damtshaa	p	d	c	n	-4.77	104	0	0	104	IaA		3.308
dam 46	Damtshaa	p	d/m	c	n	-2.61	6	0		6	II	1.19	3.78
dam 47	Damtshaa	p	o/a	c	n	-3.56	139	36	26	103	IaAB		21.904
dam 48	Damtshaa	p	d	c	n	-3.8	333	95	29	238	IaAB		48.65
dam 49	Damtshaa	p	d	c	n	-1.44	43	5	12	38	IaAB	0.98	1.54
dam 50	Damtshaa	p	i	c	n	-5.82	13	3	19	11	IaAB		1.16
dam 51	Damtshaa	p	d	t/g	n	-3.88	407	189	46	218	IaAB	1.67	139.82
dam 52	Damtshaa	p	d	c	n	-5.07	765	368	48	397	IaAB	9.8	226.53
dam 53	Damtshaa	e	d	c	n	-4.75	400	145	36	255	IaAB	9.92	88.74
dam 54	Damtshaa	e	i/d	c	n	-13.73	127	35	28	92	IaAB		23.96
dam 55	Damtshaa	p	f/d	c	n	-4.16	203	53	26	149	IaAB		28.23
dam 56	Damtshaa	e	o	c	n	-9.41	611	407	67	204	IaAB	41.4	275.26
dam 57	Damtshaa	e	i/d	c	n	-11	106	13	12	93	IaAB	1.14	10.38
dam 58	Damtshaa	e	d	c	n	-14.63	767	151	20	616	IaAB	0.6	110.13
dam 59	Damtshaa	e	o	c	n	-12.87	869	514	59	355	IaAB	38.8	250.52

Sample	location	paragenesis	shape	colour	deformation	$\delta^{13}C$	N (at. ppm)	N_B (at. ppm)	%IaB	N_A	Type	H area (cm^{-2})	P area (cm^{-2})
dam 60	Damtshaa	p	d	c	n	-4.94	604	244	40	360	IaAB	0.47	175.97
dam 61	Damtshaa	e	d/m	c	n	-8.22	0	0		0	II	0.95	
dam 62	Damtshaa	e	d	c	n	-9.14	126	38	30	89	IaAB	1.06	13.84
dam 63	Damtshaa	e	i/d	c	n	-5.51	55	16	29	39	IaAB		1.847
dam 65	Damtshaa	e	o	b	y	-8.58	41	10	24	31	IaAB	0.27	1.362
dam 66	Damtshaa	e	d	t/g	n	-3.78	359	12	3	347	IaA	0.63	32.77
dam 67	Damtshaa	e	d	b	y	-5	141	7	5	133	IaA	0.29	13.05
dam 68	Damtshaa	p	d	c	n	-3.84	974	549	56	425	IaAB	2.23	316.49
dam 69	Damtshaa	p	d/m	c	n	-3.44	46	12	26	34	IaAB	1.13	6.39
dam 70	Damtshaa	p	d	c	y	-4.95	186	48	26	139	IaAB	0.33	37.39
dam 71	Damtshaa	e	f/d/m	c	n	-4.99	1098	319	29	779	IaAB	1.9	157.82
dam 72	Damtshaa	p	f/d/m	b	n	-4.85	319	274	86	45	IaAB	7.58	61.65
dam 74	Damtshaa	p	d	c	n	-4.93	204	91	45	113	IaAB	1.42	62.25
dam 75	Damtshaa	e	d	c	n	-5.52	980	515	53	465	IaAB	3.38	330.62
dam 76	Damtshaa	e	d	c	y	-5.11	358	155	43	204	IaAB	0.38	95.25
dam 78	Damtshaa	e	o	t/g	n	-6.99	146	53	36	94	IaAB	0.5	32.9
dam 79	Damtshaa	h	i/d	c	n	-7.01	91	19	21	72	IaAB	3.59	9.69
dam 80	Damtshaa	h	d	c	y	-4.04	207	151	73	57	IaAB	2.73	76.019
dam 81	Damtshaa	p	o	c	n	-3.4	572	290	51	283	IaAB	1.1	183.58
dam 82	Damtshaa	h	f/d	b	n	-8.07	69	28	41	40	IaAB	0.91	5.01
dam 83	Damtshaa	p	o	t/g	n	-4.63	834	298	36	536	IaAB	23.69	110.23
dam 84	Damtshaa	p	o	t/g	n	-3.24	332	52	16	280	IaAB		41.81
dam 85	Damtshaa	p	o	t/g	n	-4.23	412	94	23	318	IaAB	1.17	83.45
dam 86	Damtshaa	p	i/d	g	n	-4.87	335	168	50	166	IaAB	1.54	131.52
dam 87	Damtshaa	p	o	c	n	-3.76	521	182	35	339	IaAB	0.78	123.94
dam 88	Damtshaa	e	o	c	n	-7.98	222	3	1	219	IaA	3.41	3.64
dam 89	Damtshaa	p	o	t/g	n	-3.31	294	35	12	259	IaAB	0.26	36.567
dam 90	Damtshaa	p	i/d	t/g	n	-4.99	366	106	29	260	IaAB	4.36	75.47
dam 91	Damtshaa	e	o	c	n	-7.99	189	86	46	103	IaAB	2.01	62.76
dam 92	Damtshaa	p	d	t/g	n	-3.24	439	113	26	326	IaAB		60.09
dam 93	Damtshaa	p	d	c	n	-4.21	407	92	22	315	IaAB	0.59	70.94
dam 94	Damtshaa	p	i/d	c	n	-5.67	153	51	33	102	IaAB	4.80	29.878
dam 95	Damtshaa	e	i/d	c	n	-16.43	661	441	67	220	IaAB	0.33	284.37
dam 96	Damtshaa	p	i/d	b	y	-3.58	122	20	16	102	IaAB	0.30	2.18
dam 97	Damtshaa	p	i/d	b	n	-4.05	123	38	31	85	IaAB	2.45	12.68
PA-01	Panda	h	O	b	y	-5.58	176	126	72	50	IaAB	12.53	69.883
PA-02	Panda	h	m	b	n	-5.22	411	65	16	346	IaAB	4.91	23.135

Sample	location	paragenesis	shape	colour	deformation	$\delta^{13}C$	N (at. ppm)	N_B (at. ppm)	%IaB	N_A	Type	H area (cm^{-2})	P area (cm^{-2})
PA-03	Panda	h	m	b	y	-4.58	86	19	22	67	IaAB	4.72	6.211
PA-04	Panda	h	m	b	y	-5.81	94	42	45	52	IaAB	1.59	8.268
PA-05	Panda	h	f/d	b	y	-5.04	70	48	69	22	IaAB	0.51	2.442
PA-06	Panda	h	O	b	y	-5.51	137	76	55	61	IaAB	5.53	24.169
PA-07	Panda	h	O	b	y	-5.21	19	0	0	19	IaA	0.81	0
PA-08	Panda	h	O	b	y	-5.19	24	11	46	13	IaAB	0.74	0
PA-09	Panda	h	O	b	y	-5.28	389	69	18	320	IaAB	5.39	24.831
PA-10	Panda	h	i/m	b	y	-5.65	31	6	19	25	IaAB	3.07	5.653
PA-11	Panda	l	D	b	y	-5.32	455	225	49	230	IaAB	1.01	170.549
PA-12	Panda	h	O	b	y	-5.05	175	36	21	139	IaAB	2.48	23.98
PA-13	Panda	h	O	b	y	-5.07	67	24	36	43	IaAB	1.8	6.297
PA-14	Panda	h	O	b	y	-6.93	484	88	18	396	IaAB	13.96	49.025
PA-15	Panda	h	O	b	y	-14.05	112	87	78	25	IaAB	3.33	0
PA-16	Panda	h	O	b	y	-5.00	116	59	51	57	IaAB	10.49	11.076
PA-17	Panda	h	f/d	b	y	-5.45	46	28	61	18	IaAB	1.59	1.244
PA-18	Panda	h	D	b	y	-4.99	62	30	48	32	IaAB	2.96	6.748
PA-19	Panda	l	O	b	y	-5.71	111	44	40	67	IaAB	6.37	14.996
PA-20	Panda	h	O	b	y	-5.01	184	113	61	71	IaAB	5.01	59.343
PA-21	Panda	h	O	b	y	-5.50	63	50	79	13	IaAB	2.83	2.413
PA-22	Panda	h	i	b	y	-4.27	91	67	74	24	IaAB	9.58	32.688
PA-23	Panda	l	O	b	y	-4.85	473	244	52	229	IaAB	4.81	161.295
PA-24	Panda	p	i	c	n	-3.58	857	152	18	705	IaAB	0.81	79.705
PA-25	Panda	p	D	b	y	-5.73	269	194	72	75	IaAB	7.13	124.22
PA-26	Panda	p	D	c	n	-5.14	62	0	0	62	IaA		2.324
PA-27	Panda	p	i/m	b	n	-4.33	199	17	9	182	IaA		6.136
PA-28	Panda	p	i	b	y	-4.98	209	58	28	151	IaAB		3.68
PA-29	Panda	p	i	b	y	-5.32	299	39	13	260	IaAB	0.64	12.925
PA-30	Panda	p	i	b	n	-4.77	123	0	0	123	IaA		1.972
PA-31	Panda	p	i	b	y	-5.05	189	23	12	166	IaAB		5.23
PA-32	Panda	p	i	b	n	-2.98	370	36	10	334	IaA		30.332
PA-33	Panda	p	i	b	n	-4.87	380	64	17	316	IaAB		22.225
PA-34	Panda	p	i	b	n	-5.31	377	97	26	280	IaAB		17.456
PA-35	Panda	p	i	b	n	-5.07	151	14	9	137	IaA		0
PA-36	Panda	p	O	b	y	-4.73	429	167	39	262	IaAB	12.78	106.18
PA-37	Panda	p	O	b	y	-5.96	87	47	54	40	IaAB	2.76	19.464
PA-38	Panda	p	O	c	n	-4.34	295	22	7	273	IaA	3.9	44.484
PA-39	Panda	lm	i	b	y	-3.55	0	0		0	II	0.90	0
PA-40	Panda	l	f/d/m	b	y	-5.75	0	0		0	II		0

Sample	location	paragenesis	shape	colour	deformation	$\delta^{13}C$	N (at. ppm)	N_B (at. ppm)	%IaB	N_A	Type	H area (cm^{-2})	P area (cm^{-2})
PA-41	Panda	p	i	b	y	-5.12	85	36	42	49	IaAB	5.72	26.455
PA-42	Panda	h	m	b	y	-4.86	41	6	15	35	IaAB	2.55	4.579
PA-43	Panda	p	m	b	n	-5.15	303	103	34	200	IaAB	7.20	64.34
PA-44	Panda	p	i	b	y	-4.87	27	0	0	27	IaA		0
PA-45	Panda	p	i	b	n	-5.71	87	44	51	43	IaAB	3.52	12.055
PA-46	Panda		O	c	n	-4.27	161	37	23	124	IaAB	8.93	23.859
PA-47	Panda	p	O	c	n	-5.03	1260	163	13	1097	IaAB	2.75	76.956
PA-48	Panda	p	O	b	y	-5.45	964	249	26	715	IaAB	2.5	146.51
PA-49	Panda	lm	i	b	n	-4.01	72	42	58	30	IaAB	5.67	33.058
PA-50	Panda	p	O	c	n	-5.57	0	0		0	II	1.12	0
PA-51	Panda	p	f/d/m	b	y	-5.71	545	33	6	512	IaA		30.974
PA-52	Panda		i	b	y	-5.79	357	91	25	266	IaAB	4.65	64.118
PA-53	Panda	lm	i	b	y	-3.50	0	0		0	II	0.91	1.499
PA-54	Panda	lm	O	b	y	-5.27				0	II	0.77	5.96
PA-55	Panda	p	O	b	n	-6.36	96	62	65	34	IaAB	15.19	30.046
PA-56	Panda	p	i	c	n	-4.96	843	784	93	59	IaB	126.73	432.12
PA-57	Panda	p	i	c	n	-4.96	409	44	11	365	IaAB		28.309
PA-58	Panda	h	m	b	n	-5.40	196	132	67	64	IaAB	11.82	16.442
PA-59	Panda	l	i	b	y	-4.42	20	19	95	1	IaB	1.42	0
PA-60	Panda	l	i	c	n	-6.10	677	589	87	88	IaAB	15.37	344.093
PA-61	Panda	l	i	c	n	-4.46	0	0		0	II		0
PA-62	Panda	l	i	b	y	-4.56	0	0		0	II	0.97	0
PA-63	Panda	e	i/a	b	n	-11.21	73	73	100	0	IaB	19.29	26.699
PA-64	Panda	e	c/a	c	n	-5.10	811	39	5	772	IaA	5.76	0
PA-65	Panda	e	m	c	n	-19.40	801	801	100	0	IaB	42.05	299.419
PA-66	Panda	e	o/m	c	n	-9.90	778	71	9	707	IaA	20.03	27.455
PA-67	Panda	l	i/a	c	n	-4.59	81	71	88	10	IaAB	8.30	0
PA-68	Panda	l	i/a	c	n	-5.59	147	147	100	0	IaB	11.32	0
PA-69	Panda	l	o/a	c	n	-5.29	917	74	8	843	IaA	0.90	60.777
PA-70	Panda	l	i	b	n	-5.07	85	23	27	62	IaAB	6.62	3.934
PA-71	Panda	e	i	b	n	-8.36	30	18	60	12	IaAB	7.48	3.041
PA-72	Panda	lm	i	b	y	-4.46	0	0		0	II		0
PA-73	Panda	e	c/a	c	n	-5.45	923	72	8	851	IaA	14.31	0
PA-74	Panda	e	c/a	c	n	-4.37	651	0	0	651	IaA	2.62	0
PA-75	Panda	p	o	c	n	-4.73	780	47	6	733	IaA		37.148
PA-76	Panda		O	c	n	-4.91	816	18	2	798	IaA		18.436
PA-77	Panda					-3.91	951	220	23	731	IaAB	2.90	101.523
PA-78	Panda	p	O	c	n	-5.12	491	81	16	410	IaAB	0.96	42.574

Sample	location	paragenesis	shape	colour	deformation	$\delta^{13}C$	N (at. ppm)	N_B (at. ppm)	%IaB	N_A	Type	H area (cm^{-2})	P area (cm^{-2})
PA-79	Panda	p	i	c	n	-4.68	473	47	10	426	IaA	0.74	33.414
PA-80	Panda	p	i/m	c	n	-4.90	630	32	5	598	IaA	0.88	59.232
PA-81	Panda	p	O	b	y	-5.07	61	0	0	61	IaA	1.8	4.328
PA-82	Panda	p	O	c	n	-4.33	236	61	26	175	IaAB		0
PA-83	Panda	p	O	b	n	-5.37	217	0	0	217	IaA		3.538
PA-84	Panda	p	O	b	n	-5.14	712	629	88	83	IaAB	8.88	407.885
PA-85	Panda	p	O	b	y	-2.98	367	22	6	345	IaA		6.634
PA-86	Panda	p	i	b	y	-5.21	331	31	9	300	IaA		7.78
PA-87	Panda	p	i	b	y	-5.21	44	15	34	29	IaAB	1.36	8.693
PA-88	Panda	p	i	c	n	-4.93	510	78	15	432	IaAB	0.58	41.318
PA-89	Panda	p	O	c	n	-4.78	720	93	13	627	IaAB	0.69	30.084
PA-90	Panda	p	i	b	n	-5.81	72	0	0	72	IaA		0
WW-004	Wawa	p	o	b	n	-3.40	86	6	7	79	IaA	0.42	2.72
WW-005	Wawa	p	d	l/b	n	-1.20	3	0		3	II	0.94	
WW-009	Wawa		d	c	n	-2.92	47	35	75	12	IaAB	4.34	
WW-010	Wawa	p	i/d	c	n	-4.59	83	58	70	25	IaAB	8.40	26.19
WW-016	Wawa	p	o/d	l/b	n	-2.16	15	13	86	2	IaAB	0.30	0.807
WW-019	Wawa	p	o	b	n	-1.94	48	4	8	44	IaA	2.20	
WW-041	Wawa		i/o	c	n	-3.30	41	33	81	8	IaAB	11.21	14.89
WW-057	Wawa	p	o	b		-3.76	41	12	29	29	IaAB	0.15	
WW-059	Wawa	p	i/d	b	y	-3.40	173	127	73	46	IaAB	1.52	90.78
WW-067	Wawa		d/o/a	l/b	n	-1.10	74	48	65	26	IaAB	4.72	5.66
WW-070	Wawa	p	i/o/a	b	n	-3.49	42	12	29	30	IaAB		
WW-086	Wawa	deep-h	o/d	l/b	n		33	22	66	11	IaAB		
WW-095	Wawa	p	o	l/b	n	-3.13	51	22	44	28	IaAB	3.62	
WW-201	Wawa		d	c	n		116	113	97	4	IaB	39.28	38.87
WW-202	Wawa		d/m	l/b	n	-4.01	49	30	62	19	IaAB	8.06	14.8
WW-204	Wawa	p	o/m	c	n		89	78	88	10	IaAB	27.47	30.55
WW-205	Wawa	p	i/m	c	n		24	0	0	24	IaA	0.66	
WW-207	Wawa	p	cubo-o	c	n		0	0		0	II	1.09	
WW-208	Wawa	p	o/d	c	n	-3.59	6	1		5	II		
WW-210	Wawa		i/o	c	n		11	0	0	11	IaA	0.48	
WW-211	Wawa	p	o/a	l/b	n		7	7		0	II	5.17	4.413
WW-214	Wawa		a	c	n		50	0	0	50	IaA	1.30	
WW-301	Wawa	h	d/o/m	c	n		0	0		0	II	0.30	2.7
WW-303	Wawa		i/o	b	n		615	110	18	506	IaAB	4.25	
JF-001	Jagersfontein	deep-e				-21.21	0	0		0	II	1.78	

Sample	location	paragenesis	shape	colour	deformation	$\delta^{13}C$	N (at. ppm)	N_B (at. ppm)	%IaB	N_A	Type	H area (cm^{-2})	P area (cm^{-2})
JF-003	Jagersfontein	p				-6.10	282	60	21	222	IaAB	3.12	42.118
JF-004	Jagersfontein	e				-4.07	415	188	45	228	IaAB	3.45	90.62
JF-005	Jagersfontein	p				-7.51	285	272	96	13	IaB	34.04	154.72
JF-008	Jagersfontein	e				-5.33	684	492	72	192	IaAB	3.04	292.16
JF-009	Jagersfontein	deep-e				-21.82	0	0		0	II	1.80	
JF-010	Jagersfontein	p				-6.63	12	4	36	8	IaAB	2.81	
JF-011	Jagersfontein	e				-4.49	88	28	32	60	IaAB	1.24	
JF-012	Jagersfontein	e				-3.94	64	50	78	14	IaAB	14.43	
JF-013	Jagersfontein	e				-5.64	638	427	67	211	IaAB	2.14	265.17
JF-015	Jagersfontein	e				-4.36	811	361	44	450	IaAB		1.69
JF-016	Jagersfontein						830	464	56	367	IaAB		246.5
JF-017	Jagersfontein	p				-2.59	8	3		5	II	2.8	
JF-019	Jagersfontein	e				-19.76	130	54	42	75	IaAB	0.84	34.62
JF-020	Jagersfontein	e				-3.85	611	298	49	313	IaAB	0.84	185.38
JF-021	Jagersfontein						881	743	84	138	IaAB	5.43	340.75
JF-022	Jagersfontein	deep-e				-17.25	20	20	100	0	IaB	8.71	
JF-023	Jagersfontein	e				-4.48	398	116	29	283	IaAB	3.37	87.98
JF-024	Jagersfontein	p				-4.74	10	0	0	10	IaA	0.18	
JF-025	Jagersfontein						0	0		0	II	1.26	
JF-026	Jagersfontein	e				-18.40	345	138	40	207	IaAB	7.47	64.47
JF-028	Jagersfontein						681	67	10	614	IaA	0.29	39.62
JF-029	Jagersfontein						222	66	30	156	IaAB	1.01	37.73
JF-030	Jagersfontein	p				-4.48	642	119	18	524	IaAB	1.12	62.04
JF-031	Jagersfontein	e				-9.22	0	0		0	II		
JF-032	Jagersfontein	h				-4.10	333	261	78	72	IaAB	4.44	119.38
JF-033	Jagersfontein	h				-5.02	418	116	28	301	IaAB		29.04
JF-034	Jagersfontein	e				-19.29	34	20	58	14	IaAB	10.98	
JF-035	Jagersfontein	h				-4.95	77	2	2	76	IaA		
JF-036	Jagersfontein	h				-5.33	15	0	0	15	IaA	2.28	
JF-037	Jagersfontein	deep-e				-21.67	47	19	41	28	IaAB	4.45	5.87
JF-039	Jagersfontein	deep-e				-17.91	46	39	85	7	IaAB	15.92	
JF-040	Jagersfontein	e				-17.40	0	0		0	II		
JF-041	Jagersfontein	e				-15.62	0	0		0	II	2.55	
JF-042	Jagersfontein	deep-e				-17.36	14	14	100	0	IaB	5.88	
JF-043	Jagersfontein	w				-18.74	0	0		0	II	0.24	
JF-045	Jagersfontein						42	0	0	42	IaA		
JF-046	Jagersfontein	h				-3.52	3	1		2	II	0.33	

Sample	location	paragenesis	shape	colour	deformation	$\delta^{13}C$	N (at. ppm)	N_B (at. ppm)	%IaB	N_A	Type	H area (cm^{-2})	P area (cm^{-2})
JF-047	Jagersfontein	e				-15.96	78	45	57	34	IaAB	6.48	18.47
JF-048	Jagersfontein	e				-23.60	0	0		0	II	0.27	
JF-049	Jagersfontein	e				-17.17	59	0	0	59	IaA	1.51	
JF-050	Jagersfontein	deep-e				-19.88	85	71	84	14	IaAB	5.3	9.39
JF-051	Jagersfontein	e				-22.61	7	7		0	II	2.90	
JF-053	Jagersfontein	e				-4.33	23	0	0	23	IaA		
JF-054	Jagersfontein	w				-17.15	30	30	100	0	IaB		
JF-055	Jagersfontein	deep-e				-17.55	0	0		0	II	2.66	
JF-056	Jagersfontein	e				-12.98	57	37	65	20	IaAB	6.50	19.56
JF-057	Jagersfontein	h				-5.65	219	34	15	186	IaAB	1.42	27.62
JF-058	Jagersfontein	deep-e				-23.01	8	0		8	II	1.04	
JF-059	Jagersfontein	e				-4.27	158	88	55	71	IaAB	1.47	39.91
JF-060	Jagersfontein	w				-4.27	179	27	15	151	IaAB	0.9	13.72
JF-061	Jagersfontein	e				-4.69	189	0	0	189	IaA		1.73
JF-062	Jagersfontein	h				-4.12	18	13	76	4	IaAB	0.92	
JF-063	Jagersfontein	e				-14.26	410	395	96	15	IaB	2.9	115.18
JF-064	Jagersfontein	h				-4.58	104	9	8	96	IaA	1.75	10.51
JF-065	Jagersfontein	p				-3.13	529	208	39	321	IaAB	0.92	114.18
JF-066	Jagersfontein	e				-24.22	0	0		0	II		
JF-067	Jagersfontein	e				-4.15	447	136	30	310	IaAB	1.97	92.25
JF-068	Jagersfontein	e				-18.24	2	0		2	II		
JF-069	Jagersfontein	e				-4.39	558	141	25	417	IaAB	0.8	76.95
JF-070	Jagersfontein	e				-16.35	93	34	36	59	IaAB	0.78	15.791
JF-071	Jagersfontein						1	1		0	II		
JF-072	Jagersfontein	e				-17.20	33	23	70	10	IaAB	11.0	
JF-073	Jagersfontein	p				-6.42	63	4	6	59	IaA		
JF-074	Jagersfontein	e				-1.61	400	89	22	311	IaAB	1.19	55.08
JF-075	Jagersfontein						777	315	41	462	IaAB	1.84	197.2
JF-076	Jagersfontein	e				-5.24	49	11	23	38	IaAB	2.16	
JF-077	Jagersfontein	e				-5.16	642	137	21	505	IaAB		33.14
JF-078	Jagersfontein	p				-3.46	169	57	34	112	IaAB	1.43	37.41
JF-079	Jagersfontein	e				-5.10	764	134	18	630	IaAB	1.14	37.41
JF-080	Jagersfontein	e				-22.76	37	7	20	30	IaAB	4.36	
JF-081	Jagersfontein	e				-4.88	0	0		0	II		
JF-082	Jagersfontein						887	267	30	620	IaAB	52.63	90.14
JF-084	Jagersfontein	deep-e				-20.86	53	23	44	30	IaAB	3.53	1.26
JF-085	Jagersfontein						486	74	15	412	IaAB		54.31

Sample	location	paragenesis	shape	colour	deformation	$\delta^{13}C$	N (at. ppm)	N_B (at. ppm)	%IaB	N_A	Type	H area (cm^{-2})	P area (cm^{-2})
JF-087	Jagersfontein						396	17	4	379	IaA	0.40	22.95
JF-089	Jagersfontein						108	23	22	85	IaAB	3.39	12.58
JF-091	Jagersfontein	e				-3.65	631	201	32	430	IaAB	1.30	137.58
JF-092	Jagersfontein	e				-5.57	495	264	53	231	IaAB	1.16	158.87
JF-093	Jagersfontein						0	0		0	II	0.75	
JF-094	Jagersfontein	p				-1.08	0	0		0	II		
JF-095	Jagersfontein	e				-5.41	851	321	38	530	IaAB	1.73	204.36
JF-096	Jagersfontein	e				-18.12	20	1	2	20	IaA		
JF-097	Jagersfontein	p				-7.58	8	3		5	II	0.58	
JF-098	Jagersfontein	p				-5.06	0	0		0	II	1.50	
JF-099	Jagersfontein						945	372	39	572	IaAB	1.92	217.85
JF-100	Jagersfontein						263	0	0	263	IaA		4.301
JF-101	Jagersfontein						0	0		0	II	1.15	
JF-102	Jagersfontein						346	16	5	329	IaA	0.36	2.88
JF-103	Jagersfontein	altered				-21.72	91	54	59	37	IaAB	2.30	
JF-104	Jagersfontein						310	113	36	198	IaAB	4.08	76.58
JF-105	Jagersfontein	p				-5.86	317	23	7	294	IaA	2.77	16.61
JF-106	Jagersfontein	p				-2.61	447	81	18	367	IaAB		45.15
JF-107	Jagersfontein	h				-5.28	230	39	17	190	IaAB	3.4	26.41
JF-109	Jagersfontein	p				-3.96	510	155	30	355	IaAB	0.62	107.88
JF-110	Jagersfontein	e				-13.93	298	189	63	109	IaAB	11.50	93.62
JF-111	Jagersfontein	e				-3.16	326	108	33	218	IaAB	1.84	64.62
JF-112	Jagersfontein	p				-3.92	571	127	22	443	IaAB	1	77.42
JF-113	Jagersfontein	altered				-19.07	0	0		0	II		
JF-114	Jagersfontein	h				-3.94	102	28	27	74	IaAB	6.25	14.09
JF-115	Jagersfontein	p				-4.33	22	17	75	6	IaAB	0.60	3.03
JF-116	Jagersfontein	p				-7.65	29	18	61	11	IaAB	4.94	
JF-117	Jagersfontein						103	15	15	88	IaAB	1.74	9.37
JF-118	Jagersfontein	p				-2.04	27	0	0	27	IaA	0.47	
JF-119	Jagersfontein						1042	182	17	860	IaAB	0.7	95.51
JF-120	Jagersfontein	e				-5.13	586	90	15	496	IaAB		70.54
JF-121	Jagersfontein						0	0		0	II	0.99	
JF-122	Jagersfontein	w				-15.43	0	0		0	II	1.10	
JF-123	Jagersfontein	p				-4.35	397	65	16	332	IaAB		36.29
JF-124	Jagersfontein	p				-5.51	56	0	0	56	IaA	0.40	2.71
AR01	Arenapolis		d	c		-4.06	585	255	44	330	IaAB	1.23	160.57
AR02	Arenapolis		d	c		-4.14	144	82	57	61	IaAB	0.07	30.37

Sample	location	paragenesis	shape	colour	deformation	$\delta^{13}C$	N (at. ppm)	N_B (at. ppm)	%IaB	N_A	Type	H area (cm^{-2})	P area (cm^{-2})
AR03	Arenapolis		i	b		-5.24	27	11	40	16	IaAB	1.1	
AR04	Arenapolis	p	d	c	n	-3.06	71	49	70	21	IaAB	8.01	14.908
AR05	Arenapolis	p	d	c	n	-4.93	60	53	89	7	IaAB	2.14	36.53
AR06	Arenapolis		o	y		-4.57	16	14	89	2	IaAB	0.65	
AR07	Arenapolis	p	f/o	b	n	-4.95	83	38	45	46	IaAB	3.79	11.14
AR08	Arenapolis	p	o/d	b	n	-5.02	427	351	82	76	IaAB	0.21	254.81
AR09	Arenapolis	p	d	b	n	-4.55	252	33	13	219	IaAB		19.32
AR10	Arenapolis	p	d	c	n	-5.04	0	0		0	II		
AR11	Arenapolis	p	o	c	n	-5.19	92	58	64	33	IaAB	7.4	55.27
AR12	Arenapolis	p	i	c		-6.20	162	117	72	45	IaAB	8	53.97
AR13	Arenapolis	p	f/d	c		-2.04	43	33	76	10	IaAB	0.24	6.63
AR14	Arenapolis	p	f/d	c	n	-3.06	7	3		4	II		
AR16	Arenapolis	p	o/d	c	n	-3.94	626	390	62	236	IaAB	9.3	245.72
AR17	Arenapolis	p	o/d	c		-3.08	767	90	12	677	IaAB	0.83	38.52
AR19	Arenapolis	p	i	c	n	-3.92	157	22	14	135	IaAB	8.09	33.33
AR20	Arenapolis	p	i	c	n	-5.86	439	428	98	11	IaB	3.03	44.77
BV01	Boa Vista	h	d/m	c	n	-2.97	9	7		2	II		
BV02	Boa Vista	h	f/d	c	n	-4.03	162	61	37	101	IaAB		
BV03	Boa Vista	h	o/d	c	n	-3.87	309	55	18	254	IaAB		22.54
BV04	Boa Vista	p	o	c	n	-3.00	263	7	3	255	IaA	1.74	
BV06	Boa Vista	p	o	c	n	-7.48	272	208	76	65	IaAB	2.14	110.25
BV08	Boa Vista	p	i	c	n	-3.12	7	4		3	II	0.44	1.043
BV09	Boa Vista	p	f/d	c	n	-7.61	144	65	45	79	IaAB	0.26	38.12
BV10	Boa Vista	p	f/d	c	n	-5.98	445	142	32	303	IaAB	0.52	112.48
BV11	Boa Vista	p	d	c	n	-4.40	682	347	51	335	IaAB	1.6	192.46
BV12	Boa Vista	p	d	c	n	-4.87	54	44	81	11	IaAB	2.33	6.36
BV13	Boa Vista	p	o/d	c	n	-2.96	269	89	33	180	IaAB	4.05	44.55
BV14	Boa Vista		o/d	c		-5.22	602	236	39	365	IaAB	4.49	153.75
BV15	Boa Vista		o/d	c		-4.49	362	263	73	99	IaAB	5.78	144.14
BV16	Boa Vista	h	i	b	n	-6.14	27	27	100	0	IaB	0.62	
BV17	Boa Vista	h	d	b	y	-3.29	67	10	14	57	IaAB		4.3
BV19	Boa Vista	h	d	c	n	-2.12	216	124	57	93	IaAB	3.06	68.43
BV21	Boa Vista	h	f/d/m	c	n	-3.78	242	87	36	155	IaAB	4.26	43.74
BV22	Boa Vista	h	o	c	n	-3.93	63	33	52	30	IaAB	2.32	14.44
BV23	Boa Vista	h	o	c	n	-5.72	30	30	100	0	IaB		
BV25	Boa Vista	h	o	c	n	-4.69	1018	214	21	804	IaAB	7.26	116.65
BV26	Boa Vista	p	o/m/a	c	n	-4.28	104	15	14	89	IaAB	1.37	5.8

Sample	location	paragenesis	shape	colour	deformation	$\delta^{13}C$	N (at. ppm)	N_B (at. ppm)	%IaB	N_A	Type	H area (cm^{-2})	P area (cm^{-2})
BV27	Boa Vista	p	o	c	n	-4.33	592	404	68	188	IaAB	13.98	235.6
BV28	Boa Vista	p	i/a	c		-5.21	450	268	59	182	IaAB	6.12	156.97
BV29	Boa Vista	p	d/m	c	n	-8.89	1097	964	88	133	IaAB	1.75	505.87
BV30	Boa Vista	p	d	y	n	-2.36	1626	1347	83	279	IaAB	4.49	686.22
BV31	Boa Vista	p	i	c	n	-4.25	15	0	0	15	IaA	0.15	
BV32	Boa Vista	p	o	c	n	-4.18	219	80	36	139	IaAB	3.40	45.21
BV33	Boa Vista	p	f/d	c	n	-5.17	314	65	21	249	IaAB	0.64	57.61
BV34	Boa Vista	e	d	c	n	-4.44	523	385	74	138	IaAB	5.37	191.66
CA01	Canastra	p	d	c	y	-3.71	187	22	12	165	IaAB		4.62
CA02	Canastra	p	o/d	c	n	-6.08	369	64	17	305	IaAB	2.38	37.09
CA03	Canastra	p	o/d	c	n	-6.40	241	91	38	151	IaAB	1.21	49.94
CA04	Canastra		o	c		-6.67	98	13	13	85	IaAB	0.56	2.39
CA05	Canastra	p	f/d	c	n	-5.00	335	207	62	128	IaAB		132.83
CA06	Canastra		d	b		-4.91	126	59	47	67	IaAB	0.92	11.07
CA07	Canastra		o/m	c		-4.79	368	275	75	93	IaAB	15.79	187.44
CA08	Canastra		d	c		-5.86	166	88	53	78	IaAB	1.0	78.296
CA09	Canastra		i	c		-6.15	446	22	5	424	IaA	0.44	29.52
CA10	Canastra	p	o/d	y	n	-5.40	11	0	0	11	IaA	1.09	1.25
CA11	Canastra		d	y		-19.70	2	0		2	II	8.17	
CA12	Canastra	p	d	c	n	-5.36	113	71	63	42	IaAB		50.83
CA13	Canastra	p	o/d	c	n	-5.80	512	35	7	477	IaA	1.29	28.71
CA14	Canastra	e	i	c	n	-16.08	51	11	21	40	IaAB	1.67	3.54
DBP003	De Beers Pool	p		c			7	0		7	II		
DBP005	De Beers Pool	p		c			100	13	13	88	IaAB	1.13	9.59
DBP006	De Beers Pool	p		c			89	6	7	83	IaA	0.98	7.41
DBP011	De Beers Pool	p		c			84	47	56	37	IaAB	0.18	3.23
DBP015	De Beers Pool	h		c			9	0		9	II	0.29	
DBP019	De Beers Pool	h		c			11	7	63	4	IaAB		
DBP047	De Beers Pool	h		I/b			17	0	0	17	IaA	1.01	
DBP049	De Beers Pool	h		c			117	25	21	92	IaAB	0.65	8.7
DBP057	De Beers Pool	p		c			0	0		0	II	1.42	
DBP059	De Beers Pool	h		c			28	1	5	26	IaA	0.3	1.794
DBP062	De Beers Pool	h		c			10	6		3	II	2.8	
DBP064	De Beers Pool	h		c			68	13	19	55	IaAB	1.43	6.022
DBP068	De Beers Pool	h		I/b			0	0		0	II	2.15	
DBP070	De Beers Pool	h		c			0	0		0	II	0.45	
DBP076	De Beers Pool	p		c			183	8	4	175	IaA		12.78

Sample	location	paragenesis	shape	colour	deformation	$\delta^{13}C$	N (at. ppm)	N_B (at. ppm)	%IaB	N_A	Type	H area (cm^{-2})	P area (cm^{-2})
DBP078	De Beers Pool	p		c			536	114	21	423	IaAB	1.57	32.93
DBP081	De Beers Pool	p		c			54	5	9	49	IaA		0.766
DBP083	De Beers Pool	p		c			47	13	28	34	IaAB	0.26	4.135
DBP088	De Beers Pool	p		c			44	9	22	34	IaAB	0.46	2.61
DBP089	De Beers Pool	p		c			735	122	17	613	IaAB	1.67	83.7
DBP093	De Beers Pool	p		c			193	16	8	178	IaA	0.58	19.87
DBP094	De Beers Pool	p		c			524	0	0	524	IaA	0.37	27.62
DBP097	De Beers Pool	p		c			27	0	0	27	IaA		
DBP099	De Beers Pool	p		c			28	0	0	28	IaA	1.9	2.82
DBP100	De Beers Pool	e		c			1459	503	34	956	IaAB	113.62	234.54
DBP106	De Beers Pool	e		c			149	22	15	127	IaAB	0.70	28.85
DBP110	De Beers Pool	p		I/b			30	20	65	10	IaAB	0.36	0.489
DBP113	De Beers Pool	p		c			34	8	23	26	IaAB		
DBP123	De Beers Pool	p		I/b			229	38	17	191	IaAB	1.70	16.25
DBP127	De Beers Pool	p		I/b			400	198	49	202	IaAB	1.68	130.85
DBP129	De Beers Pool	p		c			247	37	15	210	IaAB	0.59	21.31
DBP146	De Beers Pool	p		I/b			0	0		0	II	0.75	
DBP151	De Beers Pool	h		c			183	20	11	162	IaAB	0.44	17.02
DBP153	De Beers Pool	h		c			184	49	27	135	IaAB	1.05	19.39
DBP162	De Beers Pool	h		c			126	0	0	126	IaA		7.47
DBP166	De Beers Pool	h		c			0	0		0	II		
DBP172	De Beers Pool	h		c			262	49	19	213	IaAB	2.35	
DBP175	De Beers Pool	h		c			0	0		0	II	0.25	
DBP176	De Beers Pool	h		c			66	5	7	62	IaA	1.70	8.99
DBP180	De Beers Pool	h		c			75	0	0	75	IaA	0.92	1.49
DBP183	De Beers Pool	h		c			54	0	0	54	IaA		3.12
DBP184	De Beers Pool	h		c			0	0		0	II		
DBP186	De Beers Pool	h		c			0	0		0	II		
DBP206	De Beers Pool	h		c			33	3	8	30	IaA		
DBP209	De Beers Pool	p		c			27	6	23	21	IaAB	0.98	1.91
DBP211	De Beers Pool	h		c			0	0		0	II	0.20	
DBP212	De Beers Pool	p		c			0	0		0	II	3.00	
DBP214	De Beers Pool	p		c			150	16	11	134	IaAB	0.89	15.27
DBP219	De Beers Pool	p		c			83	42	51	41	IaAB	0.93	2.02
DBP221	De Beers Pool	p		c			16	4	26	12	IaAB	0.20	
DBP224	De Beers Pool	p		c			1055	305	29	750	IaAB	26.62	133.91
DBP230	De Beers Pool	p		c			278	35	13	243	IaAB	0.91	33.57

Sample	location	paragenesis	shape	colour	deformation	$\delta^{13}C$	N (at. ppm)	N_B (at. ppm)	%IaB	N_A	Type	H area (cm^{-2})	P area (cm^{-2})
DBP234	De Beers Pool	deep-h		c			766	557	73	209	IaAB	21.41	339.22
DBP245	De Beers Pool	e		c			133	49	37	84	IaAB	7.74	25.86
DBP252	De Beers Pool	h		c			18	0	0	18	IaA	0.76	1.52
DBP256	De Beers Pool	p		c			98	27	27	71	IaAB		15.53
DBP257	De Beers Pool	e		c			19	16	85	3	IaAB		
DBP259	De Beers Pool	h		c			52	5	10	46	IaAB	2.27	
DBP270	De Beers Pool	p		c			0	0		0	II	1.02	
DBP277	De Beers Pool	p		c			95	43	45	52	IaAB		
DBP285	De Beers Pool	p		c			767	157	20	610	IaAB	0.92	92.12
DBP288	De Beers Pool	p		c			20	7	38	12	IaAB		
DBP306	De Beers Pool	e		c			0	0		0	II	1.11	
DBP307	De Beers Pool	e		c			19	15	80	4	IaAB	1.12	2.2
DBP308	De Beers Pool	h		c			44	0	0	44	IaA	0.22	
DBP315	De Beers Pool	h		c			110	50	45	60	IaAB	0.27	2.97
DBP316	De Beers Pool	p		c			188	39	21	148	IaAB	1.99	21.14
DBP318	De Beers Pool	p		c			214	36	17	177	IaAB	2.41	25.63
DBP320	De Beers Pool	p		c			15	11	74	4	IaAB	1.24	
DBP336	De Beers Pool	p		c			464	154	33	310	IaAB	4.71	64.8
DBP337	De Beers Pool	p		c			0	0		0	II		
DBP352	De Beers Pool	p		I/b			743	264	36	479	IaAB	0.7	186.18
DBP356	De Beers Pool	p		I/b			63	4	6	60	IaA		
DBP359	De Beers Pool	h		c			19	0	0	19	IaA	2.20	
DBP368	De Beers Pool	h		c			163	0	0	163	IaA	1.53	8.718
DBP369	De Beers Pool	p		c			32	24	76	8	IaAB		
DBP373	De Beers Pool	h		c			0	0		0	II	0.64	
DBP378	De Beers Pool	h		c			51	51	100	0	IaB	5.52	17.22
DBP409	De Beers Pool	h		c		-4.94	12	1	12	11	IaAB	0.78	
DBP423	De Beers Pool	h		c		-5.31	9	3		6	II	1.7	
DBP425	De Beers Pool	h		c		-4.46	499	58	12	441	IaAB	3.02	44.49
DBP432	De Beers Pool	h		c		-4.22	402	34	9	367	IaA	2.21	41.11
DBP452	De Beers Pool	h		c		-5.30	51	2	5	49	IaA	0.82	4.47
DBP468	De Beers Pool	e		c		-4.53	640	106	17	534	IaAB	17.57	63.74
DBP473	De Beers Pool	h		c		-5.48	12	12	100	0	IaB	0.39	
DBP497	De Beers Pool	h		c		-6.60	804	108	13	696	IaAB	0.56	78.86
DBP498	De Beers Pool	h		c			69	2	3	67	IaA		5.35
DBP499	De Beers Pool	h		c		-5.19	766	119	15	648	IaAB	0.63	67.94
DBP500	De Beers Pool	h		c		-5.18	17	0	0	17	IaA	0.24	1.08

Sample	location	paragenesis	shape	colour	deformation	$\delta^{13}C$	N (at. ppm)	N_B (at. ppm)	%IaB	N_A	Type	H area (cm^{-2})	P area (cm^{-2})
DBP509	De Beers Pool	h		c		-5.58	250	73	29	176	IaAB	2.17	49.31
DBP513	De Beers Pool	e		c		-3.06	14	13	94	1	IaB	1.32	
DBP538	De Beers Pool	e		c		-5.98	613	9	1	604	IaA	1.58	
DBP539	De Beers Pool	e		l/b		-5.33	764	406	53	358	IaAB	2.96	215.4
DBP543	De Beers Pool	e		c			445	9	2	436	IaA	3.8	9.04
DBP545	De Beers Pool	e		c		-5.22	901	104	12	796	IaAB	7.22	58.56
DBP547	De Beers Pool	e		c		-5.46	311	102	33	210	IaAB	2.44	80.26
G011	Ghana		o	c	n	-5.73	396	396	100	0	IaB	1.31	
G012	Ghana	p	o	c	n	-5.92	140	122	87	18	IaAB	26.39	59.49
G013	Ghana	p	m	c	n	-5.09	41	10	25	31	IaAB	0.5	1.63
G014	Ghana	p	o	c	n	-2.51	65	62	95	3	IaB	14.53	16.61
G015	Ghana	p	d	c	y	-4.47	137	32	23	105	IaAB	0.80	24.83
G016	Ghana	p	o	c	n	-2.27	169	60	35	110	IaAB	2.72	48.28
G019	Ghana	p	f/d	c	y	-3.94	70	38	54	33	IaAB	4.13	3.45
G020	Ghana	p	o	c	n	-4.15	212	27	13	184	IaAB	0.59	52.17
G021	Ghana	p	d	c	n	-5.63	18	18	100	0	IaB	2.25	
G022	Ghana	p	o	c	n	-3.46	56	15	27	40	IaAB	2.20	9.96
G023	Ghana	l	o	c	n	-4.47	55	14	25	41	IaAB	3.17	5.82
G025	Ghana	p	d	c	y	-4.65	1616	303	19	1313	IaAB		
G026	Ghana	p	o	c	n	-2.68	0	0		0	II	0.84	
G027	Ghana	p	o	c	n	-4.49	273	49	18	224	IaAB	2.2	39.2
G030	Ghana	h	f/o	c	n	-5.27	201	0	0	201	IaA	1.3	1.74
G031	Ghana	p	o	c	n	-5.28	5	0		5	II	0.24	
G032	Ghana	h	d	b	y	-4.32	48	19	40	29	IaAB	0.59	6.83
G033	Ghana	h	o	c	n	-3.53	215	95	44	120	IaAB	3.83	63.226
G034	Ghana	h	o	c	n	-3.47	94	27	29	66	IaAB	0.87	24.87
G035	Ghana	h	d	b	n	-5.45	260	251	97	9	IaB	10.6	
G036	Ghana	e	o	b	n	-3.85	205	47	23	158	IaAB	1.47	38.55
G037	Ghana	h	o	c	n	-3.93	239	19	8	220	IaA	1.37	35.93
G040	Ghana	h	d	t/g	y	-5.06	43	43	100	0	IaB	2.41	
G041	Ghana	l	o	c	n	-2.36	12	5	44	7	IaAB	1.39	
G042	Ghana	p	d	c	n	-4.29	504	504	100	0	IaB	27.94	9.66
G043	Ghana	p	d	c	n	-3.08	187	61	33	126	IaAB	0.25	39.19
G044	Ghana	p	m	c	n	-5.38	67	28	42	39	IaAB	0.31	12.17
G045	Ghana	p	d	c	n	-5.03	19	5	27	14	IaAB	0.34	1.37
G046	Ghana	p	o	c	n	-2.62	112	62	55	50	IaAB	3.68	35.19
G050	Ghana	l	m	b	n	-2.95	253	54	21	199	IaAB	0.70	10.78

Sample	location	paragenesis	shape	colour	deformation	$\delta^{13}C$	N (at. ppm)	N_B (at. ppm)	%IaB	N_A	Type	H area (cm^{-2})	P area (cm^{-2})
G051	Ghana	p	o	c	n	-5.28	944	268	28	677	IaAB	6.3	196.49
G103	Ghana	h	o	c	n	-2.31	106	66	62	40	IaAB	0.67	21.92
G104	Ghana	h	f/o	c	n	-3.56	697	353	51	344	IaAB		154.64
G105	Ghana	h	o	c	n	-4.24	0	0		0	II		
G106	Ghana	h	o	b	n	-3.89	33	23	68	11	IaAB	2.97	8.98
G108	Ghana	p	i/d	c	n	-4.45	141	113	81	27	IaAB	2.89	45.51
G109	Ghana	p	d	b	n	-2.52	255	75	29	181	IaAB	1.09	73.99
G110	Ghana	p	i/d	b	n	-4.15	83	0	0	83	IaA		28.51
G112	Ghana	h	o	c	n	-4.59	57	24	43	32	IaAB	2.23	3.81
G113	Ghana	l	d	c	y	-4.03	121	53	44	68	IaAB	0.80	18.79
G114	Ghana	p	o	c	n	-3.90	59	1	2	58	IaA	0.72	7.08
G116	Ghana	p	f/d	c	n	-4.95	79	30	38	49	IaAB	0.58	16.26
G117	Ghana	p	o	c	n	-3.62	58	16	27	43	IaAB	1.92	7.68
G118	Ghana	p	o/d	c	n	-6.02	85	0	0	85	IaA	2.81	21.45
G119	Ghana	p	o	c	n	-4.27	154	16	10	138	IaAB	2.64	52.65
G121	Ghana	p	d	c	n	-4.79	330	96	29	234	IaAB	0.90	63.54
G122	Ghana	p	f/d	c	n	-3.56	311	178	57	133	IaAB	0.95	92.83
G123	Ghana	p	d	c	n	-3.19	236	86	36	150	IaAB	1.0	39.47
G125	Ghana	p	o	c	n	-4.16	41	0	0	41	IaA	0.21	
G126	Ghana	h	m	c	n	-3.62	0	0		0	II		
G127	Ghana	p	i/d	b	n	-5.11	373	214	57	159	IaAB	1.42	94.24
G128	Ghana	p	o	c	n	-4.72	257	52	20	204	IaAB	0.79	50.67
G129	Ghana	p	o	c	n	-2.87	101	46	46	55	IaAB	1.29	12.09
G201	Ghana	l	d	b	n		30	13	43	17	IaAB	0.32	3.35
G202	Ghana	h	d	c	n		0	0		0	II		
G203	Ghana		d	c	y		145	71	49	73	IaAB	2.20	16.38
G204	Ghana	w	i/d	c	y		56	45	81	11	IaAB	6.60	20.76
G205	Ghana	p	i/d	c	n		189	77	41	112	IaAB		46.3
G206	Ghana	p	i/d	c	y		318	226	71	92	IaAB	0.96	139.31
G207	Ghana	p	o	c	n		0	0		0	II	0.34	
G208	Ghana	h	f/d	c	n		242	104	43	138	IaAB		87.64
G209	Ghana	h	o	c	n		35	10	30	24	IaAB	2.66	7.6
G301	Ghana	p	d	c	n		199	15	8	184	IaA	0.97	22.994
G302	Ghana	h	d	c	n		0	0		0	II	4.65	
G303	Ghana	deep-h	d	c	n		58	40	70	17	IaAB	1.66	5.536
G305	Ghana	h	o	c	n		0	0		0	II	6.94	
G306	Ghana	h	i/d	c	n		61	21	34	41	IaAB	2.20	

Sample	location	paragenesis	shape	colour	deformation	$\delta^{13}C$	N (at. ppm)	N_B (at. ppm)	%IaB	N_A	Type	H area (cm^{-2})	P area (cm^{-2})
G307	Ghana	h	d	c	n		393	101	26	292	IaAB		
G308	Ghana	p	o	c	n		315	294	93	21	IaB	5.18	169.85
R12001A	Renard	p				-1.19	338	127	37	211	IaAB	3.78	68.93
R12001B	Renard	p				-1.19	296	107	36	189	IaAB	4.51	57.06
R12003A	Renard					-3.95	14	0	0	14	IaA	0.53	1.68
R12003B	Renard					-3.95	21	4	18	18	IaAB	0.52	1.35
R12004A	Renard					-2.82	421	193	46	227	IaAB		
R12006aA	Renard					-3.09	183	35	19	148	IaAB		5.69
R12006aB	Renard					-3.09	154	7	5	147	IaA		5.85
R12011A	Renard					-3.01	863	486	56	377	IaAB	4.90	262.69
R12012A	Renard					-3.28	28	4	15	24	IaAB	2.98	1.45
R12012B	Renard					-3.28	26	1	4	25	IaA	2.48	2.05
R12013A	Renard	h				-3.38	297	215	72	83	IaAB	11.05	122.19
R12013B	Renard	h				-3.38	23	14	61	9	IaAB		
R12013C	Renard	h				-3.38	34	0	0	34	IaA	3.29	4.78
R12014A	Renard					-3.48	111	38	34	73	IaAB	0.66	21.14
R12014B	Renard					-3.48	55	11	20	44	IaAB		9.32
R12016aB	Renard	p				-4.7	111	56	50	56	IaAB	4.63	19.57
R12026A	Renard					-2.71	52	15	30	37	IaAB	2.60	
R12026B	Renard					-2.71	48	0	0	48	IaA	1.89	
R12027A	Renard					-2.86	14	7	52	7	IaAB	2.49	
R12027B	Renard					-2.86	4	0		4	II	1.00	
R12031A	Renard	p				-4.03	14	1	3	14	IaA	0.46	
R12031B	Renard	p				-4.03	37	23	61	14	IaAB		
R12036aA	Renard	p				-3.43	36	14	39	22	IaAB	1.33	2.75
R12036aB	Renard	p				-3.43	29	14	49	15	IaAB	0.60	4.5
R12036bA	Renard	p				-4.49	0	0		0	II	1.40	
R12036bB	Renard	p				-4.49	38	10	26	28	IaAB	3.36	
R12040A	Renard					-3.84	32	22	68	10	IaAB	0.97	4.74
R12040B	Renard					-3.84	22	0	0	22	IaA	2.42	6.02
R12041A	Renard	p				-3.5	29	0	0	29	IaA	1.40	
R12041B	Renard	p				-3.5	44	41	94	3	IaB	5.33	
R12042A	Renard					-3.64	162	41	25	122	IaAB	2.02	24.17
R12042B	Renard					-3.64	188	21	11	167	IaAB	1.63	14.79
R13520A	Renard	p				-4.35	39	15	39	24	IaAB	3.69	2.15
R13520B	Renard	p				-4.35	9	0		9	II	3.20	
R13521aA	Renard	p				-3.1	13	13	100	0	IaB	0.78	
R13521aB	Renard	p				-3.1	0	0		0	II	0.62	

Sample	location	paragenesis	shape	colour	deformation	$\delta^{13}C$	N (at. ppm)	N_B (at. ppm)	%IaB	N_A	Type	H area (cm^{-2})	P area (cm^{-2})
R13521bA	Renard	p				-4.08	1255	658	52	597	IaAB	37.18	
R13521bB	Renard	p				-4.08	1063	536	50	527	IaAB	41.49	
R13521cA	Renard	p				-3.08	72	42	59	30	IaAB	11.24	12.07
R13521cB	Renard	p				-3.08	32	21	67	10	IaAB	6.96	7.72
R13523A	Renard	h				-3.65	49	12	25	37	IaAB	2.28	8.31
R13523B	Renard	h				-3.65	57	17	31	40	IaAB		6.5
R13524A	Renard					-3.39	0	0		0	II	2.58	
R13524B	Renard					-3.39	0	0		0	II	1.0	
R13527A	Renard					-3.46	0	0		0	II		
R13527B	Renard					-3.46	0	0		0	II	0.69	
R13528aA	Renard					-3.89	94	42	45	52	IaAB	16.9	22.31
R13528aB	Renard					-3.89	119	46	38	74	IaAB	23.16	20.49
R13528bA	Renard					-3.38	0	0		0	II		
R13528bB	Renard					-3.38	0	0		0	II		
R13530aA	Renard	p				-3.06	65	18	28	47	IaAB	4.23	11.07
R13530aB	Renard	p				-3.06	70	25	36	45	IaAB	2.2	7.25
R13530bA	Renard	p				-3.53	5	0		5	II	1.02	1.76
R13530bB	Renard	p				-3.53	46	16	35	30	IaAB	4.11	
R13530cA	Renard	p				-3.89	9	0		9	II		
R13530cB	Renard	p				-3.89	22	2	8	20	IaA	0.63	
R13531aA	Renard	p				-5.41	604	187	31	416	IaAB	1.34	97.25
R13531aB	Renard	p				-5.41	1108	463	42	645	IaAB	1.3	199.4
R13531bA	Renard	p				-4.38	49	9	18	40	IaAB	1.74	2.42
R13531bB	Renard	p				-4.38	45	11	25	34	IaAB	2.82	0.763
R13532aA	Renard	l				-3.71	40	8	20	32	IaAB	0.15	5.1
R13532aB	Renard	l				-3.71	42	21	51	20	IaAB	0.59	3.08
R13532bA	Renard	l				-3.37	78	28	36	51	IaAB	2.10	12.51
R13532bB	Renard	l				-3.37	76	28	37	48	IaAB	4.61	5.443
R13533A	Renard	p				-4.47	70	25	36	45	IaAB	0.34	11.21
R13533B	Renard	p				-4.47	41	18	43	23	IaAB		8.34
R13536A	Renard	p				-2.09	1	0		1	II	0.67	
R13536B	Renard	p				-2.09	3	0		3	II	0.99	
R13537A	Renard	p				-3.51	12	4	35	8	IaAB		
R13537B	Renard	p				-3.51	0	0		0	II	0.50	
R13538A	Renard	p				-3.53	15	7	45	8	IaAB	2.09	
R13538B	Renard	p				-3.53	47	24	52	22	IaAB	1.78	1.61
R13539aA	Renard	p				-3.66	20	9	46	11	IaAB	1.58	
R13539aB	Renard	p				-3.66	7	0		7	II	1.89	

Sample	location	paragenesis	shape	colour	deformation	$\delta^{13}C$	N (at. ppm)	N_B (at. ppm)	%IaB	N_A	Type	H area (cm^{-2})	P area (cm^{-2})
R13540A	Renard					-3.49	377	94	25	283	IaAB	0.40	70.74
R13540B	Renard					-3.49	405	97	24	309	IaAB	0.90	79.26
R13544A	Renard	I				-5.35	62	14	23	48	IaAB	6.38	18.77
R13544B	Renard	I				-5.35	82	29	35	53	IaAB	4.45	28.43
R13545A	Renard					-3.16	66	23	34	44	IaAB	1.65	15.62
R13545B	Renard					-3.16	66	25	37	42	IaAB	1.45	23.28
R13547aA	Renard	p				-4.08	0	0		0	II	0.94	
R13547aB	Renard	p				-4.08	0	0		0	II	0.86	
R13547bA	Renard	p				-3.94	350	233	67	117	IaAB	2.94	150.41
R13547bB	Renard	p				-3.94	332	221	67	111	IaAB	2.86	140.03
R13548A	Renard					-3.28	786	308	39	478	IaAB	2.34	186.91
R13548B	Renard					-3.28	348	252	72	96	IaAB	2.03	155.68
R13803aA	Renard	p				-4.35	63	26	42	37	IaAB	0.78	15.45
R13803aB	Renard	p				-4.35	109	36	33	74	IaAB	1.90	28.312
R13803bA	Renard	p				-4.01	39	19	50	19	IaAB	1.34	2.02
R13803bB	Renard	p				-4.01	47	22	46	26	IaAB	5.92	11.28
R13803cA	Renard	p				-3.34	22	0	0	22	IaA	2.41	
R13803cB	Renard	p				-3.34	11	0	0	11	IaA	1.43	
R13804aA	Renard	p				-3.31	0	0		0	II		
R13804aB	Renard	p				-3.31	19	2	10	17	IaA	1.03	1.962
R13804bA	Renard	p				-3.74	195	119	61	77	IaAB	6.09	64.27
R13804bB	Renard	p				-3.74	0	0		0	II		
R13805aA	Renard	p				-3.37	142	53	37	89	IaAB	2.36	29.65
R13805aB	Renard	p				-3.37	163	51	31	112	IaAB	0.92	35.54
R13805bA	Renard	p				-3.85	447	109	24	339	IaAB	3.40	63.51
R13805bB	Renard	p				-3.85	369	100	27	269	IaAB	0.71	59.33